Nuclear dipole interactions in solid Xe-129 measured with NMR

Dissertation

Presented in Partial Fulfillment
of the Requirements for the Degree of

Doctor of Natural Sciences
(Dr. rer. nat.)

Submitted to the Faculty of Physics
Philipps-University Marburg

by

Alexander Potzuweit

Marburg/Lahn 2015

"There's something that doesn't make sense. Let's go and poke it with a stick."

– Doctor Who –

Vom Fachbereich Physik der Philipps-Universität als Dissertation
am 01.04.2015 angenommen.

Erstgutachter:	Prof. Dr. Heinz J. Jänsch
Zweitgutachter:	Prof. Dr. Werner Heil
Tag der mündlichen Prüfung:	08.05.2015
Hochschulkennziffer	1180

Abstract

This thesis describes nuclear magnetic resonance experiments on hyperpolarized ^{129}Xe. With spin exchange optical pumping on rubidium it is possible to enhance the ^{129}Xe spin polarization to five orders of magnitude above its thermal equilibrium. This allows for experiments on small samples, like films on metal substrates.
During this graduation the installation of a new polarization apparatus was completed. With it, it is possible to create mixtures of ^{129}Xe with other gases. Mixtures with spin-less ^{132}Xe are of particular interest, because they allow the manipulation of nuclear dipole-dipole interactions through a variation of the distance.

The line shape of solid ^{129}Xe nuclear magnetic resonances is dominated by dipolar effects. Since an analytical calculation of the resonance shape is impossible, the moments may be used instead. The parameter dependencies of the first three moments on the polarization and the mixing ratio are quantum mechanically calculated and then verified in experiments. To extract the moments from experimental data a product fit function is introduced, and a determination of the polarization from the skewness of the resonance line is discussed.

The dipole-dipole interaction is also responsible for spin diffusion, which plays an important role in the relaxation. A thin xenon film on a copper substrate may be used as a model system to investigate spin diffusion in a quasi-1d system.

If the dipole-dipole interaction is entirely suppressed by dilution, it is possible to observe annealing effects in the frozen xenon mixture.

Zusammenfassung

Diese Arbeit beschäftigt sich mit Kernspinmessungen an hyperpolarisiertem ^{129}Xe. Mit Hilfe des optischen Pumpens von Rubidium und Spintransfer kann die Kernpolarisation des Xenon um fünf Größenordnungen über das thermische Gleichgewichtsniveau angehoben werden. Dies erlaubt es, auch sehr kleine Proben spektroskopisch zu untersuchen, z.B. dünne Filme auf Metallsubstraten.
Im Rahmen dieser Promotion wurde die Umstellung auf eine neue Polarisationsapparatur abgeschlossen, mit der es möglich ist, das spektroskopisch aktive ^{129}Xe mit anderen Gasen zu mischen. Insbesondere Mischungen mit spektroskopisch inaktivem ^{132}Xe sind interessant, weil sich hierdurch die Dipol-Dipol-Wechselwirkung der Kernspins über den Abstand der Kerne variieren lässt.

Die Linienform der Kernspinresonanz von ^{129}Xe Festkörpern wird von dipolaren Effekten dominiert. Da es nicht möglich ist, diese Linienform analytisch zu berechnen, wird in dieser Arbeit auf die Momente der Resonanzlinie zurückgegriffen. Die Parameterabhängigkeiten der ersten drei Momente von der Polarisation und dem Mischungsverhältnis werden quantenmechanisch hergeleitet und in der Folge mit experimentellen Kernspinmessungen verglichen. Um die Momente aus den experimentellen Daten zu extrahieren, wird hierzu eine Produkt-Fit-Funktion vorgeschlagen. Eine Polarisationsbestimmung anhand der Schiefe der Resonanzlinie wird diskutiert.

Ein weiterer Effekt der Dipol-Dipol-Wechselwirkung ist die Spindiffusion, die eine wesentliche Rolle bei der Polarisationsrelaxation spielt. Es wird gezeigt, dass ein dünner ^{129}Xe Film auf einem Kupfersubstrat ein geeignetes Modell ist, um Spindiffusion experimentell in einem Quasi-1D System zu untersuchen.

Wird die Dipol-Dipol-Wechselwirkung durch Verdünnung fast vollständig unterdrückt, so erhält man Resonanzen, die schmal genug sind, um Annealing-Effekte im gefrorenen Xenon-Gemisch zu untersuchen.

Contents

List of Figures

List of Tables

1. Introduction

Bloch, Hansen, and Packard [Blo46] and Purcell, Torrey, and Pound [Pur46] discovered NMR independently in 1946, and both Bloch and Purcell were awarded the Nobel Prize for it in 1952. Since then the NMR technique has come a long way, and today it is used in a wide variety of fields. In chemistry it is one of the key analysis tools for molecular structure. In physics the applications range from diffusion measurements to quantum computing. With the advent of modern computing, NMR technique has taken a leap forward to magnetic resonance imaging (MRI), allowing us to look inside the human body in a non-destructive and non-invasive way.

Ever since then, the low sensitivity of NMR has been an incentive to develop stronger magnets and more elaborate pulse sequences, which require smaller samples or less measuring time.
With Kastler's discovery of optical pumping [Kas50], for which he was awarded with the Nobel prize in 1966, it became possible to create hyperpolarized spin ensembles, thus increasing the NMR signal by up to five orders of magnitude. Today, spin exchange optical pumping (SEOP) is frequently used to hyperpolarize alkali metals and transfer the polarization to rare gas nuclei [Hap72, Wal97], most notably ^{129}Xe.
Rare gas solids are bound by Van der Waals forces, so they form closed packed lattices, which are important model systems, because of their simplicity [Kle76]. The objective of this thesis is to widen our understanding of solidified hyperpolarized ^{129}Xe.

The distinctive feature of our experimental setup is the ability to create any mixture of ^{129}Xe and ^{132}Xe isotopes on which to perform NMR spectroscopy. While ^{129}Xe is a spin $I = 1/2$ nucleus, ^{132}Xe is a $I = 0$ nucleus and thus invisible to the NMR. By mixing them, it is thus possible to separate the nuclear spins from each other and alter the strength of their interaction. In addition, our experiments include the experimental effort of a second field, namely the surface science. We conduct our experiments in an ultra high vacuum on a clean single crystal surface and are able to investigate single xenon layers on metal substrates [Jän04, Koc06b]. The single crystal used for this dissertation is copper in the (100) orientation.

In order to better understand the nuclear (dipole) interactions, a large part of this dissertation deals with the theoretical background of resonance line shapes of xenon mixtures. Several experiments were conducted to validate the previous theoretical work. This part – while interesting in itself – also offers new ways of polarization measurements [Tsy12]. With this background set, it is possible to conduct various mixing experiments. For instance, a mixture of ^{129}Xe with high ^{132}Xe content has a strongly reduced dipolar line

width, even to the point where structural defects become dominant. In this regime we can perform annealing experiments.
An other example is the combination with surface science techniques, where two separate phases of each isotope can be employed to measure the spin diffusion inside the ^{129}Xe bulk. This is important on a fundamental level, since most hyperpolarization experiments have to store the hyperpolarized xenon in the frozen form, and the spin diffusion is a key component of the depolarization [Sam05, Mor07, Gat93, Fit99].

This thesis has the following structure. Chapter 2 describes the theoretical part, which is followed by the experimental setup in chapter 3, and the experiments themselves are described in chapter 4. The thesis closes with a summary and an outlook of future experiments to come, in chapter 5 and 6 respectively.

2. Theory

2.1. The NMR experiment

In this section I will describe the basic nuclear magnetic resonance (NMR) principles. A more detailed account may be found in any NMR textbook, such as "Principles of Nuclear Magnetism" by Abragam [Abr61] or "Experimental Pulse NMR: A Nuts and Bolts Approach" by Fukushima and Roeder [Fuk81].

The basic idea behind NMR is to use the atomic nuclei or, more precisely, to use the magnetic moment of the nuclei as probes of their surrounding.
Every atomic nucleus with a non-vanishing spin I also possesses a magnetic moment μ. Both are related via the gyromagnetic ratio γ.

$$\vec{\mu} = \gamma \vec{I} \tag{2.1}$$

One might choose a different proportionality constant: the g-factor g, which is the dimensionless analogon of the gyromagnetic ratio. For convenience the nuclear magnetic moment is here normalized with the nuclear magneton μ_N.

$$\frac{\vec{\mu}}{\mu_N} = g \frac{\vec{I}}{\hbar} \tag{2.2}$$

Unfortunately, there are important elements in which the dominant isotope has no magnetic moment. Notable examples of $I = 0$ nuclei are ^{4}He, ^{12}C, ^{16}O and ^{40}Ar.

An $I \neq 0$ nucleus in a static magnetic field B_0 will exhibit the nuclear Zeeman effect which means the m_F degeneracy is lifted. One can then stimulate transitions between the Zeeman levels by applying radio frequency to the sample. The resonance frequency is the Larmor frequency ν_L which is a function of magnetic field and gyromagnetic ratio.

$$\nu_L = \frac{\Delta E}{h} = \frac{\gamma B_0}{2\pi} \qquad \text{and} \qquad \omega_L = \frac{\Delta E}{\hbar} = \gamma B_0 \tag{2.3}$$

The individual magnetic moments of the sample are an ensemble and couple to form the magnetization $\vec{M} = \sum \vec{\mu}_i / V$ that is the density of the magnetic moments in the volume V. In many respects we can apply the same rules to the magnetization as to a single

spin. The time evolution of the magnetization in a magnetic field B_0, which is oriented along the z-axis follows the Bloch equations, eq. 2.4.

$$\begin{aligned} \frac{dM_x}{dt} &= \gamma(\vec{M} \times \vec{B}_0)_x - \frac{M_x}{T_2} \\ \frac{dM_y}{dt} &= \gamma(\vec{M} \times \vec{B}_0)_y - \frac{M_y}{T_2} \\ \frac{dM_z}{dt} &= \gamma(\vec{M} \times \vec{B}_0)_z - \frac{M_z - M_0}{T_1} \end{aligned} \tag{2.4}$$

The Bloch equations contain two decay times: T_1 and T_2. The latter is the transverse or spin–spin relaxation time. On this timescale the spins performing a precession around the z-direction get out of phase. In contrast, T_1 is the longitudinal or spin–lattice relaxation time. If the magnetization is out of equilibrium, because it was depleted or artificially increased, the magnetization will return to its equilibrium value M_0 on the T_1 timescale.
If, for instance, we choose the initial conditions $M_x = M_y = 0$, $M_z(t{=}0) = M$, for the Bloch equations (eq. 2.4), we get the solution $M_z(t) = M_0 + (M - M_0) \cdot \exp(-t/T_1)$, an exponential approach of the initial magnetization to its equilibrium value. In the same manner, a deflection from the z-axis into the x-y plane yields an oscillatory and exponentially damped result (see also fig. 2.1).

On a fundamental level there are two different NMR methods: continuous wave (cw) and pulse NMR. In a cw experiment the radio frequency is continuously applied to the sample and either its frequency or the 'static' magnetic field is swept through the resonance condition. This stands in contrast to a pulse NMR experiment where a short burst of radio frequency is applied to the sample while the static field is kept constant. This pulse moves the magnetization away from its equilibrium orientation along the z-axis. The resulting angle between z-axis and magnetization is called the pulse angle. A pulse can be characterized by four properties: pulse amplitude, frequency, length and shape. Unless otherwise noted, all experiments I describe in this work use rectangular shaped pulses. The pulse length is then adjusted to the desired pulse angle. In cases where a pulse is designed to be frequency selective – to excite only the parts of the sample that are close to the pulse frequency – a Gaussian shaped pulse with a much lower amplitude and therefore a longer duration is used. From basic Fourier theory it is evident that the longer a pulse is in the time domain the narrower it is in the frequency domain.
After the pulse, the magnetization starts a free precession motion around the z-axis, called the free induction decay (FID) – see also the Bloch equations (eq. 2.4). A coil surrounding the sample will pick up the precession as an alternating induced voltage. This signal is amplified and then digitized in the NMR spectrometer. Afterwards, it is multiplied with a reference frequency and the same frequency shifted by a 90 ° phase (quadrature detection). Together both signals may be interpreted as one signal with a real and an imaginary part. This allows the application of the complex fast Fourier

transform (FFT) for transforming the time series into the frequency domain.
Figure 2.1 shows a spectrum of an experiment with a small pulse angle with the corresponding FID shown in the inset. The line shape loosely resembles a Lorentzian, see section 2.5 for a detailed discussion. The phase was manually adjusted to yield an absorption line.

One of the main problems of any NMR experiment is the lack of sensitivity and its constant struggle with noise. Apart from improving the hardware and the experimental setup there are at least two basic ways for improving the signal to noise ratio. One is repetitively measuring the same effect and summing up. In this case the signal will increase linearly with the number of repetitions n since it is phase locked. The noise, on the other hand, will only increase with the square-root of repetitions $\sqrt{n}$. This approach is often limited by the T_1 time (preventing an arbitrarily fast repetition) and thus by the time one is willing to spend on the experiment.
An other way to improve the signal to noise ratio is to increase the magnetization beyond its thermal equilibrium. This can be achieved with a spin polarization transfer [Har62] or a previous hyperpolarization of the sample. In this context it is easier to speak of the polarization (which is proportional to the magnetization) than the magnetization itself. In calculating the magnetization the sum over all magnetic moments will essentially sum up the same magnetic moment multiple times with a different sign (+/− or spin up/spin down in a spin 1/2 system). If we strip away all material specifics, the key feature is the difference between those nuclei with spin up and those with spin down. We thus define the polarization as this difference normalized by the total number of spins $N = N_\uparrow + N_\downarrow$.

$$P = \frac{N_\uparrow - N_\downarrow}{N} = 2\frac{N_\uparrow}{N} - 1 \tag{2.5}$$

In thermal equilibrium the polarization is derived from the Boltzmann factor

$$\frac{N_\downarrow}{N_\uparrow} = e^{-\frac{\Delta E}{kT}} \quad . \tag{2.6}$$

For ^{129}Xe in a 2 T magnetic field at 30 K this yields $\frac{N_\downarrow}{N_\uparrow} \approx 1 - 4 \times 10^{-5}$ and a polarization of 1.9×10^{-5}. Using hyperpolarization techniques, the polarization can be increased to 0.5 and above. These five orders of magnitude are, incidentally, the signal gain needed to measure the xenon surface that has 10^{14} nuclei compared to 10^{19} nuclei in a bulk sample [Ger03, Koc06a]. Furthermore, it should be noted that at 30 K it can take hours to reach thermal equilibrium, see chapter 4.10.

2.2. Spin-exchange optical pumping

Spin-exchange optical pumping (SEOP) is a procedure that can increase the nuclear spin polarization far beyond the thermal equilibrium. For a review on the subject by

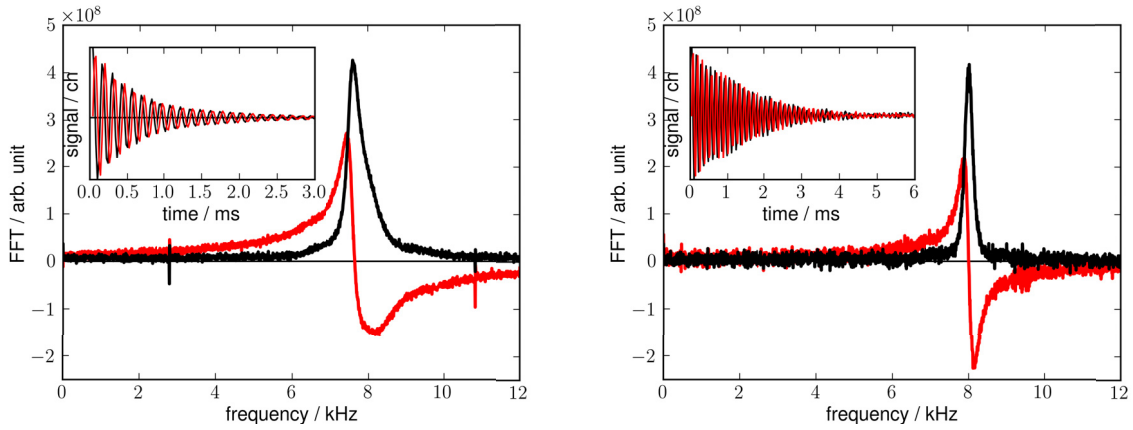

Figure 2.1.: Spectrum of a ^{129}Xe NMR experiment with a single small angle pulse (*black:* real part and *red:* imaginary part). Left diagram: pure ^{129}Xe. Right diagram: $\approx 5\,\%$ ^{129}Xe. No windowing was applied. The inset shows the FID.

Walker and Happer see [Wal97].
SEOP uses alkali vapor to transfer laser circular polarization to noble gas nuclei. In our setup (see chapter 3) we use rubidium that is contained in a cylindrical glass cell for that purpose. The cell is heated to produce rubidium vapor. Circularly polarized laser light is used to excite the D_1 transition from the $^2S_{1/2}$ ground state to the first excited state $^2P_{1/2}$. A (collinear) magnetic field ensures that the m_F degeneracy is lifted and a population difference of the m_F states is reached far beyond the thermal equilibrium. The result is a net electronic spin polarization of the rubidium vapor.
We then add ^{129}Xe and nitrogen gas. Upon a binary collision of a xenon and a rubidium atom or the formation of a Van der Waals molecule the rubidium electron spin polarization is transferred to the xenon nuclei. Depending on the pressure regime one of the processes is dominant – in our case (at roughly 100 mbar) it is the formation and break up of Van der Waals molecules [Wal97].
The nitrogen gas serves two purposes. First, it acts as a quench gas, preventing the rubidium atoms to emit unpolarized light upon deexcitation that would reduce the population difference. Second, it causes pressure broadening, thus extending the laser absorption range [Rot97, Pit14].

2.3. Korringa Relaxation and Knight Shift

The Korringa relaxation is a mechanism that causes spin polarized nuclei to lose their polarization when in contact with a metal. The conduction band electrons of the metal are scattered at the nuclei and cause nuclear spin-flips there. This effect has to be considered in ^{129}Xe NMR experiments on metal surfaces [Sta02, Koc06a, Sch15]. In this thesis the Korringa relaxation is used as a well defined polarization drain to measure the

spin diffusion, see section 2.8.

The observed relaxation rate is proportional to the thermal energy kT and the local density of states LDOS at the Fermi energy [Sta02, Abr61].

$$\frac{1}{T_1} = \frac{4\pi}{9}\mu_0^2\gamma_e^2\gamma_I^2\hbar^3 \left(\mathrm{LDOS}(E_f)\right)^2 kT \tag{2.7}$$

The evaluation of the right hand side is difficult, but a shortcut exists. The contact with the metal substrate not only causes a faster relaxation, but also an NMR frequency shift: the so called Knight shift $K = \Delta\omega/\omega$. The Knight shift is directly related to the Korringa relaxation through the Korringa relation [Sta02, Koc06a, Abr61]:

$$\frac{1}{T_1} = K^2 \frac{4\pi kT}{\hbar} \left(\frac{\gamma_I}{\gamma_e}\right)^2 b \tag{2.8}$$

$\gamma_{e/I}$ are the gyromagnetic ratios of the electron and the nucleus, and b is a correction factor to account for effects that influence the Knight shift and the Korringa relaxation differently. For free electrons this factor equals 1.
In his dissertation, Matthias Koch reported that the ^{129}Xe Knight Shift on the Cu(111) surface at a temperature of 90 K is 1297 ppm, from which he calculated a relaxation time of $T_1 \approx 12$ ms [Koc06a]. Anuschka Schaffner investigated the Knight shift on the Cu(100) surface for her thesis and found a shift of approximately 600 ppm, also at 90 K [Sch15]. The factor of two between the Cu(100) and the Cu(111) surface cause the relaxation time to be four times longer on the Cu(100) surface, which yields 50 ms.
The temperature dependency of the Knight shift and thus the relaxation time at 30 K remains unclear. Using eq. 2.7 nonetheless, we can estimate $T_1 \approx 150$ ms.

2.4. Dipole interactions

A major part of this thesis concerns the resonance line shape and spin diffusion, which are both results of dipolar interactions. Therefore, the next sections describe these effects.
The homonuclear dipolar Hamiltonian can be written as the sum of six contributions (eq. 2.9 and 2.10). They are sorted by the amount by which they change the relation (polarization) between spin up and spin down states [Abr61].

$$H_{DD} = \sum_{j<k} \frac{\gamma^2}{r_{jk}^3}\left(\vec{I}_j \cdot \vec{I}_k - 3\frac{(\vec{I}_j \cdot \vec{r}_{jk})(\vec{I}_k \cdot \vec{r}_{jk})}{r_{jk}^2}\right) = \sum_{j<k} \frac{\gamma^2}{r_{jk}^3}(A + B + C + D + E + F) \tag{2.9}$$

$$
\begin{aligned}
A &= (1 - 3\cos^2(\theta))I_j^z I_k^z \\
B &= -\frac{1}{4}(1 - 3\cos^2(\theta))(I_j^+ I_k^- + I_j^- I_k^+) \\
C &= -\frac{3}{2}\sin(\theta)\cos(\theta)e^{-i\phi}(I_j^z I_k^+ + I_j^+ I_k^z) \\
D &= -\frac{3}{2}\sin(\theta)\cos(\theta)e^{i\phi}(I_j^z I_k^- + I_j^- I_k^z) \\
E &= -\frac{3}{4}\sin^2(\theta)e^{-2i\phi}I_j^+ I_k^+ \\
F &= -\frac{3}{4}\sin^2(\theta)e^{2i\phi}I_j^- I_k^-
\end{aligned} \tag{2.10}
$$

$I_j^{+/-}$ are the raising/lowering operators acting on spin j, and I_j^z is the z-component spin operator. The r, θ and ϕ coordinates are the distance and angles in the spherical coordinate system.
These six contributions named $A - F$ are also called the dipolar alphabet. In the homonuclear case the A and B terms commute with the Zeeman Hamiltonian, therefore they are also called the secular part. While these two terms conserve the polarization $[\Delta(m_j + m_k) = 0]$, the terms C–F contain (unpaired) ladder operators and thus change the polarization and the energy state $[\Delta(m_j + m_k) = \pm 1, \pm 2]$.

In the following section I will review the implications of the dipole-dipole interaction on the NMR resonance line.

2.5. Resonance line shape

The line shape of an NMR absorption line is often rather complicated and unfortunately, there is no analytical solution to this line shape problem [Abr73]. In this section I will summarize the influence of polarization and concentration on the line shape through dipolar interactions.
As early as 1948, van Vleck described a method to derive analytical expressions for the moments of an absorption line [VV48]. Other authors found relations between the moments and the polarization [Abr73, Tsy12]. The $n-$th moment of a resonance line is defined by

$$
\langle m^n \rangle = \int_{-\infty}^{\infty} \nu^n f(\nu) d\nu \Big/ \int_{-\infty}^{\infty} f(\nu) d\nu \quad . \tag{2.11}
$$

$f(\nu)$ is the real part in fig. 2.1. The (central) moments $\langle \nu^n \rangle := \langle (m - \langle m \rangle)^n \rangle$ about the first moment are often more informative.

$$\begin{aligned}\langle\nu\rangle - \mu B &\propto P \\ \langle\nu^2\rangle &\propto 1 - P^2 \\ \langle\nu^3\rangle &\propto P(1 - P^2) \\ \langle\nu^4\rangle &\propto (1 - P^2)(1 - \alpha P^2)\end{aligned} \tag{2.12}$$

Equations 2.12 show the results from [Abr73, Tsy12]. In both publications $\hbar$ is set to unity and it is assumed that the spin carrying nuclei are the sole component.
The first central moment is easily understandable. The center of the resonance line is at a frequency μB given by the static magnetic field and the chemical shift. In addition it gets shifted by its own magnetization that is proportional to the polarization: The nuclear spins generate a magnetic field which shifts the resonance frequency of the same nuclei.
We can interpret the second moment as the line width. With a polarization close to 100 % almost all spins point in one direction, the few pointing in the opposite direction are thinly distributed 'impurities'. In this case one expects a narrow line since all nuclear spins are in similar surroundings. The broadest line width is found for small polarizations, when statistically the variance of surroundings is highest, see appendix B.4.
For the higher moments a physical interpretation is not so readily found.

With our new polarization apparatus it is possible to dilute spin carrying ^{129}Xe in spinless ^{132}Xe, adding a parameter that is not considered in the literature. Therefore, I extended the calculations of the moments by a concentration parameter c, which is the probability for a randomly chosen nucleus to carry spin. The calculations are fairly long and can be found in appendix B. The results of the calculations are shown in eq. 2.13.

$$\begin{aligned}\langle\nu\rangle &= \mu B - \lambda_1 c P \\ \langle\nu^2\rangle &= \lambda_2\Big(c - c^2 P^2\Big) \\ \langle\nu^3\rangle &= cP\Big[\lambda_3\Big(c - 1\Big) + \lambda_4\Big(c - c^2 P^2\Big)\Big]\end{aligned} \tag{2.13}$$

Here the λ parameters contain the geometrical information of the crystal structure and the direction of the magnetic field.
With the exception of very low concentrations of ^{129}Xe the third central moment is unequal zero and the resonance line is thus asymmetric. The physical origin of this effect is not entirely clear. The quantum mechanical calculations only use the A and B terms from the Hamiltonian, eq. 2.9 and 2.10. When Matthias Buschmann did Monte Carlo simulations of the line width (see section 2.7), he did not encounter asymmetric lines [Bus11]. Because these were classical simulations he only used the A term from the Hamiltonian. So most likely the asymmetry is a result of the incorporation of the spin-flip term B.

One might wonder if it is possible to reverse this process that is to derive a function from the moments that approximates the resonance line. This is called the *moment problem*, and the algorithm can be found in appendix B.5. Because the result is a sum over two δ-functions this cannot be used to approximate a spectrum.

Furthermore, the line shape is influenced by the pulse angle, a topic that is not covered in this thesis. In the case of highly polarized samples the high temperature approximation is no longer valid, and higher order terms have to be included. As a result the amplitude of the FID is no longer proportional to the sine of the pulse angle [Wal04].

2.6. Polarization induced line shift

As shown in the last section, the first moment of the resonance line depends not only on the static magnetic field, but also on the concentration of ^{129}Xe nuclei times the polarization. Thus it is possible to determine the polarization from the amount the resonance line is shifted from its position at zero polarization. We employ this regularly to determine the polarization. The advantage of this method compared to polarization estimations based on the amplitude is its robustness against experimental faults.
For a quantitative determination of the polarization one needs the proportionality constant λ_1 in eq. 2.13, which equals the frequency shift $\Delta\nu$ at 100 % polarization. This is far from trivial, as it depends on the sample geometry in relation to the magnetic field. For a thin film one finds [Tas87, Can94, Ger03]:

$$\begin{aligned} \Delta\nu &= \frac{\gamma}{2\pi}\mu_0\,\mu\,n\,\frac{1-3\cos^2(\theta)}{2}\,cP = cP\cdot 470\,\mathrm{Hz} \\ P &= \frac{\Delta\nu}{c\cdot 470\,\mathrm{Hz}} \end{aligned} \tag{2.14}$$

θ is the angle between the surface normal of the thin film and the static magnetic field. n is the (number) density of nuclei and μ their magnetic moment.
To calculate the relation in eq. 2.14 the authors use classical electromagnetic arguments. It is therefore not inherently clear if these equations hold for the frequency of the maximum of the resonance line, or for the first moment, which may be unequal in the case of asymmetric resonance lines.

2.7. Resonance width and asymmetry

In the high polarization regime the line width and its shape become functions of the concentration (the ^{129}Xe/^{132}Xe mixing ratio). In this section I will examine this dependency more closely.

In his diploma thesis Matthias Buschmann reports Monte Carlo simulations he conducted to investigate the NMR line width of a ^{129}Xe/^{132}Xe mixture [Bus11]. His simulation algorithm created a fcc crystal of about 530 atoms with spherical shape (radius = 3 × lattice constant). In consecutive runs the spin orientations were randomly distributed and the dipolar influence on every lattice site calculated. The basic model of the dipolar interaction he used is a classical one restricted to interactions of two spins, neglecting quantum mechanical effects. It thus equals the A term in the dipole Hamiltonian.

After calculating the dipolar field at each lattice site Matthias Buschmann assembled a histogram of the resulting line shifts. With 10^5 runs the histogram was smooth enough to extract the line width with a Gaussian fit. Figure 2.2 shows his results together with the second moment I calculated in section 2.5. I applied a single scaling factor to the second moment to account for the geometrical parameters. It is possible to deduce this factor from the line shift, as Matthias Buschmann did. In this case one has to multiply the result with 3/2, a quantum mechanical correction [VV48]. The quantum mechanical calculations, see appendix B, naturally include this factor.
The similarity between the numerical and analytical results are striking. The deviations have their origin in the discrete and finite size of the simulation. This is most prominent in the case of very low concentrations or high concentrations combined with high polarizations. In both circumstances the ^{129}Xe spins (or one orientation thereof) are so few that singular spins affect the result of the Monte Carlo simulation, see chapter 3.5 in Matthias Buschmann's diploma thesis [Bus11].

The polarization/concentration not only influences the resonance width, but also the third central moment, see eq. 2.13. Peter Gerhard and Matthias Buschmann already described in their respective doctoral or diploma theses the experimental resonance line to be asymmetric [Ger03, Bus11]. Both tried to fit the resonance line with either two Lorentzians or with a Gaussian and a Lorentzian. This reduced the deviation of fit and data, but ultimately lacked a physical justification. Worse, such a fit is not very stable numerically and so the fit parameters show a wide spread. In the appendix A a different approach to this fitting problem is described.

A better way to quantify the asymmetry is the skewness. It is defined as the third central moment divided by the third power of the standard deviation. From eq. 2.13 follows:

$$Skew = \frac{\langle \nu^3 \rangle}{\langle \nu^2 \rangle^{3/2}} = cP \frac{\lambda_3(c-1) + \lambda_4(c - c^2P^2)}{\lambda_2^{3/2}(c - c^2P^2)^{3/2}} \overset{c=1}{\propto} \frac{P}{\sqrt{1-P^2}} \tag{2.15}$$

Figure 2.3 shows the RHS for $c=1$ and the corresponding central moment. The skewness is a strictly increasing function and thus it is invertible. One can therefore deduce the polarization by measuring the skewness, something which is not possible with the third moment.

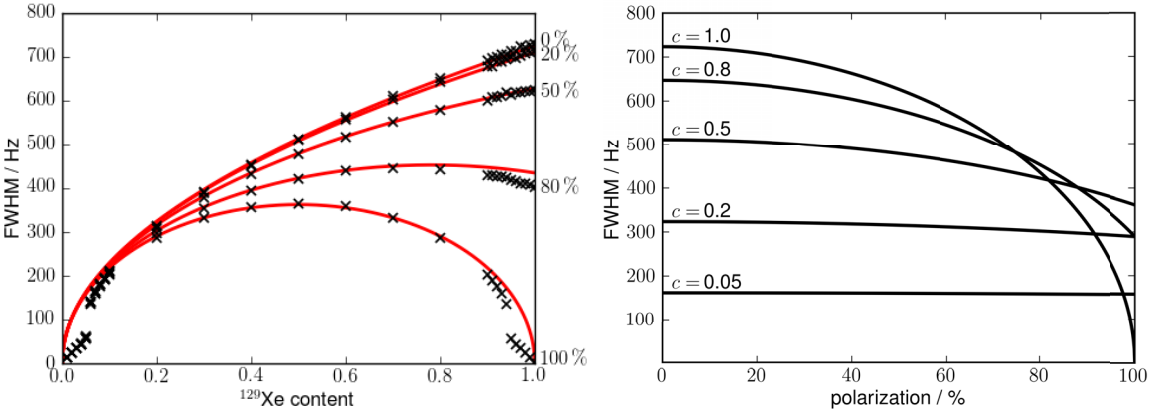

Figure 2.2.: Line width dependence on ^{129}Xe content and polarization. *Left diagram:* Line width as a function of ^{129}Xe content in the mixture for various polarizations (right axis). Symbols refer to the Monte Carlo simulations of Matthias Buschmann [Bus11]. Lines show the analytical result $\sqrt{\langle \nu^2 \rangle}$ from eq. 2.13, scaled with a single factor. With increasing polarization the neighborhood of a spin will become more homogenous. This effect is more prominent in pure ^{129}Xe. *Right diagram:* Line width as a function of polarization for various concentrations, analytical result. The higher the ^{132}Xe content of the mixture, the lower is the influence of the polarization on the line width.

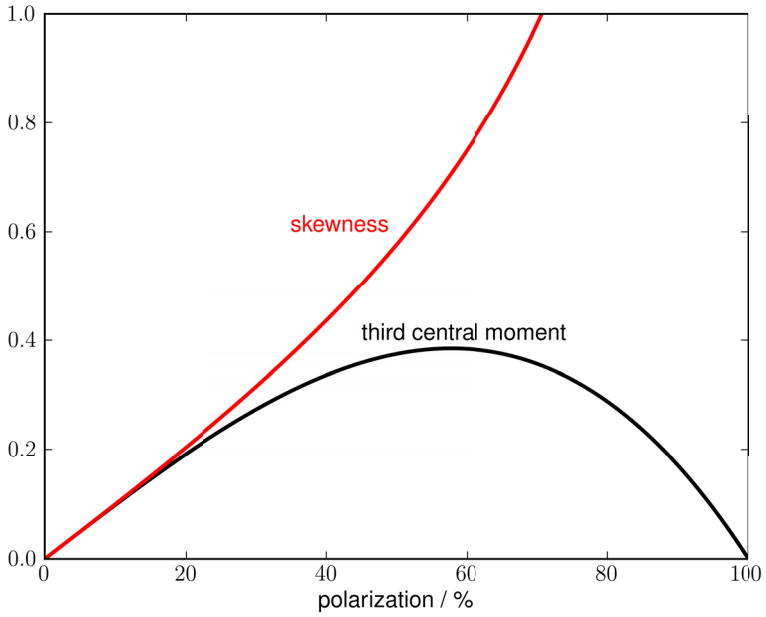

Figure 2.3.: Polarization dependent part of the central moment and the skewness as functions of the polarization for $c = 1$.

2.8. Spin-diffusion

The dipole-dipole interaction is not only responsible for the line width, but also enables the spins to perform a spin-flip, see the B term in eq. 2.10. These spin-flips do not change the total amount of magnetization.
A spin-flip requires two spins of opposite orientation, but two spins of equal orientation may be treated as if they changed places by hopping. With multiple spin-flips happening in a subsequent manner a spin might 'travel' back and forth, as in a random walk, which leads to spin diffusion.

Spin diffusion plays an important role in understanding the relaxation kinetics of hyperpolarized ^{129}Xe. Relaxation does not occur homogeneously distributed through the xenon solid, but localized, e.g. at boundaries (see section 2.3), at ^{131}Xe nuclei or at paramagnetic impurities like oxygen atoms [Sta01, Mor07, Sam05]. Therefore, most of the ^{129}Xe solid is not directly affected by these effects, but spin diffusion will 'carry' the polarization to the depolarization centers. The spin diffusion thus determines the global relaxation rate.

The T_1 relaxation time in solid ^{129}Xe at 30 K should be of the order of many hours [Sam05, Gat93, Fit99]. Peter Gerhard and Dirk Stahl from our group found much shorter times, namely 15 min for Xe/Ir and Xe/CO/Ir [Ger03] and 20 min for Xe/Ir [Sta01] respectively. In contrast Matthias Koch found 8 hr for Xe/Cu(111) [Koc06a]. These extremely short relaxation times were attributed to oxygen contamination [Ger03, Sta01] and possible spin diffusion to the substrate [Sta01]. In this thesis I am going to show that the latter can explain a wide range of relaxation times and may actually be used to measure the diffusion constant (see chapter 4.10).

In solid natural xenon, Gatzke calculated a diffusion constant of $D \approx 7.3 \times 10^{-18} m^2/s$ [Gat92]. And for isotopically enriched xenon (86% ^{129}Xe, 0.1% ^{131}Xe) Samuelson found $D \approx 2 \times 10^{-17} m^2/s$ in his experiments [Sam05]. From the distribution of impurities in the solid that act as depolarization centers, he calculated how the total amount of polarization decreases inside a sphere around a depolarization center. His model is very similar to the one proposed below. The difference is that our metal substrate is a single 2-dimensional polarization drain, where he uses many pointlike, randomly distributed polarization drains.

To model the spin diffusion from the xenon bulk to the substrate's surface we use a diffusion model from Crank [Cra79]. We assume the xenon solid to be a thin, homogeneous film of infinite extent with a thickness of $2L$. At both film surfaces the polarization should be constant zero for all times, see chapter 2.3 about the Korringa relaxation for a possible mechanism. By looking at a single half of the model we can cover the case of just one polarization drain on one side. Now for $t = 0$ the polarization should be homogeneous within the film. This means the model is actually 1-dimensional, which makes it far easier to solve the diffusion equation.

We start with Fick's second law of diffusion for the polarization P

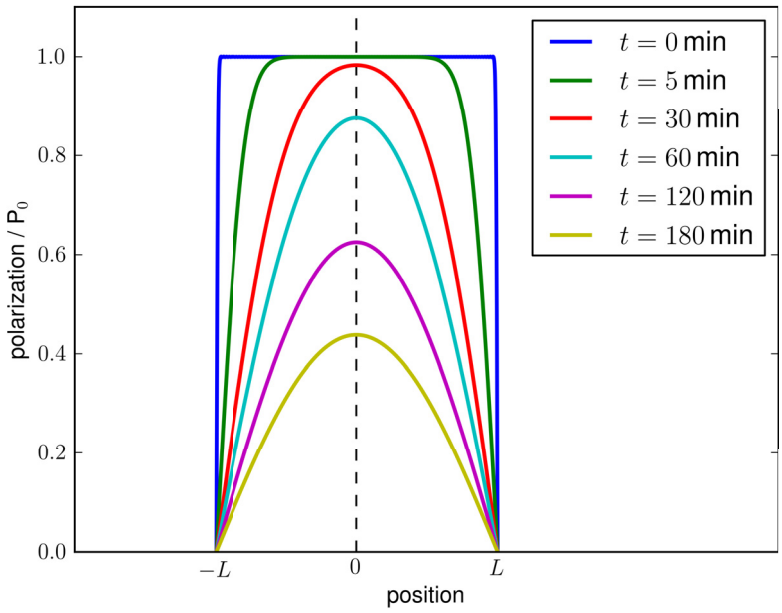

Figure 2.4.: Polarization as a function of position x and time t, see eq. 2.18 with $P_0 = 1.0$, $D = 10^{-17}\,\mathrm{m}^2/\mathrm{s}$, $L = 0.5\,\mu\mathrm{m}$ and $N = 100$ the number of summands.

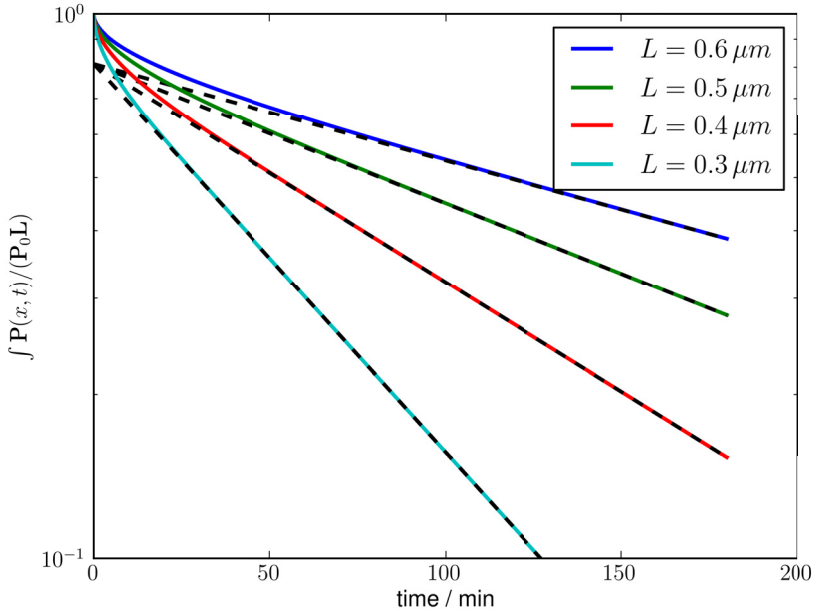

Figure 2.5.: Integral of polarization as a function of time t, see eq. 2.19 with $P_0 = 1.0$, $N = 100$, $D = 10^{-17}\,\mathrm{m}^2/\mathrm{s}$. The dashed lines show the first summand that determines the long term behavior.

$$\frac{\partial P}{\partial t} = D\frac{\partial^2 P}{\partial x^2}\,, \tag{2.16}$$

where D is the diffusion constant. To solve this differential equation one can use the separation of variables $P(x,t) = X(x)T(t)$.

$$T(t) = e^{-\lambda^2 D\, t} \qquad \text{and} \qquad X(x) = A\sin(\lambda x) + B\cos(\lambda x) \tag{2.17}$$

For the solution we use the initial conditions: The polarization equals zero at the boundaries $X(-L) = X(L) = 0$. In the beginning it is homogeneous inside $P(x,\, 0) = P_0$, and zero outside. This yields:

$$P(x,t) = \frac{4P_0}{\pi}\sum_{n=0}^{\infty}\frac{1}{2n+1}e^{-(2n+1)^2\pi^2\frac{Dt}{4L^2}}\cos\left((2n+1)\pi\frac{x}{2L}\right) \tag{2.18}$$

Figure 2.4 shows this function as it evolves in time. Since the xenon layer is a thin film, we lack the spatial resolution to probe this function. We can only detect the total amount of polarization, so we have to take the integral.

$$P_{total}(t) = \int_{-L}^{L} P(x,t)\,\mathrm{d}x = LP_0\sum_{n=0}^{\infty}\frac{16}{\pi^2(2n+1)^2}\,e^{-(2n+1)^2\pi^2\frac{Dt}{4L^2}} \tag{2.19}$$

The polarization decays as a sum of exponentials. The summation, however, is only relevant for very small times, as the n^2 term in the exponent quickly diminishes the influence of all but the first summand, see fig. 2.5.
Because the area of the xenon film is determined by the size of the single crystal, it is a constant for all measurements and LP_0 is therefore proportional to the amplitude of the NMR signal. We can use this function to fit the measurements with two parameters – one multiplicative and one for the exponent, which is proportional to the diffusion constant.

Figure 2.5 shows the shape of the total polarization relaxation curve, which has the typical shape of a diffusion limited relaxation. In the beginning the polarization drops sharply as the spins in proximity of the polarization drain relax. After the close proximity of the substrate is depolarized the spin diffusion limits the rate new polarization is transported to the substrate. If the spin diffusion were too fast or the relaxation too slow, the polarization would be homogeneous throughout the xenon solid, and the total polarization would decay exponentially [Sam05].

There remain the questions, whether the Cu(100) surface has the required relaxation properties and whether it is the only polarization drain. Section 2.3 suggests that it might be a good polarization drain and the experiments (chapter 4.10) confirm that it is, but whether this happens in the first or second monolayer is not clear. It is also not

clear what happens on the xenon surface facing the opposite direction. There might be an additional relaxation drain as well.

2.8.1. Angular dependency

The spin diffusion model from the last section is not isotropic. Because the diffusion constant D is proportional to the spin-flip rate, it contains the prefactor from the dipole Hamiltonian.

$$D \propto |1 - 3\cos^2(\theta)| \tag{2.20}$$

θ is here once more the angle between the vector that connects two spins and the static magnetic field. In the strict 1-dimensional case there is no spin diffusion if we choose the angle between the xenon film normal and the static magnetic field so that it equals the magic angle $\theta \approx 55\,^\circ$, since then the $1 - 3\cos^2(\theta)$ factor vanishes.
However a total inhibition of spin diffusion is unrealistic, as the system is not 1-dimensional and even if the direction of the film normal is blocked, slightly different directions are not. On average this means a detour and thus slower spin diffusion to the polarization drain.

2.9. Temperature programmed desorption (TPD)

Temperature programmed desorption (TPD) is a surface science method to measure the binding energy of certain atoms or molecules to a surface. The principal idea is fairly easy: One adsorbs an amount of atoms on a substrate by cooling the substrate to a temperature where its adsorption from the gas phase is larger than its desorption. If the substrate is then heated, eventually the desorption will become dominant and the adsorbate will desorb. Monitoring the rate of desorbing atoms, usually with a quadrupole mass spectrometer (QMS), as well as the temperature, one can extract the distribution of binding energies on the surface [dJ90].

Figure 2.6 shows a single TPD spectrum of xenon on a copper (100) surface from the publication by Berthold *et al.* [Ber04b]. This spectrum was recorded with a linear heating rate of 0.5 K/s. The rightmost peak at about 85 K originates from xenon directly adsorbed on the copper substrate. This layer is strongest affected by the substrate and has the highest desorption temperature. Because the peak is clearly separated from the rest, one can use its integral to calibrate the QMS signal to a single adsorbate layer – often called a monolayer (ML).
The xenon on top of the first monolayer is mostly bound to other xenon and less so to the substrate and desorbs at roughly 65 K. The third layer is almost unaffected by the substrate, with a desorption maximum at 62 K. On the left side the peak has a small shoulder from the next (incomplete) layer.

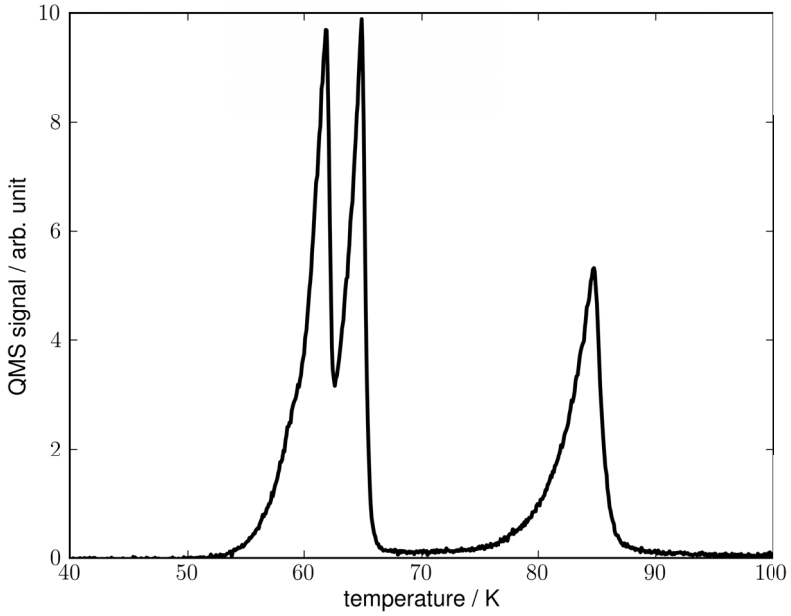

Figure 2.6.: Xenon on Cu(100) temperature programmed desorption spectrum, heating rate 0.5 K/s, adapted from [Ber04b].

In this thesis TPD is used for three purposes. First, to verify that the surface cleaning process was successful (chapter 3.5). If this isn't the case, there will either be no signal from the first ML, or a signal at a different temperature. Second, to calibrate the temperature scale (chapter 3.5). While the temperature of the first ML is strongly affected by the surface cleanliness of the substrate, the second ML is not. Its right flank gives a good calibration point for a temperature measurement. And third, to quantify the NMR signal (chapter 4.8). By using the first ML of a TPD for calibration, one can quantify the number of layers that a xenon crystal has had and relate this number to the spin polarization and the NMR amplitude.

2.10. Annealing and crystal growth

Annealing is a procedure by which a sample is heated and then cooled again. The cooling has to be slow, so that the material is always in equilibrium [AL88]. The procedure's main purpose is to reduce thermal strain as well as the number of crystal defects.

For good quality xenon crystals, growth from the liquid phase is preferable to growth from the vapor phase [Kle76]. For our setup this is not an option, as we can only grow xenon crystals directly from the vapor, and we therefore expect a high number of defects [Tot10].
Annealing the solid xenon, however, is possible, and it indeed reduces the NMR line

width, see chapter 4.9. Unfortunately, we are limited in the temperature range. Figure 2.6 shows the high temperature limit, because desorption sets in above 50 K. Annealing under constant xenon adsorption might be possible at higher temperatures. The lowest possible annealing temperature is around 30 K, set by the helium cooling system. Thus we can use a range that spans almost a factor of two in the temperature, but is still well below the xenon triple point temperature of 161.4 K [Lid96]. According to Klein and Venables this is far too low, as they recommend 0.6 of the triple point temperature – 100 K for xenon [Kle76]. This is consistent with Muskat's recommendation of "two-thirds of the melting-point temperature" as a default for other elements [Mus82]. The simulations by Totò, Schö and Jansen, however, showed annealing effects already for much lower temperatures [Tot10].

A different aspect is the temperature during growth with regards to the first monolayer. Some authors report that they needed to anneal the first monolayer before growing the rest of the crystal, otherwise they were not able to discriminate single layers in the TPD [Sch90, Ber04b].

3. Experimental setup

3.1. Overview

A successful NMR experiment on hyperpolarized ^{129}Xe requires a lot of experimental effort, which I describe in this chapter. Figure 3.1 shows an overview of our two laboratories.
To produce the hyperpolarized ^{129}Xe we use spin exchange optical pumping of rubidium, see chapter 2.2. Therefore we need a cell filled with rubidium gas to be excited with circularly polarized laser light at the Rb–D_1 wavelength. The details of the polarization apparatus, including the gas handling and protection of the highly reactive rubidium from oxidation, are described in the next section.
In our lab, the hyperpolarized xenon is transferred to the NMR experiment through a copper pipe, and then frozen onto a copper single crystal of (100) orientation. In section 3.3 the details of the transfer and the polarization loss therein are examined.
Working with a clean metal surface requires an ultra high vacuum (UHV, $P \approx 10^{-10}$ mbar) as well as a means to clean the surface after contamination, like a sputter gun – see sections 3.4 and 3.6. Section 3.5 deals with the problem of the temperature measurement under UHV and NMR conditions, which proved to be quite difficult.

The copper single crystal is inside an NMR probe, which in turn is placed inside an adjustable static magnetic field. In section 3.7 the NMR part of the setup, including the electronics, is described.

For the sake of readability the type designations of the equipment are not written in the text, but can be found in appendix D.

3.2. The polarization apparatus

The polarization apparatus was designed by Matthias Buschmann in the course of his diploma thesis [Bus11] and was constructed by the company Louwers[1]. It consists of two volumes, a small one (the polarization cell) for polarizing the xenon and a bigger one (the mixing volume) for mixing the polarized xenon with other gases (see fig. 3.2 and 3.3).
The whole unit is built from glass and differentially pumped, which means that the

[1]Louwers Glass and Ceramic Technologies, Energieweg 3A, 5527 AH Hapert, Netherlands

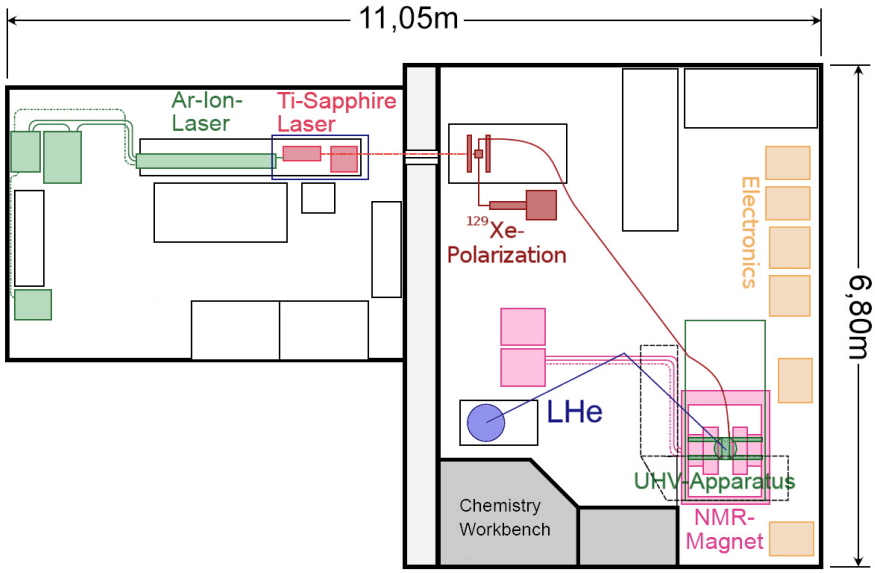

Figure 3.1.: Layout of our laboratories. On the left side (green) is the argon-ion laser that pumps the Ti:Sapphire laser (light red). The laser beam passes through the wall into the right laboratory, where it reaches the polarization apparatus (dark red). From there the polarized ^{129}Xe is transferred through a copper pipe to the UHV chamber (green), where it freezes onto a metal sample that is cooled by liquid helium (blue). The sample reaches into the NMR magnet (pink); the NMR spectrometer and the electronics are on the right wall (yellow). Original sketch in [Ger03]

xenon carrying parts are separated from the atmosphere by an additional layer with fore-vacuum. In fig. 3.3 this fore-vacuum layer is marked with green dots. Furthermore, at every stop cock, there are at least 3 O-ring seals between the atmosphere and the xenon carrying parts, to prevent contamination. The metal/glas transitions, which connect the polarization apparatus to the rest of the setup, are differentially pumped as well.
Inside the polarization cell is a small drop of about 200 mg rubidium, which is heated to 110 °C to produce rubidium vapor. Special attention has been paid to the windows of the polarization cell to be planar and free of internal stress, because through these windows a circularly polarized laser beam enters the cell and excites the rubidium. Internal stress would cause the glass to become birefringent and change the polarization of the laser light.
A pair of Helmholtz coils generates a homogeneous 13 G magnetic field around the polarization apparatus. This lifts the m_f degeneracy and causes the rubidium to get pumped into the highest(lowest) m_f state upon laser excitation. Which m_f state gets populated depends on the direction of the Helmholtz-field and the sense of the circular polarized laser light.

As shown in fig. 3.2 there are a couple of gas cylinders attached to the polarization

setup. The most important ones are the three "isotopically pure" xenon cylinders[1] and the nitrogen cylinder[2].
The xenon supply pipes are equipped with dosing valves, which we use to adjust the xenon pressure in the pumping cell. All pressure measurements are carried out with the gauge G1[3] (see fig. 3.2). For a typical experiment we fill the polarization cell with 4 mbar of ^{129}Xe (approximately 3×10^{-6} mol) and add nitrogen gas until the total pressure equals 125 mbar. The polarization cell is then closed off and illuminated with the laser for about 10 min.
An indicator of successful Rb polarization is the dependency of the laser transmission on the Helmholtz magnetic field. The total laser power is 2.4 W, but the laser spot is slightly larger than the polarization cell. The filled cell with the magnetic field turned on has a transmission of about 0.1 W/cm^2, whereas without magnetic field the transmission is less than one-tenth.

The vacuum in this part of the setup is achieved with a rotary vane pump in the high pressure regime (>0.1 mbar). To achieve a cleaner vacuum below 0.1 mbar an oil diffusion pump is used, which requires an additional rotary vane pump at its outlet. We reach a final pressure below 20×10^{-3} mbar.

Next to the polarization cell, and 12 times larger than it, is the mixing volume. For experiments with pure ^{129}Xe we can bypass it altogether. To mix polarized xenon with another gas, we dip the extension at the bottom of the mixing volume into liquid nitrogen and freeze the polarized ^{129}Xe there. We normaly don't remove the nitrogen gas from the polarization process at this stage, but it is possible to do so. Then we close the polarization cell and introduce the other gas into the mixing volume. After removal of the liquid nitrogen from the extension the ^{129}Xe thaws/evaporates and mixes with the added gas.
The xenon mixture is then transferred to the NMR setup through a 7 m long copper pipe. Before the xenon is brought into the UHV, it is advisable to remove the nitrogen gas [Rut99]. This minimizes the contamination of the vacuum chamber and enhances the temperature stability. Otherwise, the sheer amount of nitrogen gas would cause a steep temperature increase of the single crystal by more than 10 K. Without the nitrogen gas, the temperature increase is usually less than 0.1 K. Unless explicitly stated otherwise, in all experiments the nitrogen gas is removed from the xenon by freezing the xenon in a liquid nitrogen cooled trap (inside the pole shoe area of the magnet), while pumping the gaseous nitrogen, see fig. 3.9.

[1] Gas purity:
^{129}Xe: 99.988 %
^{132}Xe: 99.91 %
^{enr}Xe: 71.1 % ^{129}Xe/ 27.5 % ^{128}Xe/ 0.21 % ^{131}Xe
[2] N_2: 99.9999 %
[3] Barocel Pressure Sensor, Type 600AB, .15% accuracy, Manufacturer: Edwards High Vacuum

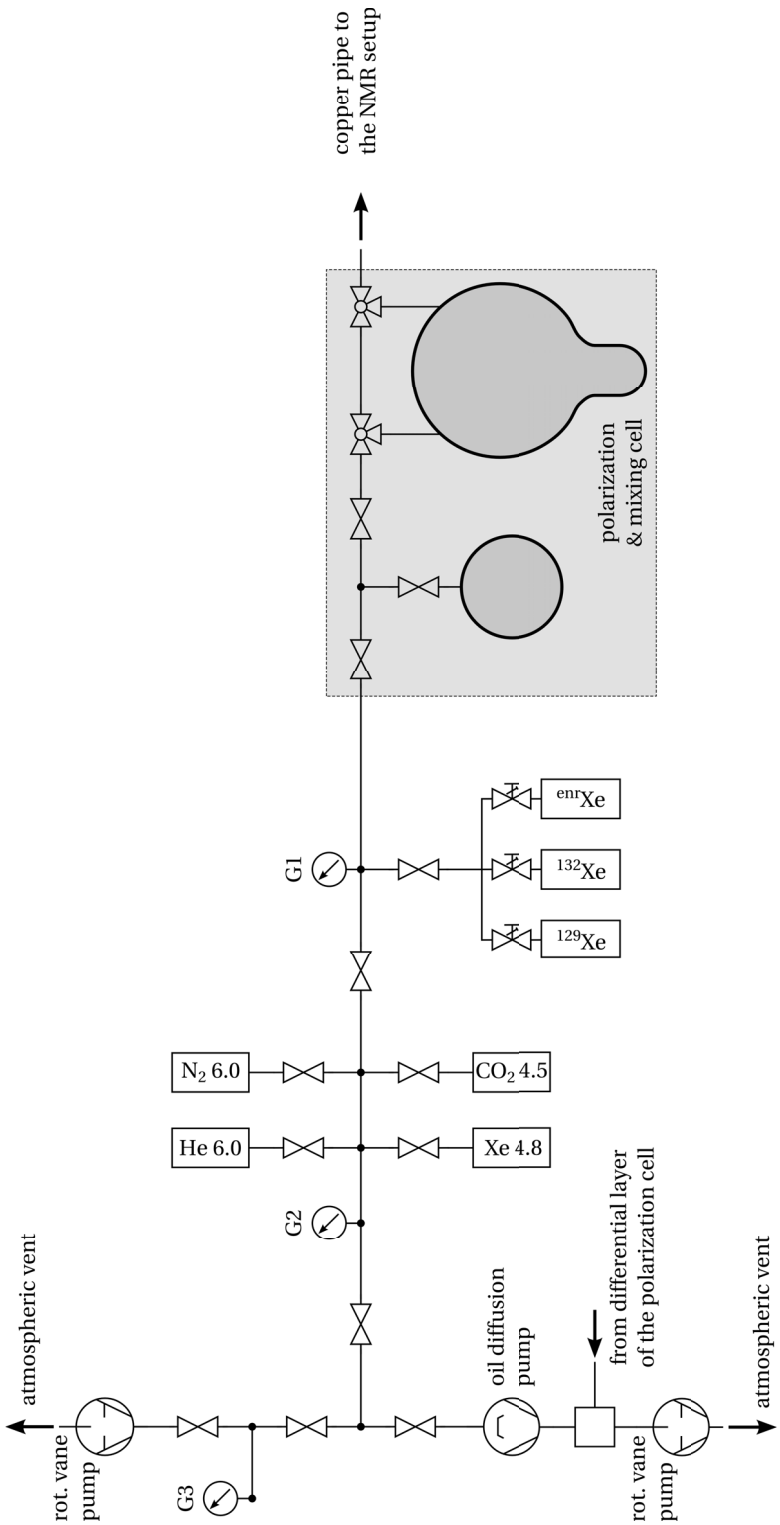

Figure 3.2.: Diagram of the vacuum pipes of the polarization apparatus. The vacuum is generated by a rotary vane pump or a combination of rotary vane pump and oil diffusion pump. The middle part shows the attached gas cylinders. Note that the three important xenon cylinders are attached separately and equipped with dosing valves. The shaded area marks the (glass-)polarization apparatus, for details see fig. 3.3. All glass valves and the glass/metal transitions are differentially pumped.

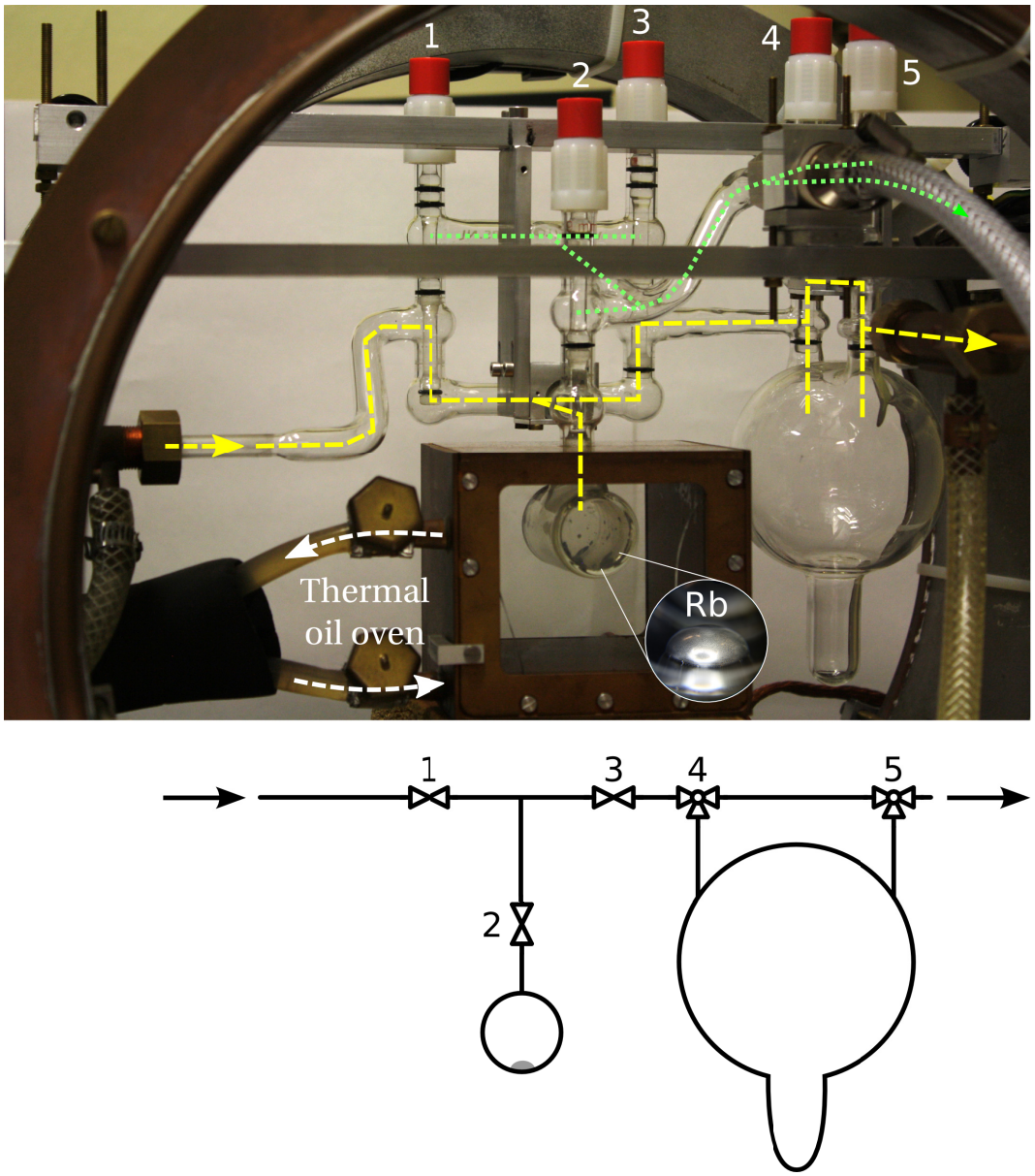

Figure 3.3.: The upper part shows a picture of the polarization apparatus. The fore-vacuum layer is marked with green dots, while the main layer, containing the polarization cell with a rubidium drop (inset) and the mixing volume, is marked with yellow dashes. Below the picture is a schematic sketch without fore-vacuum layer. An oil oven surrounding the polarization cell is used for heating the cell up to 110 °C.

3.2.1. O-ring seals in a rubidium environment

The polarization apparatus is made from 5 off-the-shelf stop cocks that are interconnected. Nonetheless we had a lot of trouble with the O-ring seals, especially the one that seals the polarization cell, valve no. 2 in fig. 3.3. The rubidium gas caused the O-ring to swell and soften. Soon the O-ring would be dragged into the gap between piston and cylinder wall, resulting in extrusion. In many cases, less than a dozen opening/closing actions were possible.
To change a defect O-ring takes a couple of hours, and includes dismounting the polarization aparatus and bringing it into an inert gas filled glovebox. Such short lifetimes made experiments almost impossible and we tested a lot of different O-ring materials to overcome the problem. Here is a short summary:
We started with viton (FKM) O-rings and high vacuum grease: The O-ring was destroyed within a day. It worked slightly better with graphite lubricant. With silicon rubber (VMQ) O-rings we had other difficulties: A blue colored O-ring leaked dye into the polarization cell. Thereafter we were not able to polarize the rubidium anymore. We also tried Perlast™, a kind of perfluoroelastomer (FFKM) that excels in chemical resistance, but nonetheless the O-ring lasted only a couple of days.
Then we came up with ethylene propylene diene monomer rubber (EPDM) in combination with very little high vacuum grease. This finally worked. We now have to replace the O-ring once a year or even less, which is tolerable.

In a redesign of the polarization cell, a static instead of a dynamic seal might be preferable.

3.3. Gas transfer

The polarized ^{129}Xe is transferred to the NMR experiment through a 7 m long copper pipe that has an inner width of 4 mm. At both ends the connectors are differentially pumped. The pipe can be evacuated with a turbomolecular pump. We found it necessary to add a fair amount of nitrogen gas during the transfer to speed up the process considerably and prohibit depolarization in the copper pipe.
With this transfer method we have seen polarizations of 50–75 %, see chapter 4.5. So, provided that one uses enough nitrogen gas, the ^{129}Xe polarization survives the transport, the freezing in high magnetic field, the N_2 pump off and the thawing.
However, for a long time polarizations that high were not routinely achieved. The polarization changed on a daily basis but, remarkably, was stable during the day. On rare occasions, we found the polarization to be negative, meaning that the magnetization was pointing the other way – all without any changes in the production setup.
The – literally – weak spot has now been identified. One position that the copper pipe passes through has close to zero magnetic field, which causes the nuclear spins to lose their orientation. Everywhere else there is a magnetic field, which is at least as strong

as the earth magnetic field.
Our provisional solution uses a multi-wire planar cable to build an air-core coil for an additional magnetic field, see fig. 3.4. The coil has a diameter of about 1 m and 150 turns. It can be operated with up to 1 A, which results in an additional field of 2 G in its center.

3.4. The Cu(100) single crystal

The NMR experiments are conducted with ^{129}Xe that is frozen onto a copper single crystal[1] with a (100) orientation. The single crystal is held in place by two rods, see fig. 3.5; one is made from tungsten and the other from a tungsten/rhenium alloy. Onto the backside we welded a copper extension for temperature measurements (see section 3.5 for details). The single crystal is heated by an electric current, which flows through the holding rods and the crystal. With a PID controller, to regulate the current, we can linearly increase the temperature or hold it at a certain value.

The single crystal is positioned at the end of a manipulator, which allows us to adjust its vertical position and turn it around the vertical axis, thus changing the angle between substrate surface and the static magnetic field. Inside the manipulator is a continuous-flow cryostat that is operated with liquid helium.

3.5. Temperature measurement

Designing a way to measure the temperature of the substrate was surprisingly difficult. We published our experiences and the final solution in [Pot14]. Here I will give only a short overview.

We use a thermocouple of type E, which is made of constantan (45% nickel - 55% copper) and chromel (90% nickel - 10% chromium). In a first attempt, we pressed the crossing point of the thermocouple against the crystal's rim (fig. 3.5) and accidentally fixed it there with a (thermocouple) constantan wire that we placed in the notch along the rim and twisted its ends to increase the tension.
This proved to be a bad idea. While the thermal contact was fine, the NMR spectra showed a drastically increased line width. The reason for this was that the thermocouple constantan wire, while nonmagnetic at room temperature, becomes ferromagnetic if cooled to liquid nitrogen temperature or below [Iny98]. Its magnetic field was strong enough to make NMR experiments on the single crystal worthless. We nonetheless wanted to use these thermocouples, because nonmagnetic thermocouples in this temperature regime are scarce and a complete change of temperature measurement method would have required a lot of modifications to the setup, possibly with unintended side effects.

[1] Purchased from MaTecK GmbH, Jülich, Germany – `www.mateck.com`

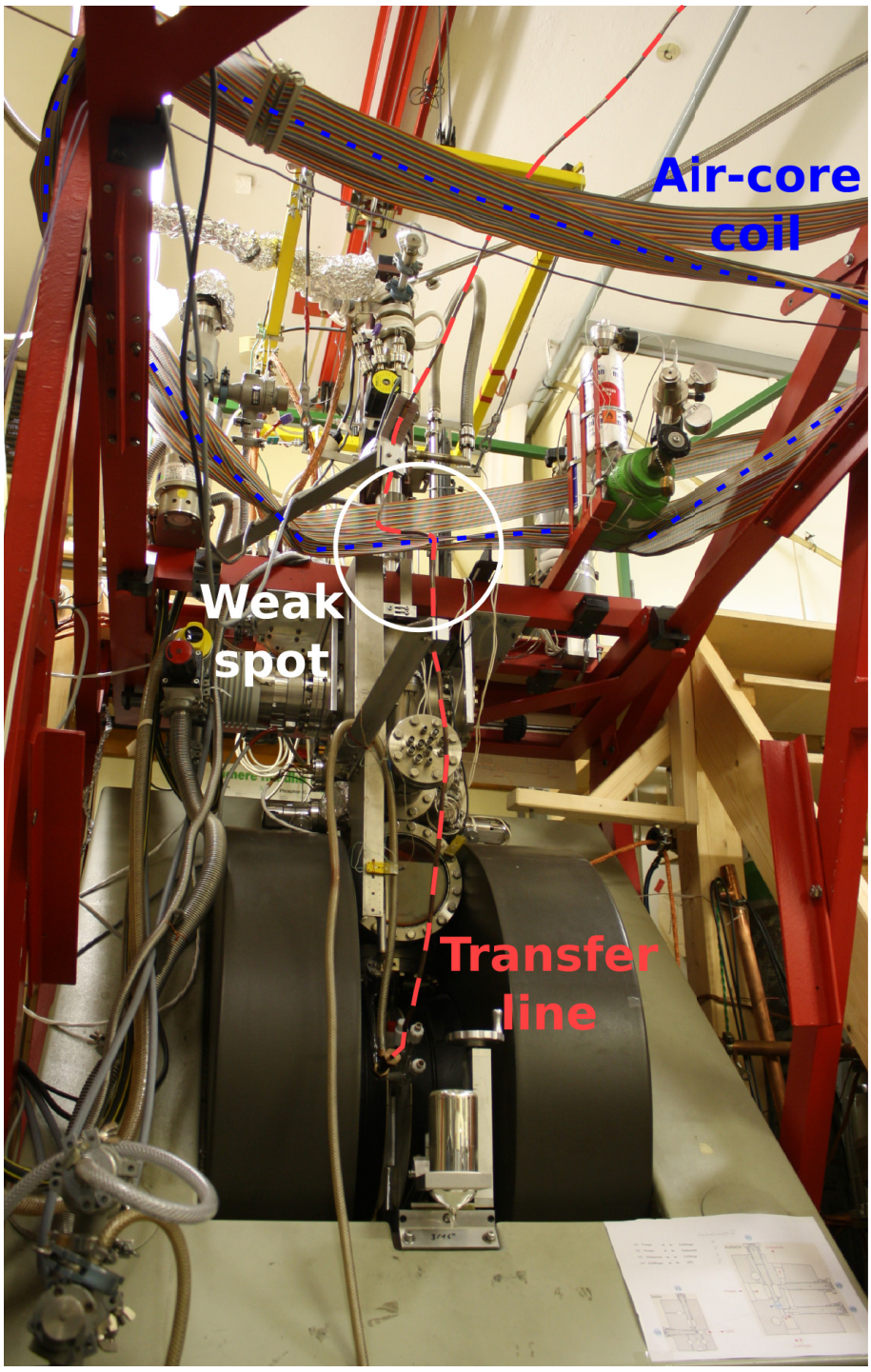

Figure 3.4.: Picture of the UHV chamber and the NMR magnet. Marked with red dashes is the xenon transfer pipe. In the center of the picture is the spot where the transfer pipe passes through a low magnetic field. Our provisional counter measure is the air-core coil that can be seen in the upper part. The coil consists of three turns of a 50 wire planar cable which, being connected in the displaced fashion, produces a 150 turns coil.

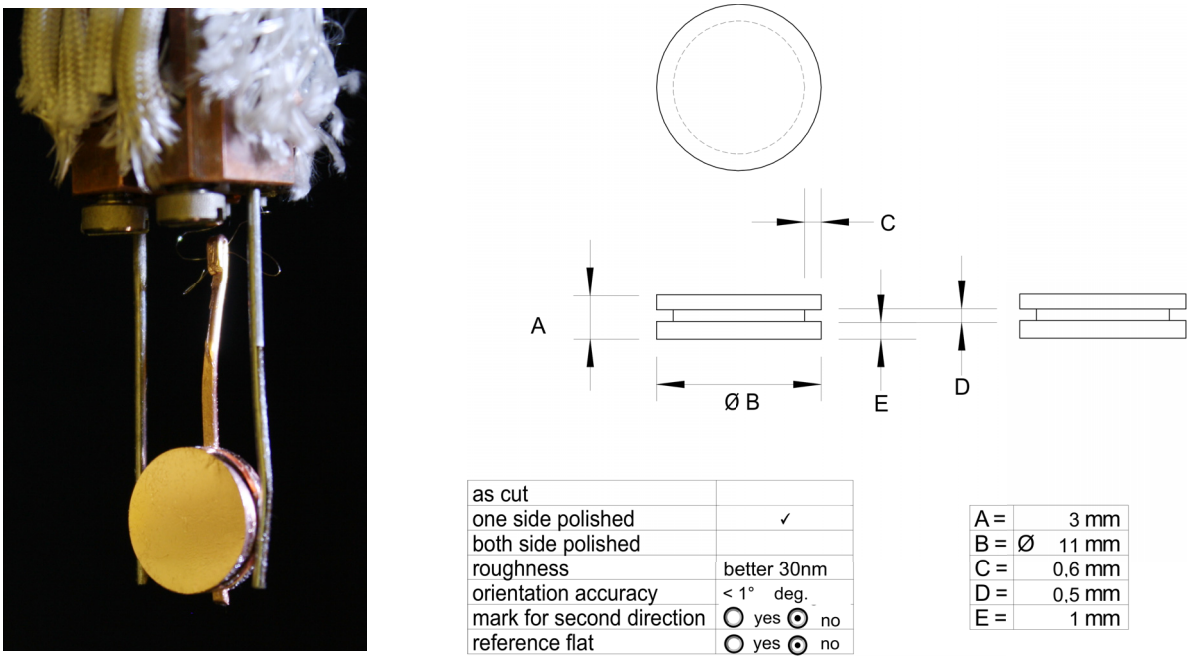

Figure 3.5.: *Left side:* Picture of the Cu(100) single crystal held by a tungsten and a tungsten/rhenium rod. In the top part, one can see the manipulator as well as the connectors for the heating current which are insulated by glass fiber. Note the copper extension on the backside of the crystal and the thermocouple at its end, which we use for temperature measurements. *Right side:* The diagram shows the dimensions of the single crystal [Mat14].

In the end we found a way to use a type E thermocouple, by laser welding a copper extension to the backside of the single crystal. The measurement then takes place at the end of the copper rod. This ensures good thermal contact and places the thermocouple 2 cm further away from the crystal, which is sufficient to suppress magnetic distortions.

The temperature measurement has to be calibrated. For this purpose, we use TPD, see chapter 2.9.
First we clean the surface of the single crystal with argon ion sputtering, for details see section 3.6. Then we cool the single crystal to 30 K, and with a constant background pressure of 5.0×10^{-7} mbar we dose approximately 3 monolayers of natural xenon onto the single crystal over the course of 40 sec. The temperature is then increased linearly to 100 K while the quadrupole mass spectrometer records the amount of ^{129}Xe that desorbs. If the cleaning process was successful, we can separate the first, second and third monolayer.
For calibration we then shift our spectrum, such that the falling edge of the second layer coincides with the reference spectrum from the literature [Ber04b], see fig. 3.6.

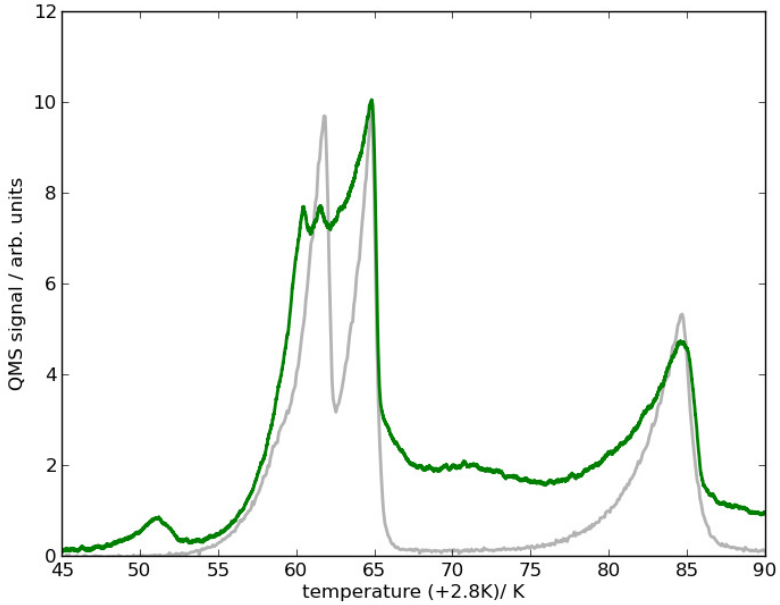

Figure 3.6.: *Green solid line:* TPD-spectrum of ^{129}Xe in natural xenon on Cu(100). Note that the temperature axis is shifted by 2.8 K to fit the falling edge of the second monolayer to the corresponding part of the grey spectrum, which has been adapted from literature [Ber04b].

3.5.1. Effect of a magnetic field on a thermocouple

If a magnetic thermocouple is placed in a magnetic field gradient and in a temperature gradient at the same time, an additional electromotive force (emf) along the thermocouple arises which alters the temperature reading [Kol77, Beg14]. It is impossible to predict the exact temperature deviation in a real experimental setup, because it strongly depends on the setup's geometry.
For some of our experiments an accurate temperature measurement is required and this effect has to be taken into account as it is not covered by the calibration, which takes place outside the magnetic field (see section 3.5). A simple way to measure the effect of the magnetic field on the thermocouple, is to monitor the temperature during the NMR magnet's power-on.
Figure 3.7 shows the temperature deviation (at $T \approx 30\,\mathrm{K}$) resulting from the magnetic field. At $t = 1\,\mathrm{min}$ the magnet was switched on. Afterwards the field strength was increased every 0.5 min, until it reached the required field for ^{129}Xe measurements ($B \approx 2\,\mathrm{T}$) at 3.5 min. At this point the temperature was 1.4 K below its original value. At $t = 4\,\mathrm{min}$ the magnetic field was turned down again and the magnet was switched off, after which the temperature reading returned to its original value.

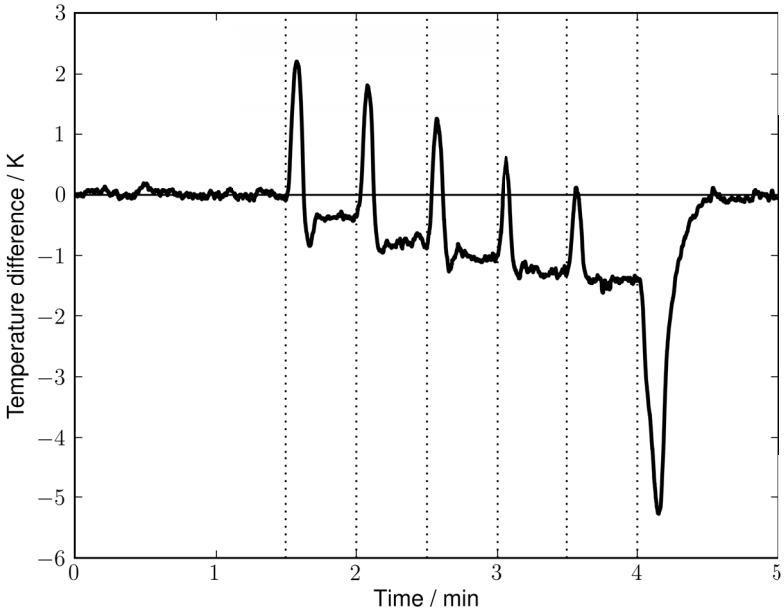

Figure 3.7.: Temperature deviation during the NMR magnet's power-on and power-off. The dotted lines mark the times the magnet field strength was altered. More details are described in the text.

3.6. The cleaning procedure

The copper single crystal has a highly reactive surface which gets contaminated over time, even in the UHV. Before conducting surface sensitive experiments it is necessary to remove this contamination. For this purpose we use the following sputtering procedure, which loosely follows the procedure described in [Mus82]:
At a constant background pressure of 5×10^{-6} mbar argon we perform three cycles of 10 min sputtering at 300 K, followed by 3 min annealing at 800 K. The acceleration voltages are 1.5 kV in the first, 1.0 kV in the second and 0.5 kV in the last cycle. However the last cycle may be skipped if the last cleaning was only a couple of days ago.

3.7. The NMR part

The NMR experiment starts and ends with the spectrometer. Fig. 3.8 shows its wiring into the setup. The spectrometer generates a (voltage) pulse of desired frequency, length, shape, phase and amplitude, where the maximum possible amplitude is 1 V. The pulse is first attenuated by a variable factor (usually 14 dB) and then amplified with a linear pulse power amplifier (LPPA) by a constant factor of 60 dB. Afterwards the pulse passes the quarter wave cable to reach the probe (fig. 3.9), where it resonates in the NMR coil,

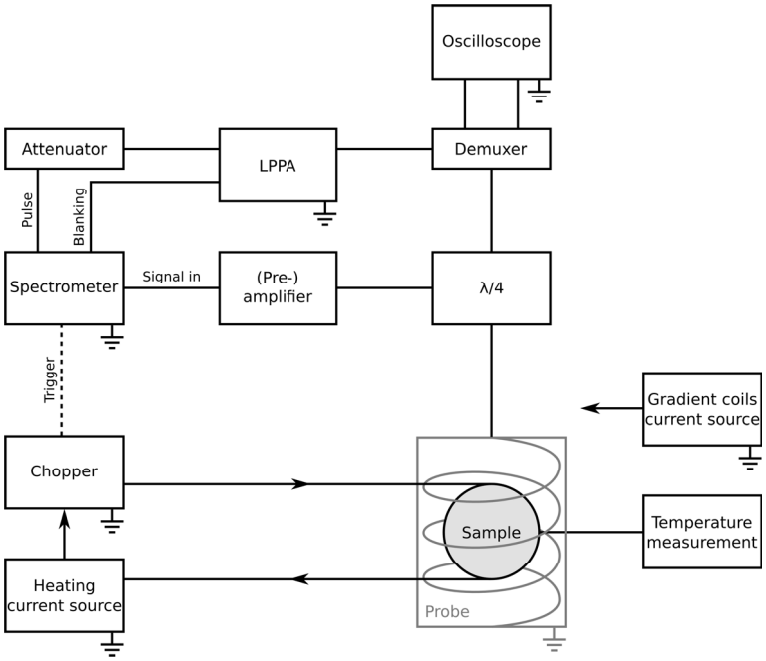

Figure 3.8.: Sketch of the electronic devices and their connections. To the lower right is the probe (see fig. 3.9). Marked with ground symbols are those devices that are electrically grounded. This information helps to identify ground loops.

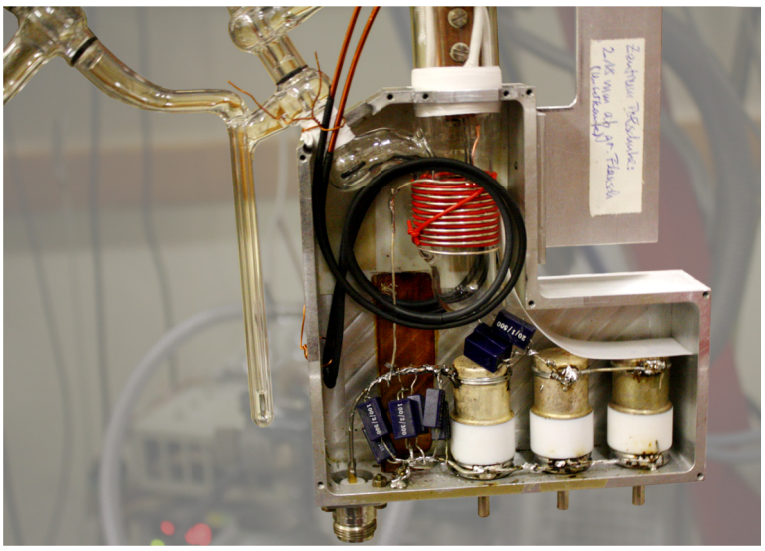

Figure 3.9.: Picture of the aluminum probe with removed cover plate. The probe is built around the glass vacuum chamber. In the center is the NMR coil that is wrapped around the glass. Below the coil are capacitors, three of which are variable. We added gradient coils and covered them with heat-shrink tubing (black) to suppress discharges from the high voltage NMR coil. To the left of the probe is a glass finger with a thin glass tube inside, which allows us to separate xenon and nitrogen by cooling the finger with liquid nitrogen.

and thus gets further amplified.
The nuclei's response signal is received by the same coil and transferred through the quarter wave cable to the preamplifiers. During this, the LPPA's output is grounded by a blanking signal from the spectrometer, so as to reduce noise. The quarter wave cable serves two purposes: first, it lets the pulse pass to the probe, while ensuring that the preamplifiers are not damaged by the high voltage. Second, to let the response pass to the preamplifiers without signal loss. The whole setup is preset to 23.275 MHz. This is the Larmor frequency of ^{129}Xe at 1.97 T. If we want to measure a different element/isotope, it is necessary to change the magnetic field accordingly.
After the NMR signal is preamplified it reaches the spectrometer, where it is further amplified, downsampled in the quadrature detection, filtered and finally sent to a computer. The spectrometer software that controls the whole process was designed and programmed by Anuschka Schaffner. Please refer to her work [Sch15] for further details.

3.8. Gradient coils

Magnetic field gradients are frequently used to achieve spatial resolution in NMR experiments. Our setup is equipped with such coils as well. Fig. 3.9 shows a picture of the opened probe, including the gradient coils. The gradient coils are oriented collinear with the static magnetic field and have two turns each. With a radius of $R \approx 30\,\text{mm}$ and a distance of $a \approx 25\,\text{mm}$ in between, they are close to anti-Helmholtz geometry.

Starting from Biot-Savart's law for two coils with N turns at a distance a from each other, we get a magnetic field on the symmetry axis of

$$B(x) = \frac{\mu_0}{2} R^2 I N \left[\frac{1}{\left(\left(x + \frac{a}{2} \right)^2 + R^2 \right)^{3/2}} - \frac{1}{\left(\left(x - \frac{a}{2} \right)^2 + R^2 \right)^{3/2}} \right] .$$

μ_0 is the vacuum permeability, and the point of origin has been placed centered between both coils. Taking the first derivative we get a gradient at $x = 0$ of

$$\frac{1}{I} \frac{\partial B}{\partial x}(x = 0) = 2.34 \times 10^{-3} \, \frac{\text{T}}{\text{Am}} \mathrel{\widehat{=}} 27.6 \, \frac{\text{kHz}}{\text{Am}} .$$

Thus, the resonance frequency of two ^{129}Xe nuclei, which are 1 cm apart along the gradient, will shift by 276 Hz for every ampere of current passing through the coils.

4. Experiments

This chapter describes the experiments and their analysis. It is important to keep in mind that the NMR-setup is preset to 23.275 MHz, and may only be changed by a few kilohertz.

4.1. Boron NMR

A common problem of experimental setups as complex as ours is the difficulty to find faults. If a recorded ^{129}Xe NMR spectrum shows no signal, it is difficult to locate the actual point of failure, for the possibilities are manifold. Here is a short list of things that went wrong during one time or another: the laser being off resonance, oxidized rubidium, polarization loss during transfer, cryo trap not cold enough, probe cable damaged or not connected, pulse amplifier broken, spectrometer software/hardware faulty. Keeping in mind that the most simple ^{129}Xe NMR experiment takes about 15 minutes to conduct, trouble shooting can be tedious.
To narrow down the possibilities it is necessary to check the setup at intermediate points, preferably without changing anything. Unfortunately, these intermediate points are rare. The ones we used so far include, first, the laser transmission through the polarization cell and its dependency on the Helmholtz magnetic field (see section 3.2). At this point we can verify that the laser works, that it is on resonance and that there is sufficient rubidium vapor. Second, by monitoring the UHV pressure we can confirm that a gas transfer took place and its quantity was within bounds. Third, an oscilloscope in the NMR circuit can detect the pulse which is sent to the probe (see fig. 3.8).
Nonetheless we were lacking a test to validate with certainty that the NMR equipment was working. The only test that comes close is sodium spectroscopy on NaCl solutions. This however requires a different probe. To fill this gap, we experimented with a small NaCl(aq) sample in the field outside of the NMR coil, but the results were not convincing. Spectroscopy on the copper single crystal would be nice, but the skin effect prevents it.

Finally, we came up with an unexpected candidate: boron. ^{11}B has some nice NMR properties (see table 4.1) and is used in significant amounts in borosilicate glass [Dur14], the material the vacuum chamber is made of (see also picture of the probe, fig. 3.9). On the downside, it is located neither in the center of the static magnetic field nor in the center of the NMR coil, it actually sticks out of the coil on both sides. Furthermore, the fixed frequency setup means that we have to change the static magnetic field. On the

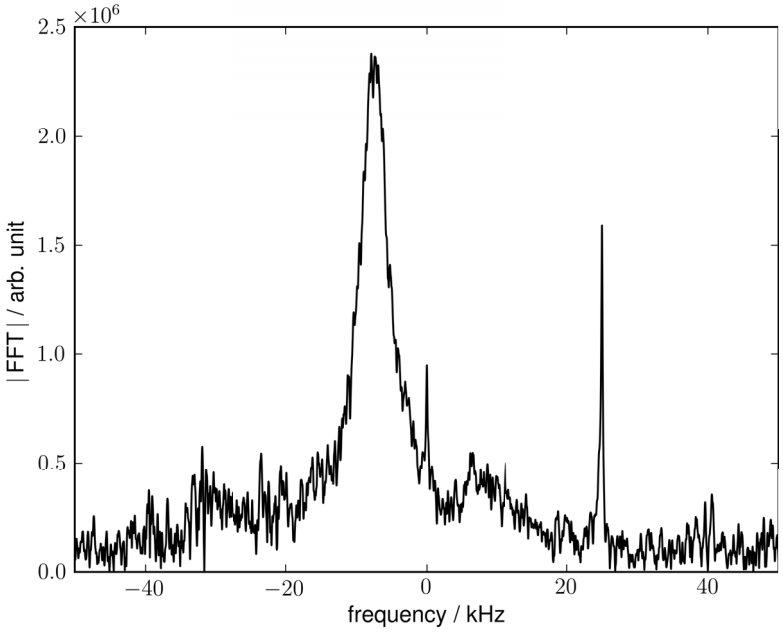

Figure 4.1.: Spectrum of the ^{11}B in the UHV glass tube. The time required for this spectrum was 5 min. The time constant for the exponential windowing was 2 ms. Mean of 4x64 acquisitions with phase cycling (CYCLOPS, see [Ger87, p. 309-311]). The spike at 25 kHz is an RF artifact.

spin	3/2
abundance	80.1%
mag. moment	$2.688649\,\mu_{\mathrm{N}}$
quad. moment	$4.059\,\mathrm{fm}^2$
gyrom. ratio	$8.584707 \times 10^7\,\mathrm{rad/sT}$

Table 4.1.: NMR properties of ^{11}B. [Bru13]

upside, the NMR coil is wound around said glass and there is plenty of it to perform spectroscopy on.

Boron has a spin of 3/2 and its borosilicate spectra have notoriously broad resonances [Tur86, Bru13], which are even broader in our case for the mentioned geometric reasons. In order to reach satisfying signal-to-noise ratios several repetitions are therefore necessary. The spectrum in fig. 4.1 is the sum of 256 acquisitions and took about 5 minutes time.

To conclude, the boron NMR allows us to test the proper functioning of the NMR equipment in 10 minutes flat.

4.2. Gas on the back side of the crystal

For many experiments, but especially for the spin diffusion measurements described in section 4.10, it is necessary to assume that the xenon gas freezes onto the front side of the single crystal. Systematic errors occur if a significant amount freezes onto the back side of the single crystal, where no clean Cu(100) surface is present.
It is reasonable to assume that most xenon freezes onto the front side, because the gas is under low pressure when entering the UHV and its angular distribution should be a cosine lobe. Still it would be preferable to have a measurement that determines the amount of xenon on the back side. After installing the gradient coils, this experiment became feasible. By rotating the single crystal we can align its surface normal colinear with the static magnetic field and the gradient. If the gradient is strong enough, front- and back side will be exposed to different magnetic fields, and the NMR will show two distinct resonance lines.

To verify that the gradient coils work as intended, we started with a measurement in the standard position, with the single crystal normal perpendicular to the gradient. As expected, the line width increased with the gradient. The resonance shape can be fitted with an ellipse, see fig 4.2. Clearly the line width and thus the gradient exceeds the estimation in eq. 3.8 by a factor of 5. The probable reason is the iron from the electromagnet nearby, or alternatively an artifact of the electromagnet's response to the gradient field.
However, we can use fig. 4.2 as a calibration and compare it to the case, where the single crystal normal is colinear with the gradient, see fig. 4.3. Here one expects to find two resonances in the spectrum, one from the front and one from the back side. By fitting two Lorentzians to the spectrum we can assess that the back side resonance has less than 5 % of the front side amplitude.

4.3. Windowing

Windowing in the NMR context means multiplying the FID with a (window) function that emphasizes certain parts of the FID. It is a standard tool in NMR signal processing to eliminate artifacts, change the peak shape and enhance the resolution or the signal to noise ratio [Ber04a]. There are plenty of window shapes for all kind of purposes, however, in this thesis only the exponential window function is used.

By multiplying the FID with an exponential decay, one trades (spectral) resolution for a better signal to noise ratio. The effect's strength can be adjusted by variation of the decay constant.
This can be understood in the following way: If the acquisition time is much larger than the actual FID, a major part of the recorded data contains only noise. By shifting weight to the early data parts, where the signal to noise ratio is best, one enhances the signal and at the same time suppresses the parts with predominant noise. But all enhancement

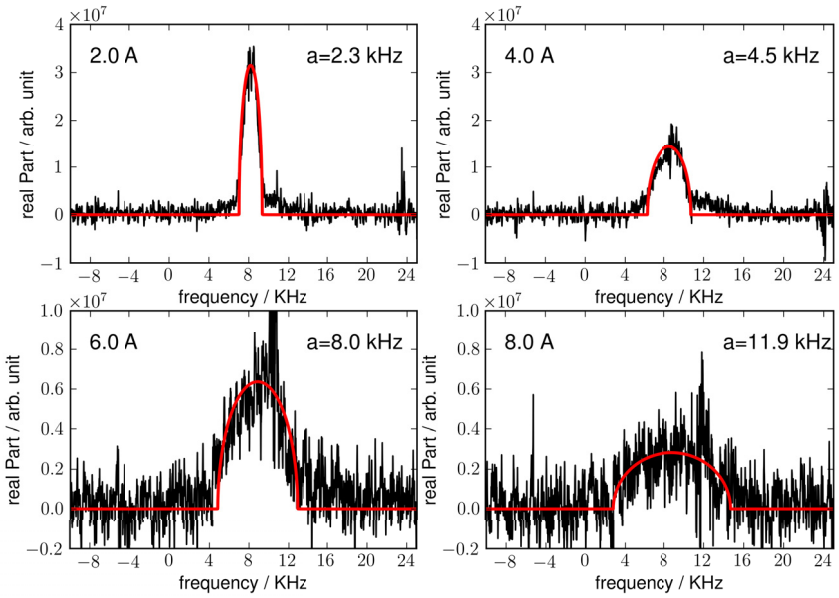

Figure 4.2.: Shape of the resonance in various gradient fields with the single crystal surface normal oriented perpendicular to the gradient field. The resonance line is fitted with an ellipse, the length of its (minor) frequency-axis a is denoted in the diagram, as well as the gradient coil current.

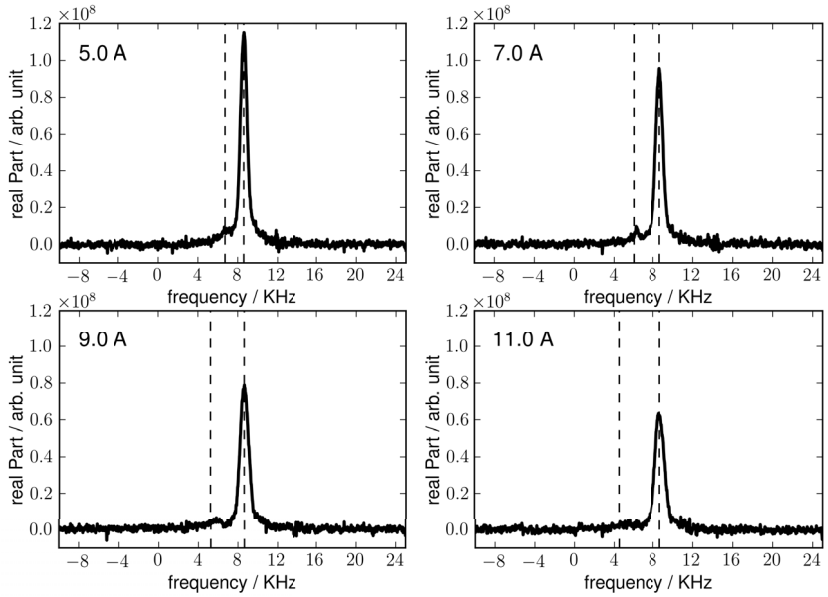

Figure 4.3.: Shape of the resonance in various gradient fields with the single crystal normal oriented colinear with the gradient field. Dashed lines indicate the resonance center and the expected position of the back side resonance line.

comes at a price. If the resonance line shape deviates from a Lorentzian, then the windowing will alter its shape; if the shape is already Lorentzian, then the windowing will broaden the resonance line by an additional $\frac{1}{\pi\tau}$, where τ is the exponential decay constant.

Since the line width of solid xenon is several hundred Hertz, a mild increase is often tolerable, and can be acounted for. Unless otherwise noted, all spectra in this thesis are multiplied with an 10 ms exponential decay [$\times \exp(-t/10\,\mathrm{ms})$], which increases the line width by 32 Hz.

4.4. Amplitude measurement

The determination of the 'strength' of the resonance line is of vital importance for many research questions. There are different ways to the calculation of the amplitude from a measured FID. Commonly one uses a Fast-Fourier-transform (FFT) of the raw data and a Lorentzian/Gaussian fit of the resonance line in frequency space. There are at least four common ways to fit the spectrum. One can either fit the absorption spectrum (the real part of the FFT), which requires a phase correction, and thus discarding the imaginary part, or use a complex valued fit. As a third option one can fit the amplitude spectrum (the modulus/absolute value of real and imaginary part), where one has to be careful because the modulus of a complex Lorentzian is not of Lorentzian form. And last, it is possible to fit the power spectrum (the modulus squared). Incidentally, the modulus squared of a complex Lorentzian is again of Lorentzian shape. A disadvantage – or sometimes also an advantage of this method – is the higher weight attributed to the peak in the power spectrum (see also [Hem96]).
Since our resonance lines are asymmetric, all these methods produce systematic errors. Worse, the result depends on the specific parameters used for the measurement (number of points recorded and their spacing, dead time, ...) as well as the windowing function and parameters. Therefore we use a direct fit of the modulus of the FID that is independent of these parameters.

For this we take the square root of the quadratic sums of the real and imaginary part, see fig. 4.4. A Lorentzian line shape would manifest itself as an exponential decay in the time domain. Even though the resonance is not truly of Lorentzian shape, it is close enough to yield reliable amplitudes when the FID is fitted with an exponential decay: $f(t) = A \cdot exp(-B\,t) + C$, where A, B and C are fit constants. As initial guess we use the average of the last half of data points as additive constant C, the first data point as initial amplitude A, and 0.5 ms as decay constant B.
To take the dead-time of the spectrometer into account (the delay between the end of the pulse and the start of the recording, which is 40 μs in all our measurements), we shift the time axis by the dead-time. Thus the zero time coincides with the end of the pulse.

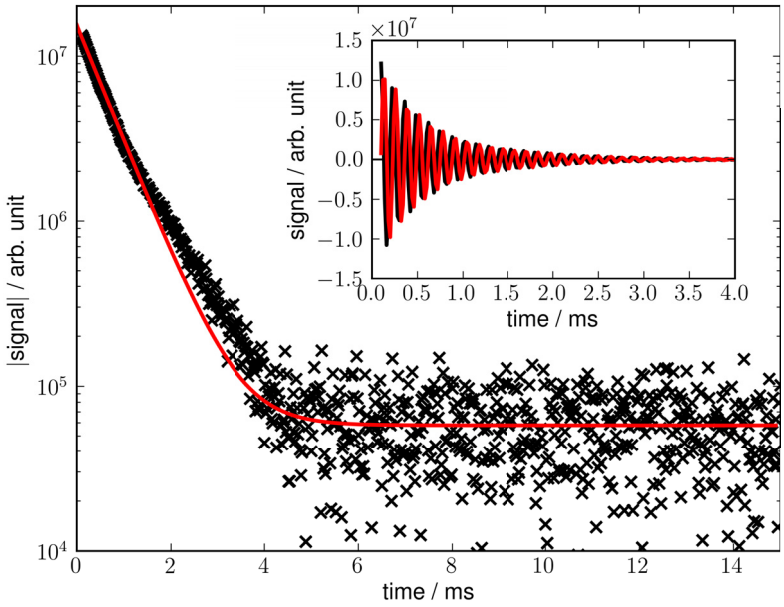

Figure 4.4.: Semi-logarithmic plot of the modulus of the FID and its exponential fit. The inset shows the complex values.

4.5. Polarization measurement

In this section, I describe the measurement of the xenon polarization. As described in the corresponding theory chapter 2.6, we make use of the line shift that the polarization causes. With a series of small angle pulses ($\varphi \approx 10\,° \ldots 20\,°$) we measure the change of resonance position and amplitude as the polarization is depleted with each consecutive pulse. To extract the resonance frequency we use a Lorentzian fit to the power spectrum. This way the peak is enhanced and the asymmetry suppressed. Furthermore it is consistent with prior experiments by Matthias Koch and Peter Gerhard [Ger03, Koc06a].
Figure 4.5 shows the line shift and the amplitude variation of a small angle measurement. The polarization is then determined from an exponential fit, in which a shift of 470 Hz corresponds to 100 % polarization, see chapter 2.6.
The advantage of this method is its self-calibration, because the fit yields all relevant parameters: the cosine of the pulse angle, the frequency in the limit of 0 % polarization and the frequency shift of the first spectrum.
One fatal disadvantage of this method remains: its destructive nature. By measuring the polarization we destroy it; its value is only known afterwards. One way to circumvent this flaw is to use only one pulse. This single pulse will deplete the polarization only by 2 % – even less might be possible. But in order to calculate the line shift, one needs prior knowledge of the 0 % frequency limit, e.g. from a separate measurement like the one shown in fig. 4.5. Of course this works best with high polarization and higher amounts of ^{129}Xe nuclei to increase the signal to noise ratio.

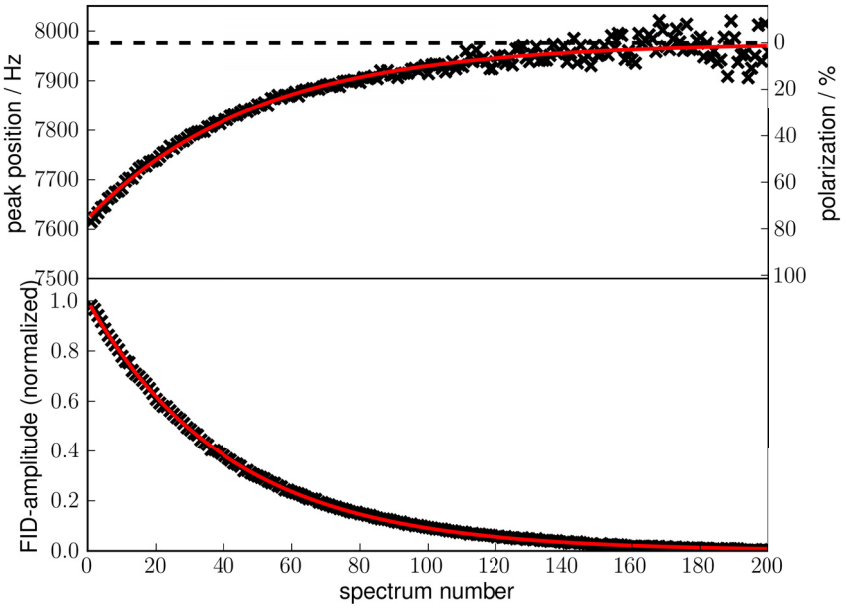

Figure 4.5.: Polarization measurement with a series of small angle pulses. Frequency shift and amplitude are both fitted with an exponential decay. From the amplitude fit we get the pulse angle $\phi \approx 12.0\,°$. The total frequency shift is 361 Hz, which equals 77 % polarization.

With a slightly more complicated pulse sequence ($X_{180°}$ – $X_{10°}$ – acq./ $X_{180°}$ – $X_{10°}$ – acq.) one can omit a separate measurement. This pulse sequence uses a 180 ° pulse to turn the magnetization to the $-z$ direction, followed by a small angle pulse to measure the resonance frequency. If this is repeated a second time, the magnetization will return to its original position and one gets two frequency shifts, one positive and one negative. The polarization shift can then be deduced. However, this sequence will also cost more polarization than a single pulse. Less so if one uses a composite 180 ° pulse [Ber04a].

4.6. Resonance line width as a function of polarization

The resonance width is a function of the $^{129}Xe/^{132}Xe$ ratio and the polarization, as shown in chapter 2.7. The second moment has the form:

$$\langle \nu^2 \rangle \propto c - c^2 P^2 \tag{4.1}$$

In a polarization measurement as described in the last section we have already acquired the necessary data and fitted the power spectrum with a Lorentzian. From this fit we can extract the full width at half maximum (FWHM). A series of small angle measurements thus yields the FWHM for all polarizations from the maximum polarization the

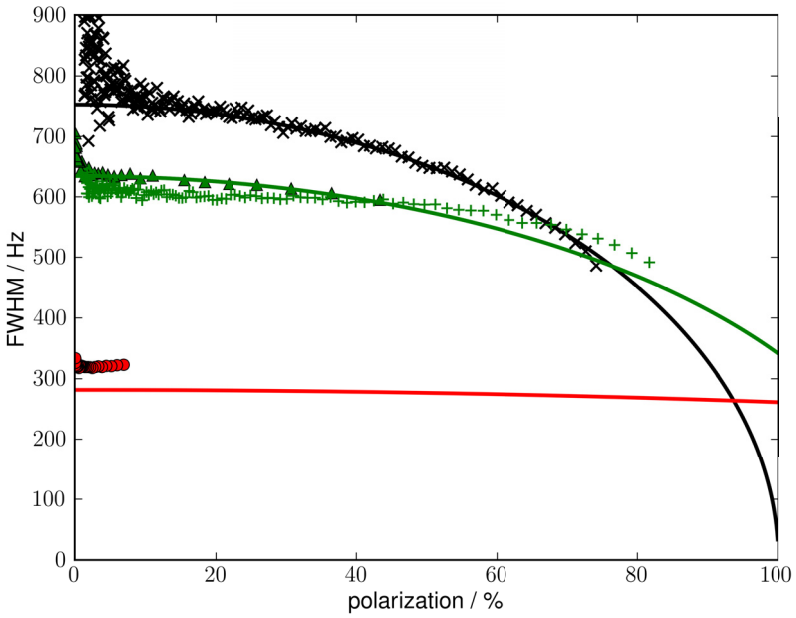

Figure 4.6.: Resonance width as a function of polarization for various concentrations. *Black:* ^{129}Xe concentration 1.0, *green:* enriched 0.71 and *red:* mixture 0.23. The *green plus markers* display a measurement from Matthias Koch [Koc06a]. The measurement with 0.23 ^{129}Xe content (red) shows a very small line shift, making the determination of the polarization unreliable. Its ^{129}Xe concentration was extracted from a isothermal TPD with a simultanious mass sweep of the QMS.

sample had in the beginning to 0 %. Figure 4.6 shows the FWHM as a function of the polarization compared to the theory. The theoretical curves were calculated from the second moment (eq. 2.13) under the assumption of a Gaussian line, because a Lorentzian has no second moment. Therefore systematic error might arise, both in the theory and in the fit of the experimental data.

A direct calculation of the moments from the spectra is not possible due to numerical instabilities. Especially the second and third moment depend strongly on the tails of the resonance line, making them vulnerable to base line effects and artifacts. The calculation in the time domain is also not feasible since it requires higher order derivatives of the FID at $t = 0$, which is experimentally not accessible due to the dead time of the spectrometer [Par73]; the integration techniques proposed in the paper were not fruitful either.

4.7. Resonance line asymmetry as function of the polarization

As shown in chapter 2.5, the resonance line shape depends on the polarization. The third moment that is closely related to the asymmetry of the resonance line is proportional to $P(1-P^2)$ for pure ^{129}Xe.

In a first step to quantify the asymmetry and compare experiment and theory, we use the asymmetry index α as a measure. This method was used for analyzing XPS spectra before computers became commonplace [Don70]. The asymmetry index is defined as the ratio of the left half maximum width and the right half maximum width (see fig. 4.7 for the construction).

$$\alpha = \frac{\left|\nu_{max} - \nu_{max/2,left}\right|}{\left|\nu_{max} - \nu_{max/2,right}\right|} \tag{4.2}$$

For this analysis we use the amplitude spectra (modulus) in order to be independent of phase corrections. First, the maximum is estimated by taking the frequency of the maximum in a 2.5 KHz window around the expected position.
To get a better approximation, a quadratic fit is then used 40 points around the estimated location. A second quadratic fit is used with its fit window centered on the output of the first fit – this ensures the fit to be less prone to errors resulting from the asymmetry. This fit yields the location and the value of the spectrum's maximum.
In the next step, the value of the maximum determines the 'half maximum' value. The resonance flanks are estimated by taking the point in the spectrum closest to the half maximum value. This is done for the left and right side of the peak separately. The result is improved with a linear regression of 20 points around the estimation value. Equation 4.2 then yields the asymmetry index.

Figure 4.8 shows the top view of amplitude spectra of a polarization measurement series. The polarization and thus the amplitude decreases with every spectrum from top to bottom. The black lines indicate the positions of the maximum and the half maxima. One clearly sees the resonance becoming more symmetric as its amplitude decreases. Comparing the asymmetry index with the prediction for the third moment, shows similar trends, see fig. 4.9.

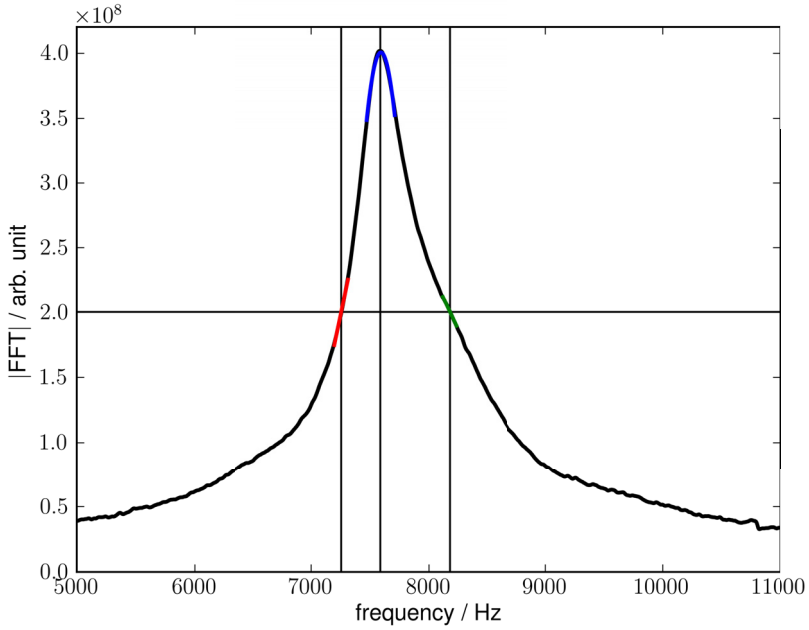

Figure 4.7.: In order to calculate the asymmetry index the maximum of the spectrum (black) is fitted with a quadratic function (blue). The result is used to fit the left and right flank with a linear regression (red and green). Vertical lines indicate the intersection points with the half maximum.

Because the third central moment is not invertible, it is favorable to use the skewness instead, see eq. 2.15. Appendix A describes a way to fit the resonance line with the product of two Lorentzians, and how to compute the central moments from the fit. The skewness proves to be remarkably stable and fit-error tolerant, as it compensates errors from the second and third central moment. Figure 4.10 shows the skewness from the measurements, and the theoretical curve from eq. 2.15 scaled with a factor of 0.73[1].
It is important to keep in mind that deviations in the high polarization regime – to a lesser extent – also occur in the polarization measurement described in section 4.5, which was used to calculate the polarization axis in fig. 4.10. Therefore it is unclear at this point whether our usual polarization measurement or the skewness in this figure is more reliable to determine the polarization. As they are only about 5 percentage points apart, this is difficult to judge. Conversely, considering its stability, the skewness can be used to calculate the polarization from a single spectrum, provided the scaling factor is correct.

[1]Considering the complexity of its constituents, this is remarkably close to unity; and suspiciously close to $3/4 = I(I+1)$.

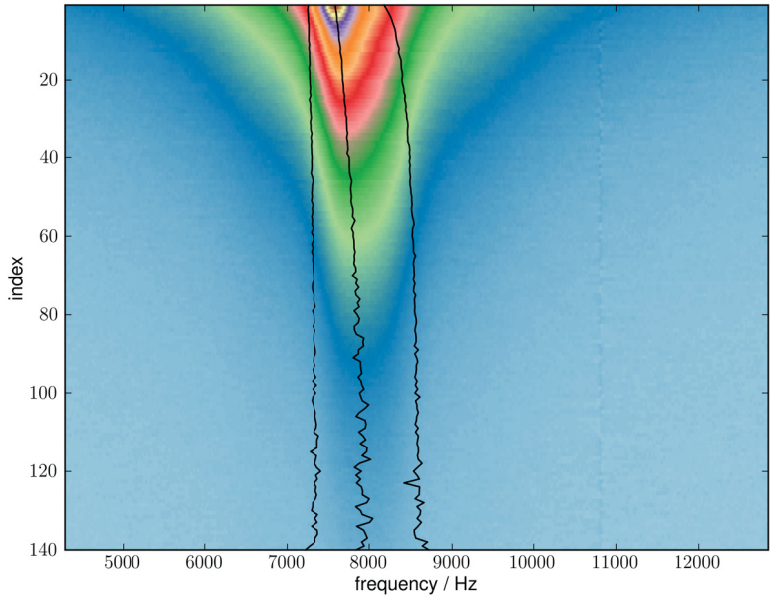

Figure 4.8.: Contour plot of the modulus of a series of spectra. With increasing spectrum index, the polarization decreases. The three black curves show the left half maximum, the center and the right half maximum as fitted, see fig. 4.7.

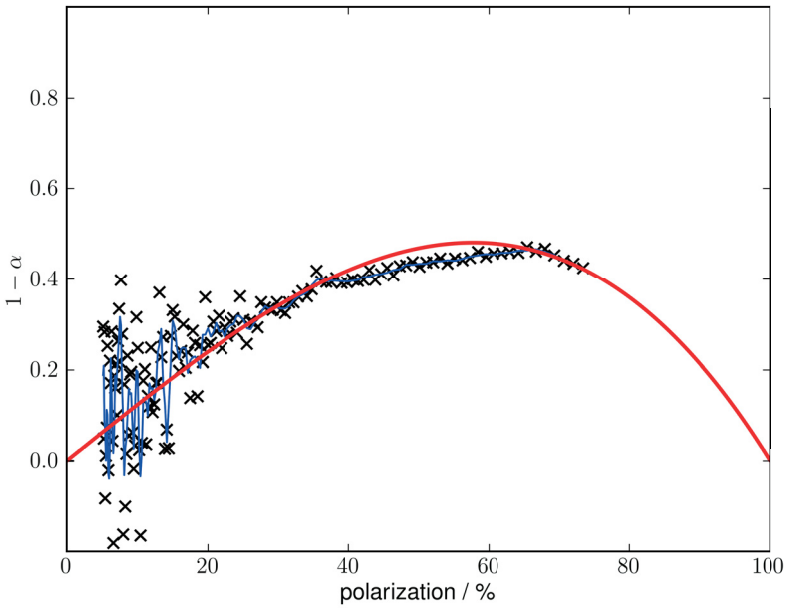

Figure 4.9.: Asymmetry index $1-\alpha$ as a function of polarization (black crosses). Solid blue line is a running average of 3 points. Solid red line shows $P(1-P^2)$ scaled with a factor of 1.25.

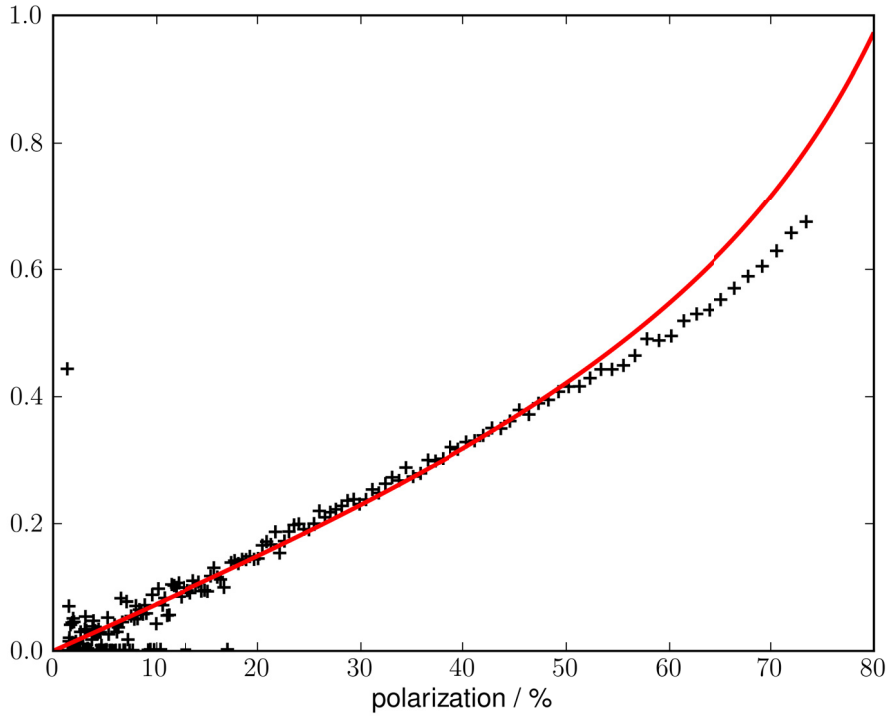

Figure 4.10.: Skewness of the experimental resonance line compared to the theoretical prediction (scaled with 0.73).

4.8. Quantitative NMR Experiments

Our NMR setup has never been used for quantitative NMR measurements. Oftentimes the amplitude information is simply discarded; because even though easily obtained, it proves also difficult to extract physical properties. Basically, what one needs is a calibration of how many nuclei at a given polarization generate which amplitude. In this section I describe three methods of how this can be done.

The NMR signal S is proportional to the number of ^{129}Xe nuclei N, the polarization P and the sine of the pulse angle θ. Since the xenon atoms always adsorb on the same surface area, it is more convenient to use the number of atomic layers N_l rather than the number of atoms.

$$\begin{aligned} S &= c \cdot N\, P \sin(\theta) \\ &= \tilde{c} \cdot N_l P \sin(\theta) \end{aligned} \tag{4.3}$$

Here c and $\tilde{c}$ are the desired proportionality constants, which depend on the spectrometer, the (pre-)amplifiers, the probe geometry and the ^{129}Xe magnetic moment.

4.8.1. Estimation from pressure in the polarization cell

The amount of ^{129}Xe for a typical experiment equals about 4 mbar pressure in the polarization cell. Assuming that all xenon forms a solid on the surface of the single crystal, we can calculate the number of monolayers this amounts to, from the surface area and the lattice constant. Under low pressure conditions, xenon forms a face centered cubic with a lattice constant of $a = 6.14\,\text{Å}$ at 30 K [Sea62]. The corresponding nearest neighbor distance is $nn = 4.34\,\text{Å}$. On Cu(100) xenon grows in (111) direction [Ber04b], therefore each atom uses $16.3\,\text{Å}^2$ of surface area. Our single crystal has a total surface area of $0.95\,\text{cm}^2$, thus one monolayer consists of 5.8×10^{14} atoms.

The volume of the polarization cell is $21\,\text{cm}^3$ [Bus11] and the crystal has a radius of 0.0055 m, see section 3.4. With the ideal gas law we can calculate the number of xenon atoms to

$$n = \frac{pV}{RT} = \frac{4\,\text{mbar} \cdot 21\,\text{cm}^3}{8.3\,\frac{\text{J}}{\text{mol K}}\,380\,\text{K}} = 2.7 \times 10^{-6}\,\text{mol} \widehat{=} 1.6 \times 10^{18} \widehat{=} 2760\,\text{ML}\,.$$

This is a rough estimation. On one side, we lose xenon gas during the transfer process and the precise loss is unknown. On the other side, there might be more xenon in the polarization cell if the quench gas pushes additional xenon from the supply pipe into the cell. The exact amount is not quantifiable, as it depends on the timing of the opening and closing of the valves.
Using the polarization measurement from section 4.5 we can calculate the proportionality constant in units of channels per nuclei, or channels per monolayer:

$$\begin{aligned} c &= \frac{1.4987 \times 10^7\,\text{ch}}{1.6 \times 10^{18} \cdot 0.77 \sin(11°)} = 7.1 \times 10^{-11}\ \text{ch/nuclei} \\ \tilde{c} &= \frac{1.4987 \times 10^7\,\text{ch}}{2760 \cdot 0.77 \sin(11°)} = 4.1 \times 10^4\ \text{ch/ML} \end{aligned} \tag{4.4}$$

This is a factor of two more than the calculations from the next sections yield. So there likely is more xenon gas in the polarization cell than expected.

4.8.2. Continuous deposition

A second possibility to calibrate the NMR signal uses the slow deposition technique, in which the hyperpolarized ^{129}Xe is not deposited onto the sample in a single burst, but over time at a fixed rate. This is achieved by keeping the xenon – after removal of the nitrogen gas – frozen in the cryo trap before the UHV, see fig. 3.9. Since at 77 K the xenon vapor pressure is higher than the pressure in the UHV, the result is a slow

desorption from the cryo trap and adsorption onto the 30 K cold single crystal. If this is done while conducting NMR experiments (90 ° single pulse), the averaged spectra show two distinct peaks: one from the xenon bulk and one from the xenon on xenon surface. By variation of the pulse repetition rate, one can determine the deposition rate from the relative peak amplitudes. Peter Gerhard did this in his PhD thesis and found a deposition rate of 4 Ml/s [Ger03].

This method has a major flaw, namely that the deposition rate is not constant over time, see fig. 4.11. However, the shape of the deposition rate is always similar and independent of the amount of xenon. Therefore the result of Peter Gerhard might be applicable, provided that the deposition time is comparable.
We have chosen a deposition time of 6 min, which is short enough to ensure that the cryo trap won't run out of xenon, while at the same time it is long enough to get a good NMR signal. To prevent depolarization through spin transfer to the copper surface a buffer layer of ^{132}Xe was used, see section 4.10.

Assuming that 1440 ML of ^{129}Xe are on the single crystal after a 6 min deposition time, one can then determine the polarization and the amplitude with a small angle NMR experiment to calculate the proportionality constant. This yields:

$$\tilde{c} = 2.0 \times 10^4 \text{ ch/ML} \tag{4.5}$$

4.8.3. Correlation of NMR and TPD signals

The methods described so far rely on assumptions about the ^{129}Xe quantity adsorbed on the sample. In this section now, I describe a way to measure this quantity.
For this the ^{129}Xe is (quickly) frozen onto the sample and a small angle NMR measurement is conducted to determine the polarization and the amplitude (as described in the previous sections). Then the NMR magnet is turned off and the sample is moved in front of the QMS.
In principal, the xenon quantity can be extracted from a TPD. However, the quantity is too large to observe the multilayer and the monolayer at the same time. Furthermore, if that much xenon desorbs too quickly, it takes time for the turbomolecular pump to remove it. We therefore use an isothermal TPD, in which the temperature is linearly increased till desorption sets in and then held there, see fig. 4.13. The time integral of the QMS-signal is then proportional to the number of ^{129}Xe monolayers. The desorption from the sample starts at about 100 sec, but as one can see in the diagram there are two peaks prior to that. Their origins are the sample holding rods where xenon also adsorbs, but which are heated faster. This off-site xenon nonetheless contributes to the NMR signal so we have to include it in the integral as well. It amounts to 10 % of the total integral.
To resolve the proportionality and quantify the number of monolayers, a calibration is

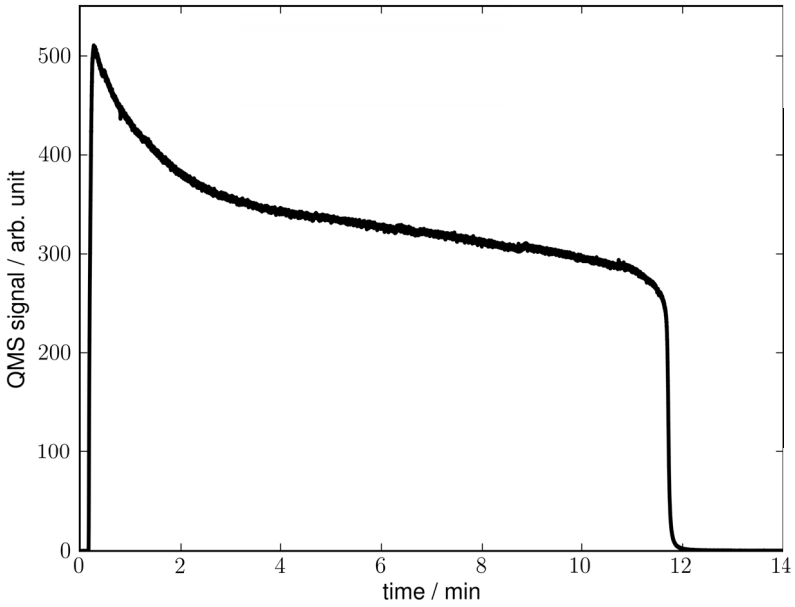

Figure 4.11.: ^{129}Xe gas flow into the UHV measured with a QMS while the setup is at room temperature. The ^{129}Xe is frozen in the cryo trap and constantly cooled with liquid nitrogen, so that the QMS measures the partial pressure after expansion into the UHV. The gas flow starts when the entry valve is opened and ends when all xenon is desorbed, which gives a remarkably sharp dropoff.

necessary. This is done with an ordinary TPD on the clean Cu(100) surface. Figure 4.12 shows three such TPDs of natural xenon. The first monolayer is clearly visible and from its area we get the calibration, which we divide by the natural abundance of ^{129}Xe – 26 %.

This measurement was repeated 3 times. The results can be found in table 4.2. The slow deposition measurement from the last section is shown as well, since its ^{129}Xe coverage was also measured with an isothermal TPD. The agreement between measured xenon quantity and assessment from the deposition rate is surprisingly good (1385 $\longleftrightarrow$ 1440 layers). The main result is the proportionality constant $\tilde{c} = 19400\,\mathrm{ch/ML}$, which is the mean of all four measurements, and the one used for further calculations.

4.9. Diluted xenon and ordering effects

Figure 4.6 suggests that the line width can get arbitrarily small if the ^{129}Xe is sufficiently diluted in ^{132}Xe. This is of course misleading, as other effects take over if the dipolar interactions become negligible.
To test whether the dipolar contribution to the line width is sufficiently small, we used

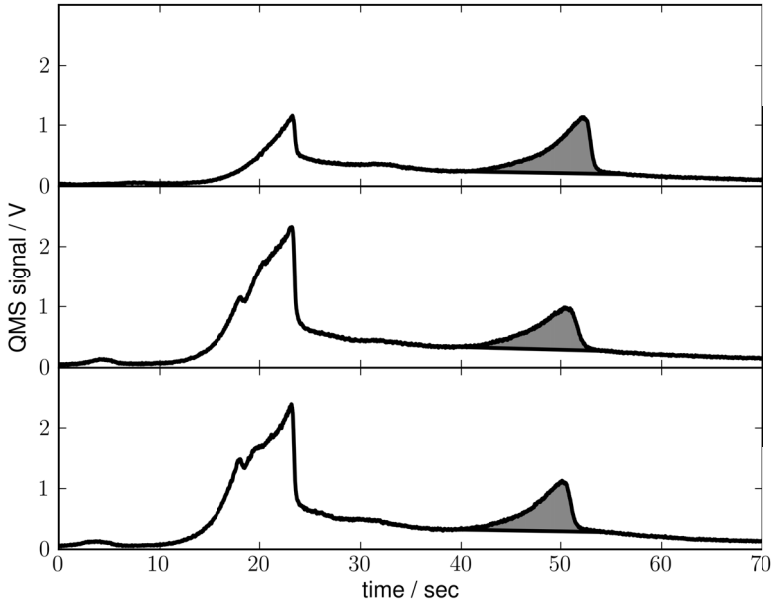

Figure 4.12.: TPD of natural ^{129}Xe. QMS signal as a function of time during a linear increase of temperature. The first monolayer is clearly visible. Its integral has been calculated with a baseline correction, shaded area. The mean of all three shaded areas is 3.77 Vs.

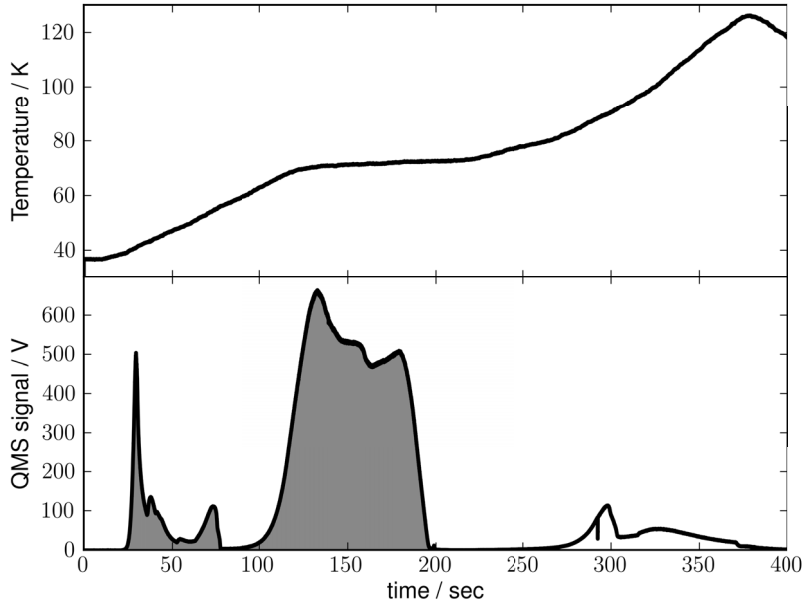

Figure 4.13.: Isothermal TPD of pure ^{129}Xe. Temperature of the single crystal and QMS signal as functions of time. The main part of the xenon gas desorbs at a constant temperature, starting at 100 sec. To get the total amount of xenon on the crystal, the integral of the shaded area is computed.

ML	polarization / %	amplitude / 10^6ch	$\tilde{c}/\frac{\text{ch}}{\text{ML}}$
3152	49.0	5.21	19049
3543	55.4	5.98	17204
2982	46.2	4.91	20126
1385	*36.1*	*1.87*	*21120*
			$\tilde{c} = 19400$

Table 4.2.: The first column is the number of xenon layers determined from the TPD. The second one shows the polarization calculated from the line shift. The third column shows the amplitude. With a flip angle of 10.2 ° the proportionality constant is calculated with eq. 4.3. The last row shows the slow deposition measurement from the last section.

the Carr-Purcell-Meiboom-Gill sequence (CPMG) [Ber04a]. This pulse sequence generates an echo train, from which the T_2 time can be estimated. As dipolar interactions cannot be inverted by a 180 ° pulse, dipolar dephased spins do not refocus (that is also the reason why it is not possible to generate an echo from a solid of pure ^{129}Xe with a simple 180 ° pulse).
Figure 4.14 shows such a CPMG measurement. After an initial 30 ° pulse at $t = 0$, the FID decays with a time constant $T_2^* = 1.57$ ms; the corresponding line width is 200 Hz. This is the line width limit we can achieve. After a delay of $\tau = 7$ ms, a 180 ° pulse is applied that causes the spins to refocus at $t = 14$ ms. Because the 180 ° pulse is not perfect, it generates an FID as well. The trick now is that the next inversion pulse is applied after a delay of $2\tau = 14$ ms – this causes the echoes of the unintended FIDs to occur at the same time as the 180 ° pulses. From the echoes one gets an estimation of $T_2 = 11$ ms, which corresponds to a line width of 30 Hz.
Part of the T_2 – T_2^* difference is the inhomogeneity of the static magnetic field, but with a good shimming these inhomogeneities are negligible. We tested this with a small cylindrical NaCl(aq) sample (size: 10 mm high, 2 mm wide), where we reached a line width of 19 Hz. Unfortunately, the measurement I describe in the following suffered from a defect in the shim controls and the resonance line is therefore unnecessarily broad.

Thus remains the fundamental question whether it is possible to observe the annealing effect(s) with our experimental setup. To test this, we conducted the following experiment. A strongly diluted ^{129}Xe/^{132}Xe mixture was frozen onto the single crystal at a temperature between 25 K and 30 K. Then we recorded five small angle measurements, where we expected such a solid to have abundant crystallographic defects. Next, the sample was annealed for 3 min at either 41 K, 47 K or 53 K, and afterwards cooled down and measured again. This cycle was repeated multiple times. The temperature at which the measurements were performed was between 25 K and 27 K. Figure 4.15 shows the temperature cycle and fig. 4.16 shows the line width as a function of the annealing cycle. The light colored symbols show the individual measurements, and the dark colored crosses the mean of five measurements.

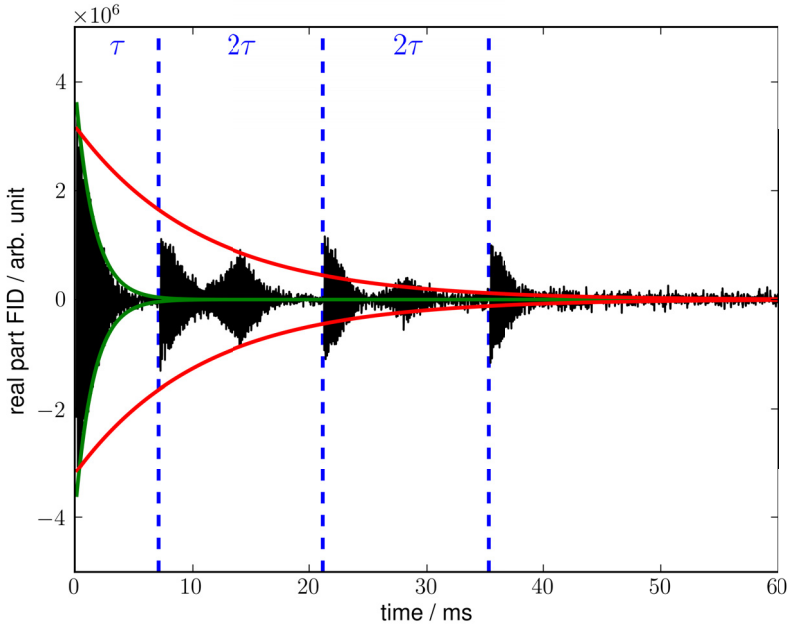

Figure 4.14.: Measurement of a ^{129}Xe/^{132}Xe mixture with the CPMG sequence. At $t = 0$, a 30 ° pulse is deployed, and the green solid line is a fit to its FID. Afterwards three 180 ° pulses are used to refocus the spins (dashed vertical lines). The echoes appear at 14 ms, 28 ms and 42 ms. The red solid line is an estimation of their decay.

The line width follows an exponential decay ($f(x) = a\,\mathrm{e}^{-x/b} + c$, solid lines), and we get the following parameters from the fit:

temperature	a/Hz	b	c/Hz
41K (blue)	18.7	3.07	297
47K (green)	26.6	1.21	294
53K (red)	39.0	0.98	287

As hoped for, we clearly see the effect of the annealing on the line width. We find that the higher the annealing temperature, the smaller is the line width one can achieve. This makes sense, considering that a higher temperature can mobilize more kinds of defects. At the same time, a higher annealing temperature leads to a faster approach to the final line width, which is understandable if the mobility of the defects is proportional to the temperature.

Likely, the annealing effect on the line width is systematically underestimated in the analysis above, because of the aforementioned line width contribution from a bad shimming. With a propper shimming, a line width reduction of up to 100 Hz is possible, which would accentuate the annealing effect.

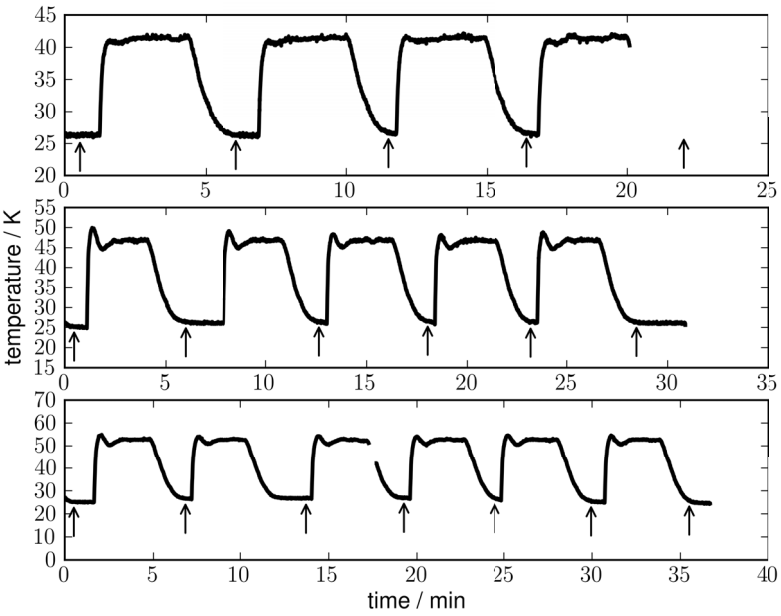

Figure 4.15.: Temperature during annealing cycles. Arrows mark the time of NMR measurements. The first curve belongs to the 41 K cycle (blue symbols in fig. 4.16). The second belongs to the 47 K cycle (green) and the third to the 53 K cycle (red). Missing data points in the first and third diagram are the result of an ADC misconfiguration.

4.10. Spin diffusion and T_1-measurements

The high differences in T_1 measurements obtained with our setup were often attributed to oxygen contamination [Sta01, Ger03, Koc06a]. But already Dirk Stahl stated that additionally, spin diffusion to the substrate could play a role [Sta01]. In this section I am going to show that spin diffusion indeed can explain the wide range of T_1 times.

The basic T_1 experiment that is utilized throughout this section consists of at least two series of small angle measurements. In the first series the pulses come in a rapid succession to minimize the depolarization during the experiment. From this series the pulse angle is calculated as described in section 4.5. All further measurements follow essentially the same pattern, but a delay is introduced between consecutive pulses. The depolarization, which is caused by the NMR pulses, is taken into account with the help of the first experiment; so only the depolarization that originates from relaxation effects remains. The decay time can then be extracted.

In a first step I will look into the case of a xenon solid with no spin diffusion. This is, once again, achieved by diluting the ^{129}Xe in ^{132}Xe. Figure 4.17 shows such a T_1 measurement with strongly diluted ^{129}Xe ($c \approx 5\,\%$). While the black curve shows a sample that was simply frozen onto the single crystal, the red curve shows a sample that was annealed at 49 K for 5 min. The extracted times are $T_1 = 280$ min (black curve) and

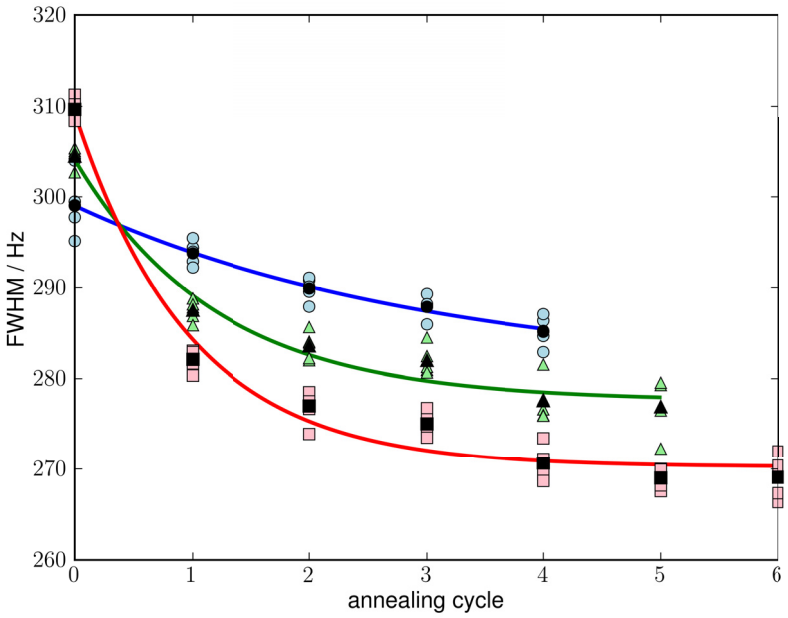

Figure 4.16.: Annealing of ^{129}Xe/^{132}Xe mixtures. For three different annealing temperatures, after every annealing cycle five NMR measurements were conducted (light symbols). Dark crosses mark the mean of five such measurements, and the solid lines show exponential fits thereof.

$T_1 = 250\,\text{min}$ (red curve). It is uncertain whether the time difference is caused by the annealing or by a small variation in the mixing ratio. Nonetheless, the result is clear: the depolarization time for this sample amounts to a couple of hours.

To investigate the spin diffusion we come back to experiments with pure ^{129}Xe. In order to verify that we actually see spin diffusion we use the following experiment: First a buffer layer of ^{132}Xe is put onto the clean Cu(100) surface, after which a certain amount of pure hyperpolarized ^{129}Xe is added on top. The T_1 time of this setup is compared to a measurement with a similar amount of ^{129}Xe, but without a buffer layer. Figure 4.18 shows the results for three different ^{129}Xe quantities. Clearly the buffer layer prolongs the T_1 time. And we already see that a smaller ^{129}Xe quantity causes a faster decay of polarization. This effect is strong if no buffer layer is used, and less so for the experiments with a buffer layer.
Additional evidence for spin diffusion can be found in the shape of the decay curves. If a buffer layer is used, it is simply exponential, whereas on bare Cu(100) the decay is faster than exponential for small times (most prominent in the blue and black curves in fig. 4.18) and approximates an exponential for long times.
The range of relaxation times is fairly wide, from 20 min to 3 hours.

The T_1 dependence on the ^{129}Xe layer thickness on top of a buffer layer is not yet understood. The attempt to put a second buffer layer onto the ^{129}Xe sample to form a

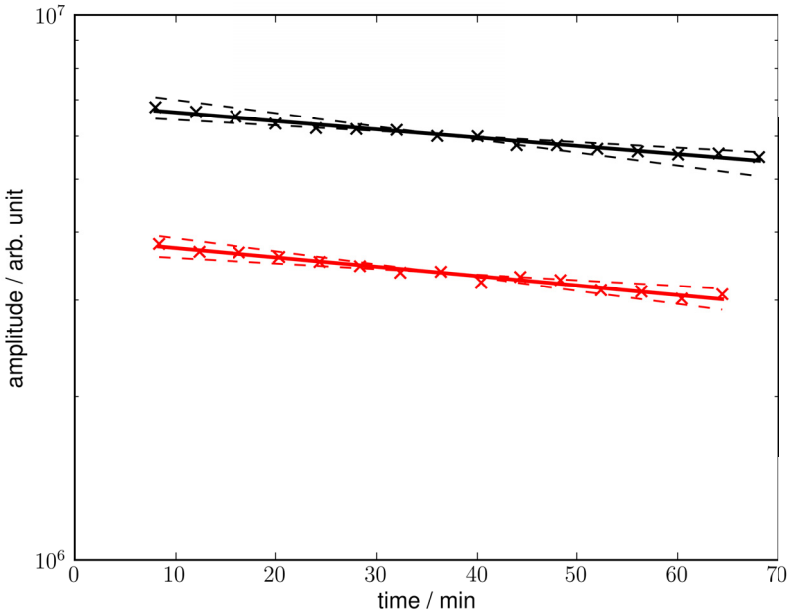

Figure 4.17.: T_1 measurement for strongly diluted ^{129}Xe ($c \approx 5\,\%$). Both measurements share approximately the same mixing ratio, but the red measurement was annealed for 5 min at 49 K. Both show an exponential decay in this semi-logarithmic plot. The effect of the pulse angle is already corrected for. The dashed lines are error estimates and correspond to a decay time of 3 hours and 7 hours respectively.

sandwich structure and prohibit depolarization at the interface was inconclusive.
The factor of 3 between measurements with and without buffer indicates that the xenon surface acts also depolarizing, as a factor of 4 would be the expected value for an ideal polarization drain.

To quantify the diffusion constant we use the model from chapter 2.8. As xenon inter layer distance we use 3.54 Å, calculated from a nearest neighbor distance of 4.34 Å [Sea62]. Therefore the xenon solid has a height of 3.54×10^{-10} m/layer, which for 3000 layers yields approximately 1 μm.
In order to calculate the diffusion constant, it is necessary to determine the polarization and the number of xenon layers. To achieve this, we use the first spectrum of each series and compare the resonance frequency to the frequency limit of 0% polarization, and calculate the polarization from the shift. The number of xenon layers is calculated from the amplitude of the first spectrum and $\tilde{c}$ from tab. 4.2.
Figure 4.19 shows the result. The non-exponential decay for small times is reproduced quite well. The diffusion constant has the right order of magnitude, but depending on the xenon quantity it varys from $1.1 \times 10^{17}\,\mathrm{m}^2/\mathrm{s}$ to $9.5 \times 10^{17}\,\mathrm{m}^2/\mathrm{s}$. Likely, the polarization and thickness determination from a single spectrum is unreliable.

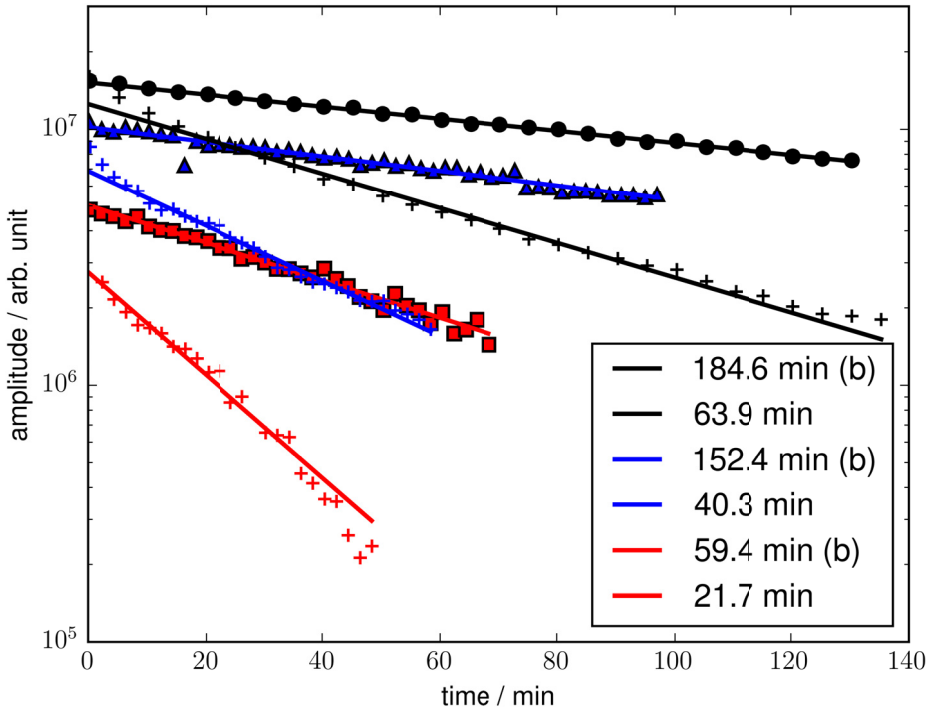

Figure 4.18.: T_1 measurements with/without a ^{132}Xe buffer layer. For each of three different ^{129}Xe quantities (black, red and blue) one measurement with buffer layer (filled symbols) and one on bare Cu(100) (+ symbols) is shown. The exponential decay was fitted with a simple exponential and the decay time extracted, see legend. The higher decay times correspond to the buffer layer measurements.

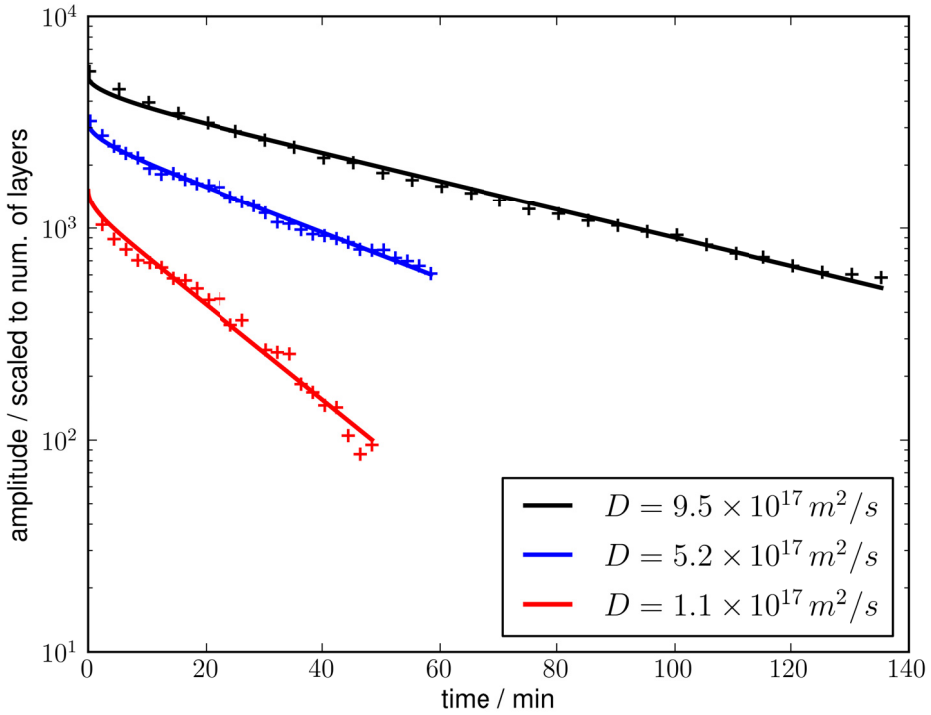

Figure 4.19.: Determination of the diffusion constant. Measurement data scaled to the number of layers. Solid lines show the diffusion model from chapter 2.8.

5. Conclusion

In this thesis I have shown that it is legitimate to assume that almost all xenon gas freezes onto the front side of the single crystal. With a simple gradient coil, it is possible to spectroscopically separate front and back side, leading to the result that under standard conditions about 5 % of the xenon gas ends up on the back side.
To improve the trouble shooting procedures, ^{11}B NMR may be employed as a tool to verify the correct functioning of the apparatus NMR part. In the transfer process a point of weak magnetic field has been identified that was responsible for the major polarization loss of the ^{129}Xe. With an air core coil it is now possible to overcome this effect, which means that the polarization was increased from an unreliable 5–80 % to a reliable 50–80 %. Additionally, after the O-ring deterioration problem was solved the new polarization apparatus is now fully functional. By using EPDM O-rings, the replacement cycle could be extended from a weekly to almost a yearly basis.

In the theory chapter the quantum mechanical calculations of the central moments of the resonance line have been presented, including their dependencies on the ^{129}Xe concentration and polarization. However, the fit of the resonance line with a predefined function is still not satisfactory. Extraction of the moments from such a fit is not possible, yet.
The comparison of the line width with the theory is excellent and the expected behavior is fully reproduced. While there are indications that the asymmetry of the resonance line follows the third central moment, it was not possible to prove this point.

The annealing of solidified xenon can be monitored by NMR if the ^{129}Xe is sufficiently diluted in ^{132}Xe. The annealing affects the line width in expected ways. At this point, however, we still lack a connection to physical properties, like for example the mobility of certain kinds of defects as a function of temperature.

By linking the NMR signal to an isothermal TPD it is feasible to quantify the number of ^{129}Xe monolayers on the single crystal from the NMR amplitude. This allows for conceptually new experiments with this setup.

The described model for spin diffusion proved to be quite successful. The combination of surface science and NMR reduces the number of assumptions and simplifies the diffusion measurements. Meanwhile, a precision measurement of the diffusion constant is still pending.

6. Outlook

A dissertation gets finished, but its subject seldom is. There are many experiments that I wished I had time to conduct. Some are listed below:

The amplitude decay in small angle measurements is not purely exponential; one probable cause could be a dependency of the pulse angle on the polarization [Wal04]. If this really is the case, it should be possible to investigate the connection by variation of the pulse angle.

The central moments of the resonance line, which I calculated, still contain the geometry factors. By evaluating them, it would be possible to understand the angular dependency of the central moments on the resonance line and conduct angle resolved line shape experiments. Many experiments in this respect would profit from a reliable line fit – preferable with a physical justification of the parameters.

To further investigate the annealing, it might be possible to constantly monitor the line width during the annealing process, similar to the T_1 measurements. The defects could thus be observed in their diffusion out of the solid.

The spin diffusion measurements that I began leave quite some room for improvement. The (reliable) determination of the polarization from a single spectrum would enable the possibility to determine the xenon quantity without losing much polarization and time. The skewness of the resonance line could do the trick. This would greatly improve the diffusion measurements and open up the possibility of a precision measurement of the diffusion constant.
Finally, the anisotropy of the spin diffusion is a challenging, but interesting topic.

Appendices

A. Fitting the resonance line

As described earlier, it is difficult to fit the NMR lines in the high polarization regime due to their asymmetry. Matthias Buschmann and Peter Gerhard tried to overcome this problem with a two line fit [Bus11, Ger03]. By using the sum of two functions, the deviation from the measurement is of course reduced, but the fit parameters are not independent and thus unstable. In addition, it is impossible to calculate the moments with this approach (if one function is a Lorentzian).

In this section I describe a fitting procedure that uses a product of two Lorentzians. After some trial and error I came up with the following function:

$$f(\nu) = A\,\frac{d^2b^2}{\left((\nu-\nu_0-\frac{a}{2})^2+b^2\right)\cdot\left((\nu-\nu_0+\frac{a}{2})^2+d^2\right)} \tag{A.1}$$

A is the amplitude and b, d are a combination of widths and weights. The centers are chosen as $\nu_0 \pm a/2$; where ν_0 is the frequency for 0 % polarization, which is independently determined. a, b, and d are bound to be non-negative. There are thus four free parameters.
This fit method needs a careful phase correction. Regrettably, it is not possible to avoid this phase correction by using the power spectrum, because every moment of the power spectrum depends on all moments of the absorption spectrum [Hem96].

The function in eq. A.1 has the following central moments:

$$\begin{aligned}
\langle\nu\rangle &= \nu_0 - \frac{a(d-b)}{2(d+b)} \\
\langle\nu^2\rangle &= bd + bd\frac{a^2}{(d+b)^2} \\
\langle\nu^3\rangle &= abd\,\frac{(d-b)((d+b)^2+a^2)}{(d+b)^3}
\end{aligned} \tag{A.2}$$

Note that the expression for $\langle\nu^3\rangle$ is the principal value.

Except for its broad base the experimental line shape is reproduced quite well, see fig. A.1. Comparing the two spectra, a simultaneous decrease of the asymmetry and the a parameter is evident.

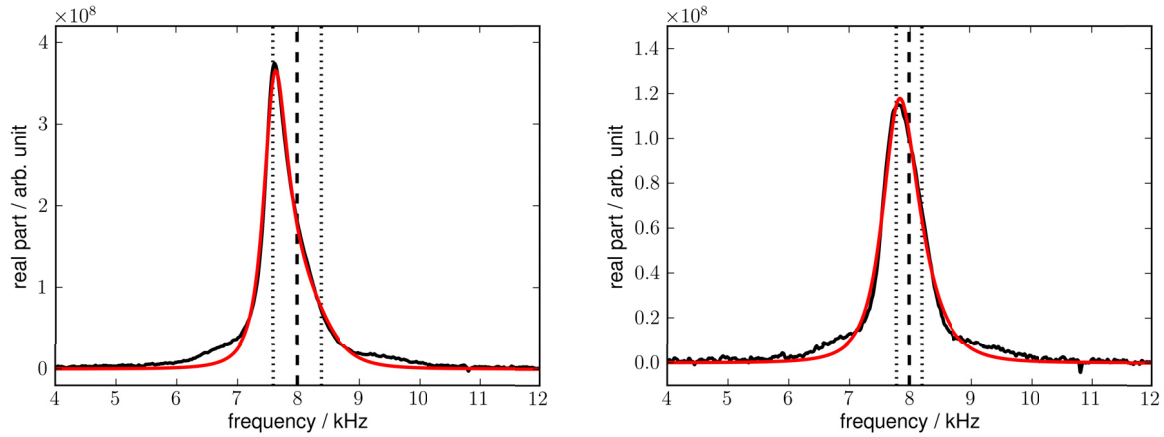

Figure A.1.: Real part of a NMR spectrum of pure ^{129}Xe recorded with a small angle pulse (black curve). Fit to the data with the product of two Lorentzians – eq. A.1 (red curve). The dashed line indicates ν_0 and the dotted lines $\nu_0 \pm a/2$. *Left side:* First spectrum of the series, 74 % polarization, *right side:* 40th spectrum, 34 % polarization.

The same small angle series as in chapter 4.6 and 4.7 is used to determine the polarization dependency of the moments, see fig. A.2. For all three central moments as well as the skewness, the theoretical values were each scaled with a constant factor.
While the first moment and the skewness follow the theoretical prediction remarkably well, the second and third central moment are unstable below 25 % polarization. This behavior has its origin in the d parameter. Apparently this is compensated in the skewness.

All central moments, and the skewness, show deviations from the theoretical prediction at high polarizations, see discussion in chapter 4.7

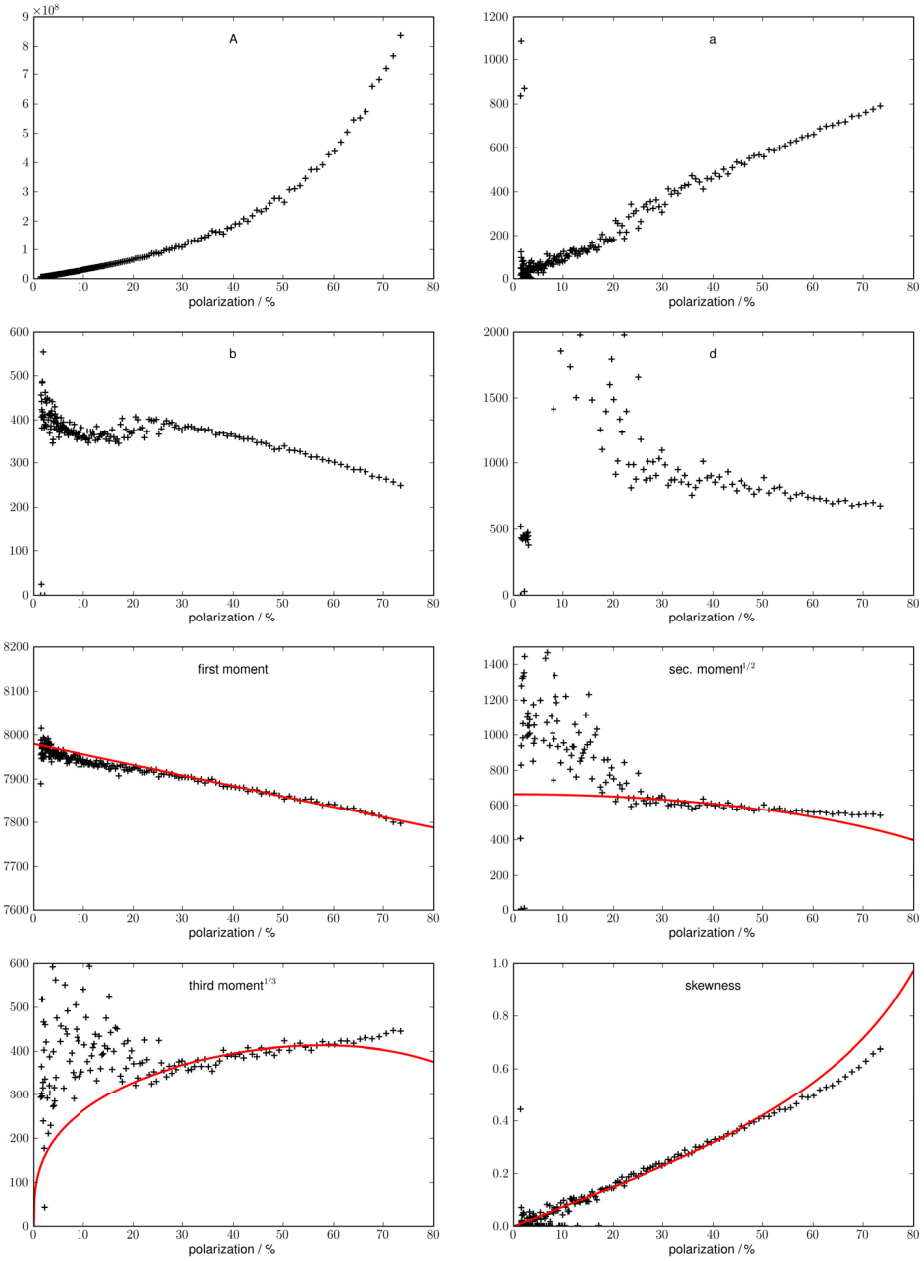

Figure A.2.: Fit parameters and moments. The upper four graphs show the fit parameters as functions of the polarization. They seem to be stable in between 30 % and 74 % polarization. The lower four show the central moments and the skewness. *Red lines* indicate the theoretical course.

B. Line shape dependency on ^{129}Xe polarization and concentration

The calculations in this chapter mainly follow the paper of Tsyplyatyev and Whittaker [Tsy12], extended with the dependency on the ^{129}Xe concentration – see also chapter 2.5. We start with the secular dipolar Hamiltonian in the following form:

$$H = \mu B \sum_j I_j^z + \sum_{i \neq j} F_{ij} \left(I_j^z I_i^z - \frac{I_j^+ I_i^-}{2} \right) \tag{B.1}$$

In the rest of this chapter the position/angle dependent part is abbreviated with $F_{ij} = \frac{\xi(3\cos^2(\theta_{ij})-1)}{r_{ij}^3}$. r_{ij} is the distance between spin i and j and θ_{ij} the angle between r_{ij} and the static field B, ξ is the dipole interaction strength. The important property of F_{ij} is its symmetry $F_{ij} = F_{ji}$.

Van Vleck wrote in 1948 [VV48] that it is not possible to directly access the line shape, but he described how the moments of the resonance line may be used to gain information on its shape. To calculate the moments of the resonance line quantum mechanically, one needs a variety of commutators. On the most fundamental level these are:

$$\begin{aligned}
[I^x, I^y] &= iI^z \qquad [I^y, I^z] = iI^x \qquad [I^z, I^x] = iI^y \\
\left[I^+, I^-\right] &= 2I^z \\
\left[I^\pm, I^x\right] &= \pm I^z \\
\left[I^\pm, I^y\right] &= iI^z \\
\left[I^\pm, I^z\right] &= \mp I^\pm
\end{aligned} \tag{B.2}$$

Operators without index are abbreviations for a summation over all nuclei, e.g. $I^\pm = \sum_j I_j^\pm$, where $I^\pm = I^x \pm I^y$ are the ladder operators.
The FID is the expectation value of I^+. From there, one can derive the moments by calculating the traces of the Hamiltonian [Abr73, Tsy12]:

$$\begin{aligned}
\langle m\rangle &= -\frac{\mathrm{Tr}\left([H_0, I^-]I^+\right)}{\mathrm{Tr}\left(I^-I^+\right)} \\
\langle m^2\rangle &= -\frac{\mathrm{Tr}\left([H_0, I^-][H_0, I^+]\right)}{\mathrm{Tr}\left(I^-I^+\right)} \\
\langle m^3\rangle &= \frac{\mathrm{Tr}\left([H_0, [H_0, I^-]][H_0, I^+]\right)}{\mathrm{Tr}\left(I^-I^+\right)}
\end{aligned} \tag{B.3}$$

As in the Tsyplyatyev and Whittaker paper we first calculate the denominator. The result has to be independent of the basis used for calculation, so a basis of non-interacting states is favorable. But we are not in a complete Hilbert space, so we cannot cyclically permute the operators in the trace.
In the following N is the total number of nuclei, $\tilde{N}$ the number of spin carrying ^{129}Xe nuclei and n the number of ^{129}Xe nuclei that are in the spin up state. Thus the number of nuclei in the spin down state is $\tilde{N} - n$, and the number of spin-less nuclei is $N - \tilde{N}$.

$$\begin{aligned}
\mathrm{Tr}\left(I^-I^+\right) &= \sum_f \sum_{jk} \langle f|I_k^- I_j^+|f\rangle \\
&= \sum_f \sum_{j} \langle f|I_j^- I_j^+|f\rangle \\
&= \sum_j \sum_f \delta_{j\downarrow} \\
&= \sum_j \binom{N-1}{\tilde{N}-1}\binom{\tilde{N}-1}{n} \\
&= N\binom{N-1}{\tilde{N}-1}\binom{\tilde{N}-1}{n} \\
&= (\tilde{N}-n)\binom{N}{\tilde{N}}\binom{\tilde{N}}{n} \\
&= \frac{N!}{(N-\tilde{N})!\,n!\,(\tilde{N}-n-1)!}
\end{aligned} \tag{B.4}$$

The first step is possible because $\langle f|I_j^+|f\rangle = 0$, so only the cases $j = k$ are non-zero. $\delta_{j\downarrow}|f\rangle$ is a short notation that yields 1 if the j-th spin is in the down state and 0 if not. I have omitted the ket-vector in the following as to clarify the combinatorial argument. The sum $\sum_f$ over all basis states results in the number of basis states, which yields the number of possibilities to distribute n spin up states onto $\tilde{N}$ ^{129}Xe nuclei distributed onto N positions. As the spins are indistinguishable we get the product of two binomial coefficients.

B.1. The first moment $\langle \mathbf{m} \rangle$

To calculate the commutator of the Hamiltonian with I^-, three other commutators $[I_j^z, I^-]$, $[I_j^z I_i^z, I^-]$ and $[I_j^+ I_i^-, I^-]$ are needed. Because the indices i and j originate from the sum in the Hamiltonian we assume $i \neq j$.

$$[I_j^z, I^-] = \sum_i [I_j^z, I_i^-] = -I_j^- \tag{B.5}$$

$$\begin{aligned}
[I_j^z I_i^z, I^-] &= \sum_k [I_j^z I_i^z, I_k^-] \\
&= [I_j^z I_i^z, I_j^-] + [I_j^z I_i^z, I_i^-] \\
&\overset{i\neq j}{=} [I_j^z, I_j^-] I_i^z + I_j^z [I_i^z, I_i^-] \\
&= -I_j^- I_i^z - I_j^z I_i^-
\end{aligned} \tag{B.6}$$

$$\begin{aligned}
[I_j^+ I_i^-, I^-] &= \sum_k [I_j^+ I_i^-, I_k^-] \\
&= [I_j^+ I_i^-, I_j^-] + [I_j^+ I_i^-, I_i^-] \\
&\overset{i\neq j}{=} [I_j^+, I_j^-] I_i^- + I_j^+ [I_i^-, I_i^-] \\
&= 2 I_j^z I_i^-
\end{aligned} \tag{B.7}$$

So for the first moment the trace of $I_j^z I_i^- I_k^+$ is required. However only the terms with $k = i$ contribute, since all other terms contain an unpaired raising or lowering operator.

$$\begin{aligned}
\mathrm{Tr}\left(I_j^z I_i^- I^+\right) = \mathrm{Tr}\left(I_i^z I_j^- I^+\right) &= \sum_f \langle f | I_j^z I_i^- I_i^+ | f \rangle \\
&= \frac{1}{2} \sum_f \delta_{i\downarrow} (\delta_{j\uparrow} - \delta_{j\downarrow}) \\
&= \frac{1}{2} \binom{N-2}{\tilde{N}-2} \left(\binom{\tilde{N}-2}{n-1} - \binom{\tilde{N}-2}{n} \right) \\
&= -\frac{1}{2} \frac{(N-2)!(\tilde{N}-2n-1)}{n!(N-\tilde{N})!(\tilde{N}-n-1)!}
\end{aligned} \tag{B.8}$$

$\sum_f \delta_{j\uparrow} \delta_{i\downarrow}$ yields the number of basis states required for a spin system where the i-th spin is in the down and the j-th spin is in the up state. Two spins are thus held fixed

which means we can distribute $\tilde{N}-2$ spins among $N-2$ free positions. Furthermore, one spin j is fixed in the up state, so there are $n-1$ nuclei with spin up left, which we can distribute among the $\tilde{N}-2$ positions. Combining eq. B.8 with eq. B.4 we get the normalized trace.

$$\frac{\mathrm{Tr}\left(I_j^z I_i^- I^+\right)}{\mathrm{Tr}\left(I^- I^+\right)} = -\frac{1}{2}\frac{\tilde{N}-2n-1}{N(N-1)} \tag{B.9}$$

Finally the first moment or alternatively the first central moment $\langle\nu\rangle$ can be calculated.

$$\begin{aligned}
\langle m\rangle = \langle\nu\rangle &= -\frac{\mathrm{Tr}\left([H_0, I^-]I^+\right)}{\mathrm{Tr}\left(I^- I^+\right)} \\
&= -\mathrm{Tr}\left(\mu B\sum_j [I_j^z, I^-]I^+ + \sum_{i\neq j} F_{ij}\left([I_j^z I_i^z, I^-]I^+ - \frac{[I_j^+ I_i^-, I^-]I^+}{2}\right)\right) \Big/ \mathrm{Tr}\left(I^- I^+\right) \\
&= \left(\mu B\mathrm{Tr}\left(I^- I^+\right) + \sum_{i\neq j} F_{ij}\Big(\mathrm{Tr}\left(I_j^- I_i^z I^+\right) + 3\,\mathrm{Tr}\left(I_j^z I_i^- I^+\right)\Big)\right) \Big/ \mathrm{Tr}\left(I^- I^+\right) \\
&= \mu B + 3\sum_{i\neq j} F_{ij}\frac{\mathrm{Tr}\left(I_j^z I_i^- I^+\right)}{\mathrm{Tr}\left(I^- I^+\right)} \\
&= \mu B - \frac{3}{2}\sum_{i\neq j} F_{ij}\frac{\tilde{N}-2n-1}{N(N-1)} \\
&= \mu B - \frac{3}{2}\sum_{j} F_{0j}\frac{\tilde{N}(1-2\frac{n}{\tilde{N}}-\frac{1}{\tilde{N}})}{N(1-\frac{1}{N})} \\
&= \mu B - \frac{3}{2}cP\sum_j F_{0j} \qquad \text{for } N, \tilde{N}\to\infty
\end{aligned} \tag{B.10}$$

Under the sum $\mathrm{Tr}\left(I_j^- I_i^z I^+\right)$ and $\mathrm{Tr}\left(I_j^z I_i^- I^+\right)$ are equal. The operators I_j^z and I_i^- commute since $i\neq j$, and we can rename $i\leftrightarrow j$ in the second summand because $F_{ij}=F_{ji}$. So the first moment or, equally, the resonance frequency is a constant minus the concentration $c=\tilde{N}/N$ of ^{129}Xe in all nuclei times the polarization $P=1-2n/\tilde{N}$.
To perform the summation over i we assume all nuclei to have similar surroundings. In eq. B.10 we already calculated $[H_0, I^-]$. For future reference I'll state the result separately:

$$[H_0, I^-] = -\mu B I^- - 3\sum_{i\neq j} F_{ij} I_j^- I_i^z \tag{B.11}$$

B.2. The second moment $\langle \mathbf{m^2} \rangle$

For the calculation of the second moment (see eq. B.3) the commutator of H_0 with I^+ is needed. A pre-calculation of three smaller commutators is advisable. Along the line of eq. B.5, eq. B.6 and eq. B.7 we can derive:

$$[I_j^z, I^+] = I_j^+ \tag{B.12}$$

$$\begin{aligned}[I_j^z I_i^z, I^+] &\overset{i\neq j}{=} [I_j^z, I_j^+] I_i^z + I_j^z [I_i^z, I_i^+] \\ &= I_j^+ I_i^z + I_j^z I_i^+ \end{aligned} \tag{B.13}$$

$$\begin{aligned}[I_j^+ I_i^-, I^+] &\overset{i\neq j}{=} [I_j^+, I_j^+] I_i^- + I_j^+ [I_i^-, I_i^+] \\ &= -2 I_i^z I_j^+ \end{aligned} \tag{B.14}$$

Most traces have already been calculated for the first moment. In addition a four operator trace is now required. The indices are restricted by $i \neq j$ and $k \neq l$. All parts except $i = l$ are again zero, because they contain an unpaired raising/lowering operator. We need to treat two cases separately, namely $j = k$ and $j \neq k$.

$$\begin{aligned}&\mathrm{Tr}\left(I_j^z I_k^z I_i^- I_i^+\right) \\ &= \frac{1}{4}\sum_f \delta_{i\downarrow}\Big[(1-\delta_{jk})(1-\delta_{ik})(\delta_{j\uparrow}-\delta_{j\downarrow})(\delta_{k\uparrow}-\delta_{k\downarrow}) - \delta_{ik}(\delta_{j\uparrow}-\delta_{j\downarrow}) + \delta_{jk}(\delta_{k\uparrow}+\delta_{k\downarrow})\Big] \\ &= \frac{1}{4}(1-\delta_{jk})(1-\delta_{ik})\binom{N-3}{\tilde{N}-3}\left(\binom{\tilde{N}-3}{n-2} + \binom{\tilde{N}-3}{n} - 2\binom{\tilde{N}-3}{n-1}\right) \\ &\quad + \frac{1}{4}\delta_{jk}\binom{N-2}{\tilde{N}-2}\left(\binom{\tilde{N}-2}{n-1} + \binom{\tilde{N}-2}{n}\right) - \frac{1}{4}\delta_{ik}\binom{N-2}{\tilde{N}-2}\left(\binom{\tilde{N}-2}{n-1} - \binom{\tilde{N}-2}{n}\right) \\ &= \frac{1}{4}(1-\delta_{jk})(1-\delta_{ik})(N-3)!\frac{(\tilde{N}-2n-1)(\tilde{N}-2n-2)-2n}{(N-\tilde{N})!n!(\tilde{N}-n-1)!} \\ &\quad + \frac{1}{4}\delta_{jk}\frac{(N-2)!(\tilde{N}-1)}{(N-\tilde{N})!n!(\tilde{N}-n-1)!} + \frac{1}{4}\delta_{ik}\frac{(N-2)!(\tilde{N}-2n-1)}{(N-\tilde{N})!n!(\tilde{N}-n-1)!}\end{aligned} \tag{B.15}$$

Combining eq. B.15 with eq. B.10 we get the normalized four operator trace. In the case of a slightly different trace, namely $I_i^+ \to I_l^+$, an additional δ_{il} enters the result which makes the $(1-\delta_{ik})$ factor obsolete and cancels the third term out.

$$\begin{aligned}\frac{\mathrm{Tr}\left(I_j^z I_k^z I_i^- I_i^+\right)}{\mathrm{Tr}\left(I^- I^+\right)} &= \frac{1}{4}\Bigg[(1-\delta_{jk})(1-\delta_{ik})\frac{(\tilde{N}-2n-1)(\tilde{N}-2n-2)-2n}{N(N-1)(N-2)} \\ &\qquad + \delta_{jk}\frac{\tilde{N}-1}{N(N-1)} + \delta_{ik}\frac{\tilde{N}-2n-1}{N(N-1)}\Bigg] \\ \frac{\mathrm{Tr}\left(I_j^z I_k^z I_i^- I_l^+\right)}{\mathrm{Tr}\left(I^- I^+\right)} &= \frac{1}{4}\delta_{il}\left[(1-\delta_{jk})\frac{(\tilde{N}-2n-1)(\tilde{N}-2n-2)-2n}{N(N-1)(N-2)} + \delta_{jk}\frac{\tilde{N}-1}{N(N-1)}\right]\end{aligned} \tag{B.16}$$

This result deviates from the intermediate result (eq. 10) in the paper [Tsy12] for reasons unknown. Similar to eq. B.11 we calculate the commutator of H_0 and I^+.

$$[H_0, I^+] = \mu B I^+ + 3\sum_{i\neq j} F_{ij} I_j^+ I_i^z \tag{B.17}$$

These are all the preliminary results one needs to calculate the second moment.

$$\begin{aligned}\langle m^2\rangle &= -\frac{\mathrm{Tr}\left([H_0, I^-][H_0, I^+]\right)}{\mathrm{Tr}\left(I^- I^+\right)} \\ &= \frac{-\mathrm{Tr}\left(\left[-\mu B I^- - 3\sum\limits_{i\neq j} F_{ij} I_j^- I_i^z\right]\left[\mu B I^+ + 3\sum\limits_{k\neq l} F_{kl} I_l^+ I_k^z\right]\right)}{\mathrm{Tr}\left(I^- I^+\right)} \\ &= (\mu B)^2 + 6\mu B\sum_{i\neq j} F_{ij}\frac{\mathrm{Tr}\left(I_j^- I_i^z I_j^+\right)}{\mathrm{Tr}\left(I^- I^+\right)} + 9\sum_{i\neq j}\sum_{k\neq l} F_{ij}F_{kl}\frac{\mathrm{Tr}\left(I_j^z I_i^- I_k^z I_l^+\right)}{\mathrm{Tr}\left(I^- I^+\right)} \\ &= (\mu B)^2 - 3\mu B\sum_{i\neq j} F_{ij}\frac{\tilde{N}-2n-1}{N(N-1)} \\ &\quad + \frac{9}{4}\sum_{\substack{i\neq j\\ k\neq l}} F_{ij}F_{kl}\delta_{il}\left[(1-\delta_{jk})\frac{(\tilde{N}-2n-1)(\tilde{N}-2n-2)-2n}{N(N-1)(N-2)} + \delta_{jk}\frac{\tilde{N}-1}{N(N-1)}\right] \\ &= (\mu B)^2 - 3\mu B\sum_{j} F_{0j}\frac{\tilde{N}-2n-1}{N-1} \\ &\quad + \frac{9}{4}\sum_{j\neq k} F_{0j}F_{k0}\frac{(\tilde{N}-2n-1)(\tilde{N}-2n-2)-2n}{(N-1)(N-2)} + \frac{9}{4}\sum_j F_{0j}^2\frac{\tilde{N}-1}{N-1}\end{aligned} \tag{B.18}$$

With the second moment we next calculate the second central moment.

$$
\begin{aligned}
\langle \nu^2 \rangle &= \left\langle \Big(m - \langle m \rangle \Big)^2 \right\rangle = \langle m^2 \rangle - \langle m \rangle^2 \\
&= (\mu B)^2 - 3\mu B \sum_j F_{0j} \frac{\tilde{N} - 2n - 1}{N - 1} + \frac{9}{4} \sum_{i \neq j} F_{0i} F_{j0} \frac{(\tilde{N} - 2n - 1)(\tilde{N} - 2n - 2) - 2n}{(N-1)(N-2)} \\
&\quad + \frac{9}{4} \sum_j F_{0j}^2 \frac{\tilde{N} - 1}{N - 1} - \left[\mu B - \frac{3}{2} \sum_j F_{0j} \frac{\tilde{N} - 2n - 1}{N - 1} \right]^2 \\
&= \frac{9}{4} \sum_{i \neq j} F_{0i} F_{j0} \frac{(\tilde{N} - 2n - 1)(\tilde{N} - 2n - 2) - 2n}{(N-1)(N-2)} + \frac{9}{4} \sum_j F_{0j}^2 \frac{\tilde{N} - 1}{N - 1} \\
&\quad - \frac{9}{4} \sum_{i,j} F_{0j} F_{0i} \left[\frac{\tilde{N} - 2n - 1}{N - 1} \right]^2 \\
&= \frac{9}{4} \sum_{i \neq j} F_{0i} F_{j0} \left(\frac{(\tilde{N} - 2n - 1)(\tilde{N} - 2n - 2) - 2n}{(N-1)(N-2)} - \left[\frac{\tilde{N} - 2n - 1}{N - 1} \right]^2 \right) \\
&\quad + \frac{9}{4} \sum_j F_{0j}^2 \left(\frac{\tilde{N} - 1}{N - 1} - \left[\frac{\tilde{N} - 2n - 1}{N - 1} \right]^2 \right)
\end{aligned}
\tag{B.19}
$$

Since the leading order of the first term is $1/N$, it vanishes in the limit of large N. The second term yields a squared cP, compare with eq. B.10.

$$
\langle \nu^2 \rangle = \frac{9}{4} \sum_j F_{0j}^2 \left(c - c^2 P^2 \right) \qquad \text{for } N, \tilde{N} \to \infty \tag{B.20}
$$

The second central moment is proportional to the line width. So for a given concentration, the line width decreases with increasing polarization.

B.3. The third moment $\langle \mathbf{m^3} \rangle$

To calculate the third moment, we assume $i \neq j$, $k \neq l$ and $r \neq s$ throughout the section, and start with the calculation of some smaller commutators that will be useful later on.

$$
\begin{aligned}
[I_j^z I_i^z, I_l^- I_k^z] &= \delta_{il} [I_j^z I_i^z, I_i^- I_k^z] + \delta_{jl} [I_j^z I_i^z, I_j^- I_k^z] \\
&= \delta_{il} [I_i^z, I_i^-] I_j^z I_k^z + \delta_{jl} [I_j^z, I_j^-] I_i^z I_k^z \\
&= -\delta_{il} I_i^- I_j^z I_k^z - \delta_{jl} I_j^- I_i^z I_k^z
\end{aligned}
\tag{B.21}
$$

$$
\begin{aligned}
[I_j^+ I_i^-, I_l^- I_k^z] &= [I_j^+ I_i^-, I_l^- I_k^z] \\
&= I_j^+ I_i^- I_l^- I_k^z - I_l^- I_k^z I_j^+ I_i^- \\
&= I_j^+ I_i^- I_l^- I_k^z - I_l^- I_j^+ I_k^z I_i^- - \delta_{kj} I_l^- [I_k^z, I_j^+] I_i^- \\
&= I_j^+ I_i^- I_l^- I_k^z - I_j^+ I_l^- I_k^z I_i^- - \delta_{lj} [I_l^-, I_j^+] I_k^z I_i^- - \delta_{kj} I_l^- [I_k^z, I_j^+] I_i^- \\
&= I_j^+ I_i^- I_l^- I_k^z - I_j^+ I_l^- I_i^- I_k^z - \delta_{ki} I_j^+ I_l^- [I_k^z, I_i^-] \\
&\quad - \delta_{lj} [I_l^-, I_j^+] I_k^z I_i^- - \delta_{kj} I_l^- [I_k^z, I_j^+] I_i^- \\
&= -\Big(\delta_{ki} I_j^+ I_l^- [I_k^z, I_i^-] + \delta_{lj} [I_l^-, I_j^+] I_k^z I_i^- + \delta_{kj} I_l^- [I_k^z, I_j^+] I_i^- \Big) \\
&= \delta_{lj} 2 I_j^z I_k^z I_i^- + \delta_{ki} I_j^+ I_l^- I_i^- - \delta_{kj} I_l^- I_j^+ I_i^- \\
&= \delta_{lj} 2 I_j^z I_k^z I_i^- + (\delta_{ki} - \delta_{kj}) I_j^+ I_l^- I_i^- \qquad \text{(B.22)}
\end{aligned}
$$

This is possible because $k \neq l$ allows to commute operators with index j and those with index l under δ_{kj}.

The next step is to calculate three basic traces with four and five spin operators, a tedious necessity. The four operator trace is still fairly easy:

$$
\begin{aligned}
\frac{\mathrm{Tr}\left(I_j^+ I_k^- I_i^- I^+\right)}{\mathrm{Tr}\left(I^- I^+\right)} &= \delta_{jk} \frac{\mathrm{Tr}\left(I_j^+ I_j^- I_i^- I_i^+\right)}{\mathrm{Tr}\left(I^- I^+\right)} \\
&= \frac{\delta_{jk}}{\mathrm{Tr}\left(I^- I^+\right)} \sum_f \delta_{i\downarrow} \delta_{j\uparrow} \\
&= \frac{\delta_{jk}}{\mathrm{Tr}\left(I^- I^+\right)} \binom{N-2}{\tilde{N}-2} \binom{\tilde{N}-2}{n-1} \\
&= \delta_{jk} \frac{n}{N(N-1)} \qquad \text{(B.23)}
\end{aligned}
$$

It gets a little more complicated if we add an additional I^z-operator:

$$
\begin{aligned}
&\frac{\mathrm{Tr}\left(I_j^+ I_l^- I_i^- I_s^+ I_r^z\right)}{\mathrm{Tr}\left(I^- I^+\right)} \\
&= \frac{\delta_{jl}\delta_{is}}{\mathrm{Tr}\left(I^- I^+\right)} \mathrm{Tr}\left(I_j^+ I_j^- I_i^- I_i^+ I_r^z\right) \\
&= \frac{1}{2}\frac{\delta_{jl}\delta_{is}}{\mathrm{Tr}\left(I^- I^+\right)} \sum_f \delta_{i\downarrow}\delta_{j\uparrow}(\delta_{r\uparrow} - \delta_{r\downarrow}) \\
&= \frac{1}{2}\frac{\delta_{jl}\delta_{is}}{\mathrm{Tr}\left(I^- I^+\right)} \left(\delta_{rj} \binom{N-2}{\tilde{N}-2} \binom{\tilde{N}-2}{n-1} + (1-\delta_{rj}) \binom{N-3}{\tilde{N}-3} \left[\binom{\tilde{N}-3}{n-2} - \binom{\tilde{N}-3}{n-1} \right] \right) \\
&= \frac{1}{2}\delta_{jl}\delta_{is} \left(\delta_{rj} \frac{n}{N(N-1)} - (1-\delta_{rj}) \frac{n(\tilde{N}-2n)}{N(N-1)(N-2)} \right)
\end{aligned}
\tag{B.24}
$$

The terms with $r = i$ do not contribute due to δ_{is}.
The next trace is by far the most intricate and we tackle it step by step.

$$
\begin{aligned}
\frac{\mathrm{Tr}\left(I_j^z I_l^z I_i^- I_s^+ I_r^z\right)}{\mathrm{Tr}\left(I^- I^+\right)} &= \delta_{si} \mathrm{Tr}\left(I_j^z I_l^z I_i^- I_i^+ I_r^z\right) / \mathrm{Tr}\left(I^- I^+\right) \\
&= \frac{\delta_{si}}{8} \sum_f \left[\delta_{i\downarrow}(\delta_{j\uparrow} - \delta_{j\downarrow})(\delta_{l\uparrow} - \delta_{l\downarrow})(\delta_{r\uparrow} - \delta_{r\downarrow}) \right] / \mathrm{Tr}\left(I^- I^+\right) \\
&= \frac{\delta_{si}}{8} \left[\textcircled{1} + \textcircled{2} + \cdots + \textcircled{7} \right]
\end{aligned}
\tag{B.25}
$$

The possibilities of indices to be equal or unequal are numerous in this trace. So as not to get lost, visualization is helpful and a tree diagram is the method of choice. At each

node a decision is made whether two indices are equal or unequal. The asymmetry of the tree is a consequence of the ($j \neq i$ and $r \neq i = s$) precondition.

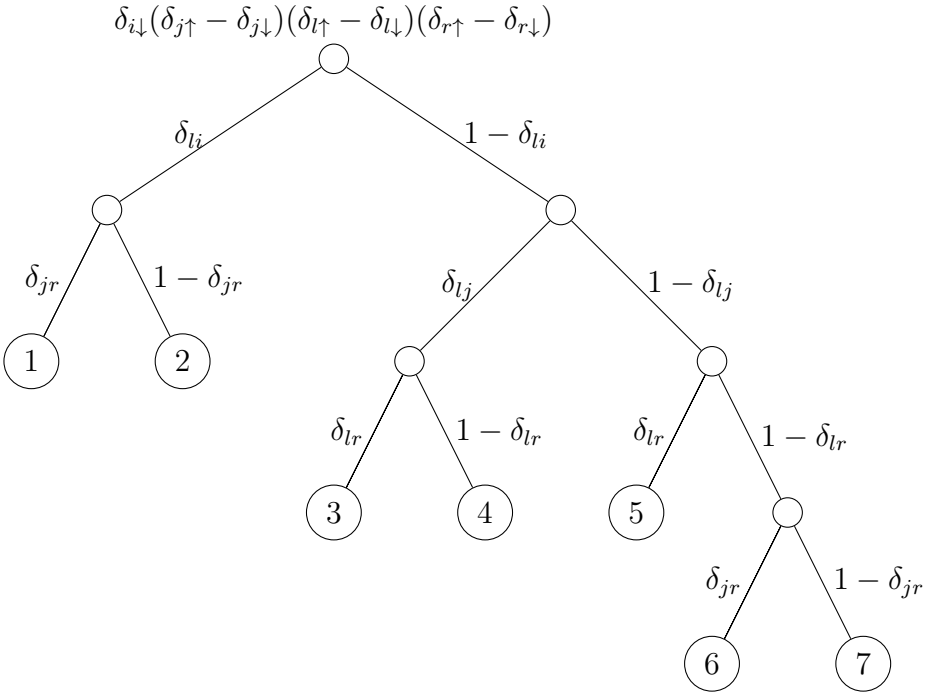

$$
\begin{aligned}
\textcircled{1} &= -\delta_{li}\delta_{jr}\tbinom{N-2}{\tilde{N}-2}\left[\tbinom{\tilde{N}-2}{n-1} + \tbinom{\tilde{N}-2}{n}\right]/\mathrm{Tr}\left(I^- I^+\right) = -\delta_{li}\delta_{jr}\tfrac{\tilde{N}-1}{N(N-1)} \\
\textcircled{2} &= -\delta_{li}(1-\delta_{jr})\tbinom{N-3}{\tilde{N}-3}\left[\tbinom{\tilde{N}-3}{n-2} + \tbinom{\tilde{N}-3}{n} - 2\tbinom{\tilde{N}-3}{n-1}\right]/\mathrm{Tr}\left(I^- I^+\right) \\
&= -\delta_{li}(1-\delta_{jr})\tfrac{(\tilde{N}-2n-1)(\tilde{N}-2n-2)-2n}{N(N-1)(N-2)} \\
\textcircled{3} &= (1-\delta_{li})\delta_{lj}\delta_{lr}\tbinom{N-2}{\tilde{N}-2}\left[\tbinom{\tilde{N}-2}{n-1} - \tbinom{\tilde{N}-2}{n}\right]/\mathrm{Tr}\left(I^- I^+\right) = -(1-\delta_{li})\delta_{lj}\delta_{lr}\tfrac{\tilde{N}-2n-1}{N(N-1)} \\
\textcircled{4} &= (1-\delta_{li})\delta_{lj}(1-\delta_{lr})\tbinom{N-3}{\tilde{N}-3}\left[\tbinom{\tilde{N}-3}{n-2} - \tbinom{\tilde{N}-3}{n}\right]/\mathrm{Tr}\left(I^- I^+\right) \\
&= -(1-\delta_{li})(1-\delta_{lr})\delta_{lj}\tfrac{(\tilde{N}-2)(\tilde{N}-2n-1)}{N(N-1)(N-2)} \\
\textcircled{5} &= (1-\delta_{li})(1-\delta_{lj})\delta_{lr}\tbinom{N-3}{\tilde{N}-3}\left[\tbinom{\tilde{N}-3}{n-2} - \tbinom{\tilde{N}-3}{n}\right]/\mathrm{Tr}\left(I^- I^+\right) \\
&= -(1-\delta_{li})(1-\delta_{lj})\delta_{lr}\tfrac{(\tilde{N}-2)(\tilde{N}-2n-1)}{N(N-1)(N-2)} \\
\textcircled{6} &= (1-\delta_{li})(1-\delta_{lj})(1-\delta_{lr})\delta_{jr}\tbinom{N-3}{\tilde{N}-3}\left[\tbinom{\tilde{N}-3}{n-2} - \tbinom{\tilde{N}-3}{n}\right]/\mathrm{Tr}\left(I^- I^+\right) \\
&= -(1-\delta_{li})(1-\delta_{lj})\delta_{jr}\tfrac{(\tilde{N}-2)(\tilde{N}-2n-1)}{N(N-1)(N-2)} \\
\textcircled{7} &= (1-\delta_{li})(1-\delta_{lj})(1-\delta_{lr})(1-\delta_{jr})\tbinom{N-4}{\tilde{N}-4}\tfrac{\left[\binom{\tilde{N}-4}{n-3} - 3\binom{\tilde{N}-4}{n-2} + 3\binom{\tilde{N}-4}{n-1} - \binom{\tilde{N}-4}{n}\right]}{\mathrm{Tr}(I^- I^+)} \\
&= -(1-\delta_{li})(1-\delta_{lj})(1-\delta_{lr})(1-\delta_{jr})(\tilde{N}-2n-1)\tfrac{(\tilde{N}-2n-3)(\tilde{N}-2n-2)-6n}{N(N-1)(N-2)(N-3)}
\end{aligned}
\tag{B.26}
$$

We now can continue evaluating eq. B.25. A certain simplification is possible, because the terms 4, 5 and 6 are similar.

$$
\begin{aligned}
&\frac{\mathrm{Tr}\left(I_j^z I_l^z I_i^- I_i^+ I_r^z\right)}{\mathrm{Tr}\left(I^- I^+\right)} = \frac{\delta_{si}}{8}\left[\textcircled{1} + \textcircled{2} + \cdots + \textcircled{7}\right] \\
&= -\tfrac{\delta_{si}}{8}\Bigg[\delta_{li}\delta_{jr}\tfrac{\tilde{N}-1}{N(N-1)} + \delta_{li}(1-\delta_{jr})\tfrac{(\tilde{N}-2n-1)(\tilde{N}-2n-2)-2n}{N(N-1)(N-2)} + (1-\delta_{li})\delta_{lj}\delta_{lr}\tfrac{\tilde{N}-2n-1}{N(N-1)} \\
&\quad + \tfrac{(\tilde{N}-2)(\tilde{N}-2n-1)}{N(N-1)(N-2)}(1-\delta_{li})\Big\{\delta_{lj}(1-\delta_{lr}) + (1-\delta_{lj})\delta_{lr} + (1-\delta_{lj})\delta_{jr}\Big\} \\
&\quad + (1-\delta_{li})(1-\delta_{lj})(1-\delta_{lr})(1-\delta_{jr})(\tilde{N}-2n-1)\tfrac{(\tilde{N}-2n-3)(\tilde{N}-2n-2)-6n}{N(N-1)(N-2)(N-3)}\Bigg]
\end{aligned}
\tag{B.27}
$$

Next we need to simplify the nested commutators and multiply the result with $[H_0, I^+]$.

$$
\begin{aligned}
&[H_0,[H_0,I^-]] = \left[\mu B I^z + \sum_{i\neq j} F_{ij}\left(I_j^z I_i^z - \frac{I_j^+ I_i^-}{2}\right), -\mu B I^- - 3\sum_{i\neq j} F_{ij} I_j^- I_i^z\right] \\
&= -(\mu B)^2[I^z,I^-] - \mu B\sum_{i\neq j} F_{ij}\left(3[I^z, I_j^- I_i^z] + [I_j^z I_i^z, I^-] - \frac{1}{2}[I_j^+ I_i^-, I^-]\right) \\
&\quad - \frac{3}{2}\sum_{i\neq j}\sum_{k\neq l} F_{ij}F_{kl}\Big(2\left[I_j^z I_i^z, I_l^- I_k^z\right] - \left[I_j^+ I_i^-, I_l^- I_k^z\right]\Big) \\
&= (\mu B)^2 I^- + \mu B\sum_{i\neq j} F_{ij}\left(3I_j^- I_i^z + I_j^- I_i^z + I_j^z I_i^- + I_j^z I_i^-\right) \\
&\quad + \frac{3}{2}\sum_{i\neq j}\sum_{k\neq l} F_{ij}F_{kl}\Big(2\delta_{il} I_j^z I_k^z I_i^- + 2\delta_{jl} I_i^z I_k^z I_j^- + 2\delta_{lj} I_j^z I_k^z I_i^- + (\delta_{ki}-\delta_{kj}) I_j^+ I_l^- I_i^-\Big) \\
&= (\mu B)^2 I^- + 6\mu B\sum_{i\neq j} F_{ij} I_j^- I_i^z \\
&\quad + \frac{3}{2}\sum_{i\neq j}\sum_{k\neq l} F_{ij}F_{kl}\Big((4\delta_{ik}+2\delta_{kj}) I_j^z I_l^z I_i^- + (\delta_{ki}-\delta_{kj}) I_j^+ I_l^- I_i^-\Big)
\end{aligned}
\tag{B.28}
$$

$$
\begin{aligned}
&\frac{\mathrm{Tr}\left([H_0,[H_0,I^-]][H_0,I^+]\right)}{\mathrm{Tr}\left(I^-I^+\right)} = \\
&= \frac{\mathrm{Tr}\left(\left[(\mu B)^2 I^- + 6\mu B \sum_{i\neq j} F_{ij} I_j^- I_i^z + \tfrac{3}{2} \sum_{i\neq j,k\neq l} F_{ij}F_{kl}\Big((4\delta_{ik}+2\delta_{kj}) I_j^z I_l^z I_i^- + (\delta_{ki}-\delta_{kj}) I_j^+ I_l^- I_i^-\Big)\right] \cdot \left[\mu B I^+ + 3\sum_{k\neq l} F_{kl} I_l^+ I_k^z\right]\right)}{\mathrm{Tr}\left(I^-I^+\right)} \\
&= (\mu B)^3 \frac{\mathrm{Tr}\left(I^-I^+\right)}{\mathrm{Tr}\left(I^-I^+\right)} + 9(\mu B)^2 \sum_{i\neq j} F_{ij} \frac{\mathrm{Tr}\left(I_j^- I_i^z I_j^+\right)}{\mathrm{Tr}\left(I^-I^+\right)} \\
&\quad + \frac{3}{2}\mu B \sum_{i\neq j}\sum_{k\neq l} F_{ij}F_{kl}\left((16\delta_{ik}+2\delta_{kj}) \frac{\mathrm{Tr}\left(I_j^z I_l^z I_i^- I_i^+\right)}{\mathrm{Tr}\left(I^-I^+\right)} + (\delta_{ki}-\delta_{kj}) \frac{\mathrm{Tr}\left(I_j^+ I_l^- I_i^- I_i^+\right)}{\mathrm{Tr}\left(I^-I^+\right)}\right) \\
&\quad + \frac{9}{2}\sum_{i\neq j}\sum_{k\neq l}\sum_{r\neq s} F_{ij}F_{kl}F_{rs}\left((4\delta_{ik}+2\delta_{kj}) \frac{\mathrm{Tr}\left(I_j^z I_l^z I_i^- I_s^+ I_r^z\right)}{\mathrm{Tr}\left(I^-I^+\right)} + (\delta_{ki}-\delta_{kj}) \frac{\mathrm{Tr}\left(I_j^+ I_l^- I_i^- I_s^+ I_r^z\right)}{\mathrm{Tr}\left(I^-I^+\right)}\right) \\
&= (\mu B)^3 - \frac{9}{2}(\mu B)^2 \sum_j F_{0j} \frac{\tilde{N}-2n-1}{N-1} + \frac{27}{4}\mu B \sum_{j\neq l} F_{0j}F_{0l}\left(\delta_{jl}\frac{\tilde{N}-1}{N-1} + (1-\delta_{jl})\frac{(\tilde{N}-2n-1)(\tilde{N}-2n-2)-2n}{(N-1)(N-2)}\right) \\
&\quad - \frac{27}{8}\sum_l F_{0l}^3 \frac{\tilde{N}-2n-1}{N-1} - 9\sum_{l\neq r} F_{r0}F_{0l}^2 \frac{(\tilde{N}-2n-1)(\tilde{N}-2)}{(N-1)(N-2)} - \frac{9}{8}\sum_{j\neq l} F_{0l}F_{0j}F_{jl} \frac{(\tilde{N}-2)(\tilde{N}-2n-1)}{(N-1)(N-2)} \\
&\quad - \frac{9}{8}(\tilde{N}-2n-1)\frac{(\tilde{N}-2n-3)(\tilde{N}-2n-2)-6n}{(N-1)(N-2)(N-3)}\left(2\sum_{j\neq r\neq l\neq j} F_{0r}F_{0j}F_{0l} + \sum_{j\neq r\neq l\neq j} F_{0r}F_{0j}F_{jl}\right)
\end{aligned}
\tag{B.29}
$$

As in the calculations of the second moment, most terms of the third will vanish if we use the third central moment instead.

$$\langle \nu^3 \rangle = \Big\langle (m - \langle m \rangle)^3 \Big\rangle = \langle m^3 \rangle - 3 \langle \nu \rangle \langle \nu^2 \rangle - \langle \nu \rangle^3 \tag{B.30}$$

$$\begin{aligned}
&3 \langle \nu \rangle \langle \nu^2 \rangle + \langle \nu \rangle^3 \\
&= 3\left[\mu B - \frac{3}{2}\sum_j F_{0j}\frac{\tilde{N}-2n-1}{N-1}\right]\left[\frac{9}{4}\sum_j F_{0j}^2\left(\frac{\tilde{N}-1}{N-1} - \left[\frac{\tilde{N}-2n-1}{N-1}\right]^2\right)\right. \\
&\quad \left. + \frac{9}{4}\sum_{i\neq j} F_{0i}F_{j0}\left(\frac{(\tilde{N}-2n-1)(\tilde{N}-N-2n) - 2n(N-1)}{(N-1)^2(N-2)}\right)\right] \\
&\quad + \left[\mu B - \frac{3}{2}\sum_j F_{0j}\frac{\tilde{N}-2n-1}{N-1}\right]^3 \\
&= (\mu B)^3 - \frac{9}{2}(\mu B)^2 \sum_j F_{0j}\frac{\tilde{N}-2n-1}{N-1} \\
&\quad + \frac{27}{4}\mu B \sum_{j\neq l} F_{0j}F_{0l}\left(\delta_{jl}\frac{\tilde{N}-1}{N-1} + (1-\delta_{jl})\frac{(\tilde{N}-2n-1)(\tilde{N}-2n-2)-2n}{(N-1)(N-2)}\right) \\
&\quad - \frac{81}{8}\sum_{l,j,r} F_{0l}F_{0j}F_{0r}\frac{\tilde{N}-2n-1}{N-1}\left(\delta_{jl}\frac{\tilde{N}-1}{N-1} + (1-\delta_{jl})\frac{(\tilde{N}-2n-1)(\tilde{N}-2n-2)-2n}{(N-1)(N-2)}\right) \\
&\quad + \frac{54}{8}\sum_j\sum_k\sum_r F_{0j}F_{0k}F_{0r}\frac{(\tilde{N}-2n-1)^3}{(N-1)^3}
\end{aligned} \tag{B.31}$$

Comparing eq. B.31 and eq. B.29, one finds that the terms which are proportional to μB, $(\mu B)^2$ and $(\mu B)^3$ are equal. Thus they cancel each other out when we calculate $\langle \nu^3 \rangle^3$.

$$
\begin{aligned}
&\langle \nu^3 \rangle \\
&= \frac{9}{8}\frac{\tilde{N}-2n-1}{N-1}\Bigg[-3\sum_l F_{0l}^3 + \frac{\tilde{N}-2}{N-2}\Bigg(9\sum_{l,r} F_{r0}F_{0l}^2 - 8\sum_{l\neq r} F_{r0}F_{0l}^2 - \sum_{l\neq r} F_{r0}F_{0l}F_{rl}\Bigg) \\
&\quad - \frac{(\tilde{N}-2n-3)(\tilde{N}-2n-2)-6n}{(N-2)(N-3)}\Bigg(2\sum_{j\neq r\neq l\neq j} F_{0r}F_{0j}F_{0l} + \sum_{j\neq r\neq l\neq j} F_{0r}F_{0j}F_{jl}\Bigg) \\
&\quad + 9\sum_{l\neq j,r} F_{0l}F_{0j}F_{0r}\frac{(\tilde{N}-2n-1)(\tilde{N}-2n-2)-2n}{(N-1)(N-2)} \\
&\quad + 6\sum_j\sum_k\sum_r F_{0j}F_{0k}F_{0r}\frac{(\tilde{N}-2n-1)^2}{(N-1)^2}\Bigg] \\
&\longrightarrow \frac{9}{8}cP\Bigg[-3\sum_l F_{0l}^3 + c\Bigg(9\sum_{l,r} F_{r0}F_{0l}^2 - 8\sum_{l\neq r} F_{r0}F_{0l}^2 - \sum_{l\neq r} F_{r0}F_{0l}F_{rl}\Bigg) \\
&\quad - c^2P^2\Bigg(2\sum_{j\neq r\neq l\neq j} F_{0r}F_{0j}F_{0l} + \sum_{j\neq r\neq l\neq j} F_{0r}F_{0j}F_{jl} - 9\sum_{l\neq j,r} F_{0l}F_{0j}F_{0r} \\
&\qquad\qquad - 6\sum_j\sum_k\sum_r F_{0j}F_{0k}F_{0r}\Bigg)\Bigg] \\
&= \frac{9}{8}cP\Bigg[-3\sum_l F_{0l}^3 + c\Bigg(8\sum_l F_{0l}^3 + \sum_{l,r} F_{r0}F_{0l}^2 - \sum_{l\neq r} F_{r0}F_{0l}F_{rl}\Bigg) \\
&\quad - c^2P^2\Bigg(5\sum_l F_{0l}^3 + \sum_{l,r} F_{r0}F_{0l}^2 - \sum_{l\neq r} F_{r0}F_{0l}F_{rl} + \sum_{r\neq j\neq k} F_{0j}F_{0r}(F_{jk}-F_{0k})\Bigg)\Bigg] \\
&= \frac{9}{8}cP\Bigg[-3\sum_l F_{0l}^3\Big(1-c\Big) + \Bigg(5\sum_l F_{0l}^3 + \sum_{l,r} F_{r0}F_{0l}^2 - \sum_{l\neq r} F_{r0}F_{0l}F_{rl}\Bigg)\Big(c-c^2P^2\Big)\Bigg] \\
&= cP\Big[\lambda_3(1-c) + \lambda_4\Big(c-c^2P^2\Big)\Big] \qquad \text{(B.32)}
\end{aligned}
$$

For $c \to 1$ this yields exactly the same expression Tsyplyatyev and Whittaker found [Tsy12].

B.4. Classical approach

The correct concentration c and polarization P dependency for the first and second central moment can be deduced from classical statistical arguments, by calculating the expectation value and the variance of the spin random variable at a given location, using the values from the table below.

	^{129}Xe ↑	^{129}Xe ↓	^{132}Xe
spin	$+1$	-1	0
isotope probability	c		$1-c$
polarization probability	p	$1-p$	

The expectation value of the spin polarization for a given nucleus is

$$\mu = (+1)cp + (-1)c(1-p) = c(2p-1) = c \cdot P \quad . \tag{B.33}$$

And accordingly the variance:

$$\begin{aligned} \sigma^2 &= (1-c(2p-1))^2 cp + (-1-c(2p-1))^2 c(1-p) + c^2(2p-1)^2(1-c) \\ &= c - c^2P^2 \end{aligned} \tag{B.34}$$

This yields the same concentration/polarization dependency as the quantum mechanical calculations; albeit not the pre-factors.

B.5. The moment problem

In the last sections I showed how the moments of the resonance line are calculated. This section is about the reverse process, that is to derive a function from the moments that approximates the resonance line. This is called the *moment problem*. Depending on the interval that the function is defined on, one distinguishes between the Stieltjes moment problem $[0, \infty[$, the Hausdorff moment problem $[0, 1]$ and the Hamburger moment problem $\mathbb{R}$ [Chr14, Akh65].
Since our resonance line lives on the whole real (frequency) axis and we know the form of the first three moments, we need to solve the *truncated Hamburger moment problem*, sometimes also referred to as a *truncated power moment problem*. For the following calculations we use these central moments:

$$\begin{aligned} \langle \nu^0 \rangle &= 1 \\ \langle \nu^1 \rangle &= 0 \\ \langle \nu^2 \rangle &= \lambda_2 \Big(c - c^2 P^2 \Big) \\ \langle \nu^3 \rangle &= cP \Big[\lambda_3 \Big(c - 1 \Big) + \lambda_4 \Big(c - c^2 P^2 \Big) \Big] \end{aligned} \tag{B.35}$$

Compared to eq. 2.13 these central moments are slightly different, the first moment equals zero here and the zeroth moment equals one. The sudden change is for consistency reasons. In the quantum mechanical calculations all moments are normalized by

the zeroth moment. Additionally the central moments are also calculated in relation to the first moment (see sections B.1 – B.3).
The calculations follow the algorithm described in [Cur91] for an odd number of moments.

The problem is only solvable if the determinants of all Hankel matrices H_i are positive, which is the case here, because $0 < c \leq 0$, $|P| \leq 1$ and $0 < \lambda_2$; If we exclude that $c = 1$ and $P = 1$ at the same time.

$$\begin{aligned} H_0 &= |\langle \nu^0 \rangle| = 1 > 0 \\ H_1 &= \begin{vmatrix} \langle \nu^0 \rangle & \langle \nu^1 \rangle \\ \langle \nu^1 \rangle & \langle \nu^2 \rangle \end{vmatrix} = \begin{vmatrix} 1 & 0 \\ 0 & \lambda_2\left(c - c^2 P^2\right) \end{vmatrix} = \lambda_2\left(c - c^2 P^2\right) > 0 \end{aligned} \tag{B.36}$$

From adjacent central moments we construct three 2-dimensional vectors.

$$\begin{aligned} \vec{v}_0 &= \begin{pmatrix} \langle \nu^0 \rangle \\ \langle \nu^1 \rangle \end{pmatrix} \\ \vec{v}_1 &= \begin{pmatrix} \langle \nu^1 \rangle \\ \langle \nu^2 \rangle \end{pmatrix} \\ \vec{v}_2 &= \begin{pmatrix} \langle \nu^2 \rangle \\ \langle \nu^3 \rangle \end{pmatrix} \end{aligned} \tag{B.37}$$

Three vectors in a 2-dimensional space are linear dependent and we can express the last vector as a non-trivial linear combination of the other two.

$$\vec{v}_2 = \phi_0 \vec{v}_0 + \phi_1 \vec{v}_1 \tag{B.38}$$

Next we need to calculate the coefficients of the vector $\vec{\Phi} = (\phi_0, \phi_1)$. The easiest way to do this is to invert the Hankel matrix from eq. B.36.

$$\vec{\Phi} = H_1^{-1} \vec{v}_2 \tag{B.39}$$

From $\vec{\Phi}$ we construct a polynomial $g(t)$ and calculate its two real roots t_0 and t_1, which are the basis of the solution function.

$$g(t) = t^2 - (\phi_0 + \phi_1 t) \tag{B.40}$$

Then we calculate a weight for each root t_i. This is done with the inverse of a Vandermonde matrix:

$$\rho = \begin{pmatrix} \rho_0 \\ \rho_1 \end{pmatrix} = \begin{pmatrix} 1 & 1 \\ t_0 & t_1 \end{pmatrix}^{-1} \cdot \vec{v}_0 \tag{B.41}$$

The solution function is then the sum over "atomic probability measures" at t_i multiplied with the corresponding weight ρ_i.

$$\mu = \sum_{i=0}^{k} \rho_i \delta_{t_i} \tag{B.42}$$

In the case of only three moments the expressions one gets are simple enough that it is possible to analytically calculate μ. The solution for the moments specified in eq. B.35 is:

$$f(\nu) = \rho_0 \, \delta(\nu - t_0) + \rho_1 \, \delta(\nu - t_1) \tag{B.43}$$

with the Dirac δ function and

$$\begin{aligned} t_0 &= \frac{1}{2}(a - c) \\ t_1 &= \frac{1}{2}(a + c) \\ \rho_0 &= \frac{1}{2}\left(1 + \frac{a}{c}\right) \\ \rho_1 &= \frac{1}{2}\left(1 - \frac{a}{c}\right) \end{aligned} \tag{B.44}$$

where

$$a = \frac{\langle \nu^3 \rangle}{\langle \nu^2 \rangle} \qquad b = \langle \nu^2 \rangle \qquad c = \sqrt{4b + a^2} \; . \tag{B.45}$$

The integrals to calculate the moments are all well defined because of the delta functions. And one can easily verify that this is indeed a solution of our moment problem. Despite this the solution is not satisfying, as it only consists of two points and hence doesn't approximate a spectrum.

C. Xenon properties

Table C.1 shows some thermodynamical properties of xenon, while fig. C.1 shows a mass spectrum recorded with our QMS.

Triple point temperature	161.4 K
Triple point pressure	81.59 kPa
Melting point	165.10 K (-108.04 °C)
Boiling Point	168.81 K (-111.75 °C)
Critical temperature	16.58 °C
Van der Waals constants (real gas)	$a = 4.192\ \frac{\mathrm{Bar\,L^2}}{\mathrm{mol}}$
	$b = 0.05156\ \frac{\mathrm{L}}{\mathrm{mol}}$

Table C.1.: Thermodynamic properties of xenon from [Lid96].

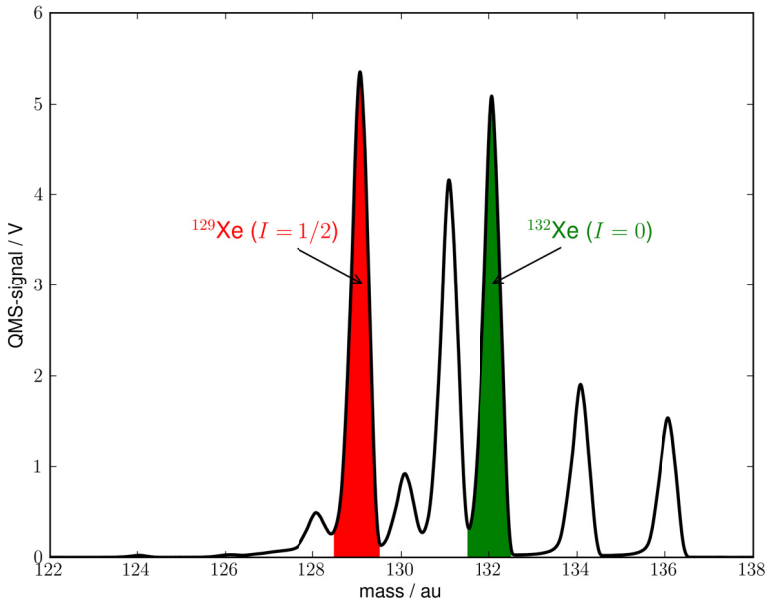

Figure C.1.: Mass spectrum of the natural xenon that is attached to the UHV-chamber. The colored areas are the two main isotopes that we also use in pure form (99.9+ %).

D. List of equipment

List of instruments that are used in the experiments. Internal ID refers to instruments (or parts thereof, like the casing or wiring) built by the workshops of the institute.

Description	**Internal ID**	**Manufacturer**	**Model number**
Ar-Ion laser		Spectra-Physics	BeamLok 2080-15S
Ti:Sapphire laser		Spectra-Physics	3900S
NMR magnet		Varian	XL-100-15
NMR-spectrometer	SPM-01	SpinCore Technologies	PulseBlaster RadioProcessor
Preamplifier (2x)		Advanced Receiver Research	P23.6 UDG
LPPA		Dressler	LPPA 13010
Quarter wave cable	NMR-04		
Vector network analyzer		ADVANTEST	R3753EH
Temperature controller	TR-30	Newport	iSeries
Direct current heating		Heinzinger	PTN 16-40
Chopper control	CHS-05		
AD computer card		FAST	TR1202
Ion (sputter) gun		Specs	Power supply 867911 Ion gun IQE 10/35
QMS		UTI	100C
Manipulator control unit	SMS-19a		
Transferfield power supply		FUG	MCN 350-350
Gradient coils power supply		FUG	NTN 350-12,5
3 Axis magnetic field sensor	MFM-01/01	Stefan Mayer Instr.	FLC3-70

Bibliography

[Abr61] A. Abragam. *The principles of nuclear magnetism: the international series of monographs on physics*. Clarendon Press, Oxford (1961). Reprinted 1986.

[Abr73] A. Abragam, M. Chapellier, J. Jacquinot, and M. Goldman. *Absorption lineshape of highly polarized nuclear spin systems*. Journal of Magnetic Resonance (1969), 10(3):322 (1973).

[Akh65] N. I. Akhiezer and N. Kemmer. *The classical moment problem: and some related questions in analysis*, volume 5. Oliver & Boyd Edinburgh (1965).

[AL88] F. Agullö-Löpez, C. R. A. Catlow, and P. D. Townsend. *Point defects in materials*, volume 149. Academic Press London (1988).

[Beg14] S. Beguš, J. Bojkovski, J. Drnovšek, and G. Geršak. *Magnetic effects on thermocouples*. Measurement Science and Technology, 25(3):035006 (2014).

[Ber04a] S. Berger and S. Braun. *200 and More NMR Experiments: A Practical Course*. Wiley-VCH Verlag GmbH & Co. KGaA (2004).

[Ber04b] W. Berthold, F. Rebentrost, P. Feulner, and U. Höfer. *Influence of Ar, Kr, and Xe layers on the energies and lifetimes of image-potential states on Cu(100)*. Applied Physics A, 78(2):131 (2004).

[Blo46] F. Bloch, W. Hansen, and M. Packard. *The Nuclear Induction Experiment*. Phys. Rev., 70:474 (1946).

[Bru13] *Bruker Almanac 2013* (2013). Accessed: 26.09.2014.

[Bus11] M. Buschmann. *Xe-129 NMR an konzentrierten und verdünnten Xe-Isotopengemischen*. Diploma thesis, Philipps Universität Marburg (2011).

[Can94] D. Candela, M. E. Hayden, and P. J. Nacher. *Steady-State Production of High Nuclear Polarization in* ^{3}He-^{4}He *Mixtures*. Phys. Rev. Lett., 73:2587 (1994).

[Chr14] J. Christiansen. *The moment problem*. `http://www.williams.edu/go/math/sjmiller/public_html/book/papers/jcmp.pdf`. Accessed 25.10.2014.

[Cra79] J. Crank. *The mathematics of diffusion*. Oxford university press, 2nd edition (1979).

[Cur91] R. E. Curto and L. A. Fialkow. *Recursiveness, positivity, and truncated moment problems*. Houston Journal of Mathematics, 17(4):603 (1991).

[dJ90] A. de Jong and J. Niemantsverdriet. *Thermal desorption analysis: Comparative test of ten commonly applied procedures.* Surface Science, 233(3):355 (1990).

[Don70] S. Doniach and M. Sunjic. *Many-electron singularity in X-ray photoemission and X-ray line spectra from metals.* Journal of Physics C: Solid State Physics, 3(2):285 (1970).

[Dur14] *Duran properties.* `http://www.duran-group.com/en/about-duran/duran-properties.html`. Accessed: 24.11.2014.

[Fit99] R. J. Fitzgerald, M. Gatzke, D. C. Fox, G. D. Cates, and W. Happer. ^{129}Xe *spin relaxation in frozen xenon.* Phys. Rev. B, 59:8795 (1999).

[Fuk81] E. Fukushima and S. B. Roeder. *Experimental pulse NMR: a nuts and bolts approach.* Addison-Wesley Reading, MA: (1981).

[Gat92] M. Gatzke. *Nuclear spin relaxation in polarized solid xenon.* Ph.D. thesis, Princeton University (1992).

[Gat93] M. Gatzke, G. D. Cates, B. Driehuys, D. Fox, W. Happer, and B. Saam. *Extraordinarily slow nuclear spin relaxation in frozen laser-polarized* ^{129}Xe. Phys. Rev. Lett., 70:690 (1993).

[Ger87] I. Gerothanassis. *Methods of avoiding the effects of acoustic ringing in pulsed fourier transform nuclear magnetic resonance spectroscopy.* Progress in Nuclear Magnetic Resonance Spectroscopy, 19(3):267 (1987).

[Ger03] P. B. Gerhard. *Konventionelle Puls-NMR an Xe-129 auf Einkristalloberflächen.* Ph.D. thesis, Philipps Universität Marburg (2003).

[Hap72] W. Happer. *Optical Pumping.* Rev. Mod. Phys., 44:169 (1972).

[Har62] S. R. Hartmann and E. L. Hahn. *Nuclear Double Resonance in the Rotating Frame.* Phys. Rev., 128:2042 (1962).

[Hem96] G. Hempel and U. Schmeißer. *Moments of the Power Spectra of Dipolar Interaction between Spin-1/2 Nuclei.* Journal of Magnetic Resonance, Series A, 121(1):50 (1996).

[Iny98] A. V. Inyushkin, K. Leicht, and P. Esquinazi. *Magnetic field dependence of the sensitivity of a type E (chromel-constantan) thermocouple.* Cryogenics, 38(3):299 (1998).

[Jän04] H. J. Jänsch, P. Gerhard, and M. Koch. *129Xe on Ir(111): NMR study of xenon on a metal single crystal surface.* Proceedings of the National Academy of Sciences of the United States of America, 101(38):13715 (2004).

[Kas50] Kastler, Alfred. *Quelques suggestions concernant la production optique et la détection optique d'une inégalité de population des niveaux de quantifigation spatiale des atomes. Application à l'expérience de Stern et Gerlach et à la résonance magnétique.* J. Phys. Radium, 11(6):255 (1950).

[Kle76] M. L. Klein and J. A. Venables. *Rare gas solids*, volume 2. Academic Press (1976).

[Koc06a] M. Koch. *NMR-Experimente auf metallischen Einkristalloberflächen.* Ph.D. thesis, Philipps Universität Marburg (2006).

[Koc06b] M. Koch, P. Gerhard, and H. J. Jänsch. *{NMR} of ^{129}Xe on CO/Ir(111) and on multilayer Xe/Ir(111).* Surface Science, 600(18):3586 (2006). Berlin, Germany: 4–9 September 2005 Proceedings of the 23th European Conference on Surface Science.

[Kol77] T. G. Kollie, R. L. Anderson, J. L. Horton, and M. J. Roberts. *Large thermocouple thermometry errors caused by magnetic fields.* Review of Scientific Instruments, 48(5):501 (1977).

[Lid96] D. R. Lide. *CRC handbook of chemistry and physics.* CRC press, 77th edition (1996).

[Mat14] *Mateck GmbH, Juelich, Germany.* private communication.

[Mor07] S. W. Morgan. *Relaxation of solid hyperpolarized ^{129}Xe.* Ph.D. thesis, University of Utah (2007).

[Mus82] R. Musket, W. McLean, C. Colmenares, D. Makowiecki, and W. Siekhaus. *Preparation of atomically clean surfaces of selected elements: A review.* Applications of Surface Science, 10(2):143 (1982).

[Par73] G. W. Parker. *Calculation of moments of NMR absorption lines from free-induction decay curves.* The Journal of Chemical Physics, 58(8):3274 (1973).

[Pit14] G. A. Pitz, A. J. Sandoval, T. B. Tafoya, W. L. Klennert, and D. A. Hostutler. *Pressure broadening and shift of the rubidium D_1 transition and potassium D_2 transitions by various gases with comparison to other alkali rates.* Journal of Quantitative Spectroscopy and Radiative Transfer, 140:18 (2014).

[Pot14] A. Potzuweit, A. Schaffner, and H. J. Jänsch. *Mounting a thermocouple of type E onto a Cu single crystal for use in a magnetically sensitive environment below 77K.* Journal of Vacuum Science & Technology A, 32(5) (2014).

[Pur46] E. Purcell, H. Torrey, and R. Pound. *Resonance Absorption by Nuclear Magnetic Moments in a Solid.* Phys. Rev., 69:37 (1946).

[Rot97] M. D. Rotondaro and G. P. Perram. *Collisional broadening and shift of the rubidium D_1 and D_2 lines ($5^2S_{1/2} \rightarrow 5^2P_{1/2}, 5^2P_{3/2}$) by rare gases, H_2, D_2, N_2, CH_4 and CF_4.* Journal of Quantitative Spectroscopy and Radiative Transfer, 57(4):497 (1997).

[Rut99] U. Ruth, T. Hof, J. Schmidt, D. Fick, and H. Jänsch. *Production of nitrogen-free, hyperpolarized 129Xe gas.* Applied Physics B, 68(1):93 (1999).

[Sam05] G. L. Samuelson. *Nuclear spin relaxation of polycrystaline 129 xenon.* Ph.D. thesis, University of Utah (2005).

[Sch15] A. Schaffner. Ph.D. thesis, Philipps Universität Marburg (to be published).

[Sch90] H. Schlichting. *Methoden und Mechanismen der thermischen Desorption: Adsorptions-, Desorptions-Kinetik, Epitaxie und Ordnung von Edelgasschichten auf Ru(001).* Ph.D. thesis, Technische Universität München (1990).

[Sea62] D. R. Sears and H. P. Klug. *Density and Expansivity of Solid Xenon.* The Journal of Chemical Physics, 37(12):3002 (1962).

[Sta01] D. Stahl. *NMR an hyperpolarisiertem ^{129}Xe auf Einkristalloberflächen.* Ph.D. thesis, Philipps Universität Marburg (2001).

[Sta02] D. Stahl, W. Mannstadt, P. Gerhard, M. Koch, and H. J. Jänsch. *T_1-relaxation of ^{129}Xe on metal single crystal surfaces – multilayer experiments on iridium and monolayer considerations.* Journal of Magnetic Resonance, 159(1):1 (2002).

[Tas87] G. Tastevin. *Hélium trois polarisé: ondes de spin et liquéfaction du gaz.* Ph.D. thesis, Université Pierre et Marie Curie-Paris VI (1987).

[Tot10] N. Totò, C. Schön, and M. Jansen. *Atomistic study of xenon crystal growth via low-temperature atom beam deposition.* Phys. Rev. B, 82:115401 (2010).

[Tsy12] O. Tsyplyatyev and D. M. Whittaker. *Dipolar broadening of nuclear spin resonance under dynamical pumping.* Phys. Rev. B, 85:125123 (2012).

[Tur86] G. L. Turner, K. A. Smith, R. Kirkpatrick, and E. Oldfield. *Boron-11 nuclear magnetic resonance spectroscopic study of borate and borosilicate minerals and a borosilicate glass.* Journal of Magnetic Resonance (1969), 67(3):544 (1986).

[VV48] J. H. Van Vleck. *The Dipolar Broadening of Magnetic Resonance Lines in Crystals.* Phys. Rev., 74:1168 (1948).

[Wal97] T. G. Walker and W. Happer. *Spin-exchange optical pumping of noble-gas nuclei.* Rev. Mod. Phys., 69:629 (1997).

[Wal04] J. D. Walls, F. K. H. Phoa, and Y.-Y. Lin. *Spin dynamics at very high spin polarization.* Phys. Rev. B, 70:174410 (2004).

Wissenschaftlicher Werdegang

2002 - 2009	Philipps-Universität Marburg: Studium Diplom-Physik mit Nebenfach Informatik (Vordiplom) und Kernchemie (Diplom)
2004	Vordiplom
2005 - 2006	Erasmus-Jahr an der Lunds Tekniska Högskola (Schweden)
2009	Diplomarbeit in der AG Quantenchaos (Prof. Dr. H.-J. Stöckmann) zum Thema: *"Mikrowellenmessungen an n-Scheiben Streusystemen"*
2010 - 2015	Dissertation in der AG Oberflächen-NMR (Prof. Dr. H.J. Jänsch) zum Thema: *"Nuclear dipole interactions in solid Xe-129 measured with NMR"*

Danksagung

Mein Dank gilt allen, die zum Gelingen dieser Arbeit beigetragen haben:

Prof. Heinz Jänsch danke ich für seine ausdauernde Betreuung, die vielen hilfreichen Diskussionen, und für die Motivation weiter zu machen, auch wenn es sehr lange nicht funktioniert.

Prof. Werner Heil danke ich, dass er sich bereit erklärt hat, Zweitgutachter zu sein.

Prof. Florian Gebhard danke ich für seine Erläuterungen zur Quantenmechanik, Prof. Bernhard Schmitt für seine Hilfestellung beim Linienfit und PD. Jens Güdde dafür, dass er immer ein offenes Ohr für meine Fragen hatte.

Dem Europäischen Graduiertenkolleg "Electron-Electron Interactions in Solids, Marburg – Budapest" verdanke ich finanzielle Unterstützung und einige schöne Workshops.

Meiner Arbeitsgruppe und der ganzen Oberflächenphysik danke für die schöne Arbeitsatmosphäre.

Ohne die Werkstätten des Fachbereichs, wäre diese Arbeit nie entstanden. Insbesondere Matthias Born und Carsten Schindler haben wahre Wunder vollbracht.

Meinen Eltern, die mich all die Jahre unterstützt haben, danke ich von ganzem Herzen.

Ich danke meinen Freunden aus Physik, Sport und Rollenspiel für die schöne Zeit; die mir den Abschied aus Marburg jetzt so schwer macht.

Denen die so tapfer waren, sich meinem Englisch zu stellen und Korrektur gelesen haben: Charleen, Anuschka, Lars und Laura – ohne euch wäre diese Arbeit noch viel schwerer zu verstehen.

Ganz besonders möchte ich meiner Freundin/Kumpel/Counselor/Geliebten Charleen für ihre vielfältige Unterstützung danken.